Coastal and Offshore Science and Engineering

an International
open-access Journal

6/2024
ISSN 2785-7972

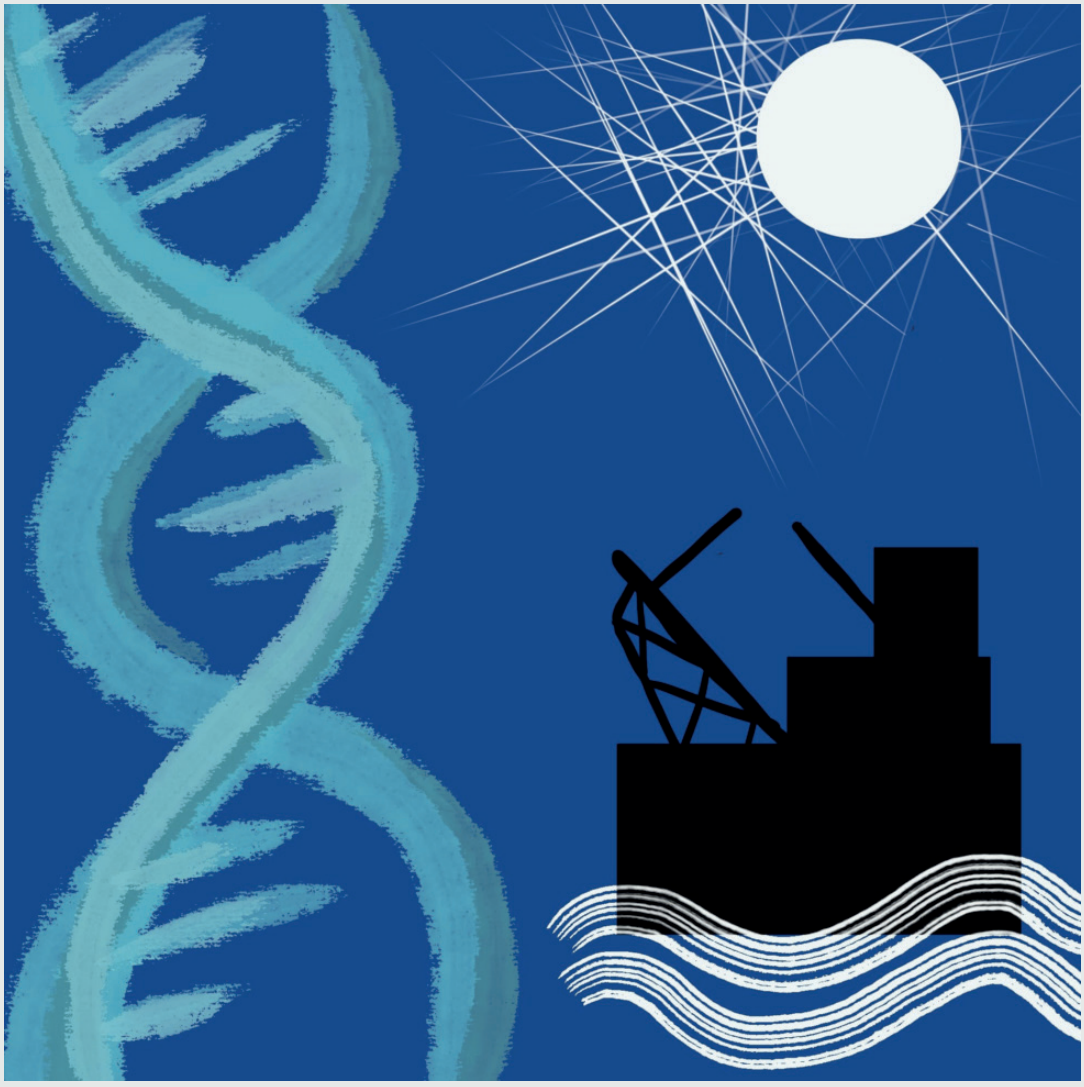

STUDIUM EDITORE

eCAMPUS UNIVERSITÀ

eCAMPUS UNIVERSITY PRESS

COSE

COASTAL AND OFFSHORE SCIENCE AND ENGINEERING

An International open-access Journal

Year III - VOL. 6 - 2024

ISSN : 2785-7972

Coastal and Offshore Science and Engineering is an internationally peerreviewed open access journal of coastal science and engineering published every 6 months online by STUDIUM. Readers of the Journal include engineers, geologists, ecologists, geographers, oceanographers, scholars and specialists who interest in coastal development, ecology, management and protection. The Journal provides new insights on coastal, port and offshore processes, function, design, performance, management, monitoring and restoration from an integrated, multi-/inter- disciplinary, multi-trophic and sustainable perspective. Coastal and Offshore Science and Engineering welcomes research and field case papers based on a wide range of topics by means of field, laboratory and experimental campaigns and remote sensing technology as well as mathematical and numerical modeling. The purpose is to encourage the development and application of holistic initiatives and novel concepts, methods, models and technologies; to elucidate the impact of multiple stressors (climate change, invasive species); to enhance knowledge about the engineering, geology and ecology and integrity of the coastal and offshore systems.

INDEX

Innovation, Monitoring and Data-Driven Approaches for a Resilient Coastal Future

The second 2024 Volume of Coastal and Ocean Science and Engineering (COSE) brings together a diverse yet conceptually cohesive collection of five scientific contributions that examine the evolving relationship between coastal observation, modelling, prediction, and risk assessment. This issue reflects a discipline in transition: as climate-driven pressures intensify, coastal engineering is increasingly shaped by integrated, data-rich methodologies capable of translating physical complexity into actionable insight.

Across the contributions gathered in this Special Issue, there is a clear convergence of advanced monitoring platforms, multi-scale numerical methods, artificial intelligence, and refined statistical analyses. Together, these tools are reshaping how coastal scientists interpret structural vulnerability, predict hydrodynamic processes, and manage escalating climate risk. The studies share a common ambition: to develop coastal systems that are not only better understood and more predictable, but also more resilient and adaptively managed.

The articles in this volume span a broad range of themes—from hybrid visual–aerial monitoring of maritime infrastructure, to bottom-up climate stress-testing, to neural-network-based wave forecasting, to statistical detection of tide–surge interactions, and finally to multi-sensor remote sensing for infrastructure assessment. Taken together, they exemplify a contemporary coastal engineering paradigm rooted in high-resolution observation, data assimilation, and anticipatory risk governance.

1. Systematic Observation and Digital Monitoring of Maritime Infrastructure

The first contribution presents an extensive application of LNEC's OSOM+ methodology, a modernised evolution of Portugal's long-standing systematic monitoring programme for rubble-mound breakwaters and maritime structures. By integrating GPS-referenced visual inspections, high-resolution drone photogrammetry, and a sophisticated web-based GIS platform (ANOSOM-WEB), the methodology provides a comprehensive digital framework for tracking structural performance and diagnosing early-stage anomalies.

Using the West Breakwater at the Port of Sines as a case study, the authors demonstrate how multitemporal photogrammetric products—orthomosaics, point clouds, digital surface models, and structural profiles—enable the detection of subtle armour-unit displacements and morphological adjustments. Crucially, OSOM+ transforms observational data into a decision-support system, allowing port authorities to schedule targeted maintenance based on quantitative assessments of structural evolution, risk condition, and spatially explicit diagnostics.

This work highlights a defining shift in contemporary coastal engineering practice: monitoring is no longer episodic, but continuous, spatially comprehensive, and digitally integrated—strengthening both operational preparedness and long-term resilience planning.

2. Bottom-Up Risk Assessment and Climate Stress-Testing for Future Flood Hazards

The second article offers a compelling comparison between top-down, scenario-driven climate assessments and bottom-up, vulnerability-focused frameworks, arguing for the complementary value of the latter under conditions of deep uncertainty. While top-down approaches ensure consistency with global climate projections, bottom-up methods excel at identifying local thresholds, adaptive capacities, and socio-environmental vulnerabilities that often determine real-world risk.

The authors show how participatory processes, fine-scale system mapping, and climate stress-testing can reveal critical tipping points—structural, social, or ecological—that remain invisible in scenario-based modelling alone. Their analysis reflects a broader conceptual shift: coastal risk assessment is evolving from a projection-centred exercise toward a resilience-oriented, locally grounded planning strategy.

In the context of accelerating sea-level rise and increasing storm impacts, this contribution underscores the need for hybrid frameworks that integrate climate science with site-specific knowledge and adaptive pathway planning, thereby fostering more flexible and robust adaptation strategies.

3. Artificial Intelligence for Nonlinear Wave Forecasting

The third contribution explores the growing interface between machine learning and phase-resolving wave modelling, demonstrating how neural networks can enhance the predictive skill of coastal wave forecasting systems. By training neural networks on hindcast datasets and high-fidelity nonlinear wave simulations, the authors successfully reconstruct complex wave dynamics, capturing short-term variability and nonlinear behaviour that are often underestimated by conventional approaches.

The study highlights several key advances:

- integration of artificial intelligence with deterministic hydrodynamic models;
- improved representation of nonlinear processes such as wave–wave interactions;
- enhanced forecasting at temporal scales relevant to harbour agitation, overtopping, and nearshore operations.

The resulting hybrid modelling framework illustrates how machine learning can augment—rather than replace—physics-based simulation. Together, these approaches offer strong potential for real-time forecasting systems capable of supporting coastal safety protocols and port operations under increasingly volatile meteorological conditions.

4. Detecting Tide–Surge Interaction in the Adriatic Sea

This study addresses a fundamental yet underexplored question for the Adriatic Sea: whether storm surges and astronomical tides interact statistically to influence extreme water levels. Applying three independent statistical frameworks—distributional analysis of extreme surges, timing relative to high tide, and correlation between skew surges and high tides—the authors analyse long-term tide-gauge records from the northern, middle, and southern Adriatic.

The results present a nuanced picture. While individual methods or locations exhibit weak indications of interaction, no consistent or robust evidence of tide–surge interaction emerges across all tests. This finding is particularly relevant in the context of the Adriatic's microtidal regime, where storm surges dominate extreme sea-level events.

By clarifying the limited role of tide–surge interaction in this basin, the study supports simplified modelling approaches in which tidal and surge components can be treated as largely independent—improving hazard quantification and flood-risk assessment.

5. Multi-Sensor Remote Sensing for Coastal Structure Assessment

The final contribution introduces an advanced RTK-anchored, multi-sensor remote-sensing workflow that integrates UAV-SfM, handheld SfM, smartphone LiDAR (sLiDAR), and terrestrial laser scanning into a unified monitoring framework for rubble-mound breakwaters. Beyond methodological innovation, the study presents a fully reproducible uncertainty-quantification protocol, incorporating hybrid M3C2 analyses and LoD95 detection thresholds.

The authors demonstrate:

- how different sensing platforms complement each other in terms of coverage, resolution, and access to occluded or porous zones;
- how multi-sensor co-registration yields engineering-grade point clouds suitable for as-built verification;
- how formalised uncertainty propagation supports defensible change detection.

By lowering technical and financial barriers to high-resolution monitoring, this workflow offers substantial benefits for routine coastal infrastructure management, enabling more frequent, accurate, and comprehensive assessments under increasing climate-related pressures.

Collective Themes and Emerging Directions

Several unifying themes emerge across the five contributions:

1. *The rise of high-resolution, multi-source coastal observation*

Drone photogrammetry, remote sensing, and multi-sensor point clouds are redefining how coastal structures and processes are monitored.

2. *Integration of data-driven and physics-based modelling*

Neural networks, statistical methods, and hydrodynamic models are increasingly combined to address complex nonlinear phenomena.

3. *Emphasis on uncertainty, thresholds, and systemic vulnerability*

Both bottom-up stress-testing and multi-sensor workflows highlight the importance of understanding failure conditions and risk propagation.

4. *Need for flexible, adaptive risk-management strategies*

As sea levels rise and storms intensify, adaptation planning must be iterative, locally grounded, and scenario-rich.

5. *A shift toward predictive and near-real-time capability*

AI-enhanced forecasting, high-frequency monitoring, and digital diagnostic platforms point toward a dynamic future for coastal risk assessment.

Concluding Remarks

Volume II (2024) of COSE, a special issue, offers a comprehensive snapshot of innovation at the intersection of monitoring, modelling, and coastal risk analysis. It portrays a discipline in evolution—moving toward predictive, high-resolution, and system-aware methodologies that are essential for addressing the challenges posed by climate change.

By advancing digital observation, hybrid modelling, and participatory risk assessment, the contributions in this Special Issue collectively strengthen the scientific foundations needed to design, manage, and safeguard coastal systems worldwide.

This volume serves both as a reflection of current progress and as an invitation to future research, collaboration, and innovation in support of more resilient coasts and communities.

Roberto Tomasicchio
University of Salento, Italy
Felice D'Alessandro
University of Milan, Italy
Dalibor Carević
University of Zagreb, Croatia
Damjan Bujak
University of Zagreb, Croatia

DOI: https://doi.org/10.53256/COSE_240201

Application of the OSOM+ Systematic Observation Methodology to Maritime Structures at the Port of Sines

R. Capitão[a, *], C.J.E.M. Fortes[a], R. Lemos[a], M.J. Henriques[a] and L.G. Silva[a]
[a] *LNEC - National Laboratory for Civil Engineering, Lisbon, Portugal*

[*] *Corresponding author: Address: LNEC, Avenida do Brasil 101, 1700-066 Lisbon, Portugal; email: rcapitao@lnec.pt*

ABSTRACT: The current OSOM+ methodology developed at LNEC - National Laboratory for Civil Engineering has been applied to the maritime and port infrastructure at the Port of Sines with the objective of monitoring structural performance and, when necessary, recommending timely maintenance interventions.

During monitoring campaigns, systematic photographic records were collected at georeferenced locations along each structure, and observed anomalies were identified. In addition, drone-based photogrammetric surveys were carried out, providing more detailed and accurate information on the condition of the structures. The integrated cloud-based GIS platform offers an intuitive and comprehensive online interface for data visualization, as well as a mobile interface that enables efficient on-site data input and real-time access to information stored in the maritime structures database.

This methodology has enabled the assessment of the current condition, evolution, and risk status of the port structures at Sines. Based on these evaluations, maintenance and repair actions can be planned in a timely and informed manner.

This paper compares the results of inspection campaigns conducted in 2018, 2020, 2022, and 2023 on the west breakwater, based on visual inspections and drone surveys, and supported by a critical analysis of georeferenced photographs, orthomosaics, point clouds, digital surface models, and cross-sectional profiles.

The results indicate that only minor displacements of armour units have been observed along the Sines west breakwater, which, to date, have been classified as non-significant anomalies.

KEYWORDS: Maritime structures, monitoring, visual inspection, drone survey, photogrammetry

1 INTRODUCTION

Since 1986, the National Laboratory for Civil Engineering (LNEC) has been developing the *Systematic Observation of Maritime Works* (OSOM) programme, aimed at monitoring the structural behaviour of rubble-mound breakwaters along the Portuguese continental coastline—namely the west and south coasts—as well as the island coastlines. The primary objective of the programme is the early identification of structural anomalies in maritime structures, thereby enabling timely maintenance and/or repair interventions while affected areas remain limited and remediation is simpler and more cost-effective.

The OSOM methodology was initially based on systematic visual inspection campaigns, which provided data for the former ANOSOM database (Reis et al., 1995; Lemos et al., 2007). This database supports the assessment of the current condition, condition evolution, and risk level of the monitored maritime structures. Since the 2010s, the OSOM programme has undergone significant developments. In 2017, with the integration of drone-based monitoring techniques, the programme evolved into OSOM+ (Capitão et al., 2018).

The use of unmanned aerial vehicles (UAVs) has substantially improved the accuracy and level of detail in structural condition assessments, allowing more reliable quantification of settlements, volume losses, and other structural changes affecting the monitored structures.

This paper presents LNEC's experience in visual inspection and drone-assisted monitoring of rubble-mound breakwaters and demonstrates the application of the OSOM+ methodology through a specific case study: the Port of Sines, where inspection activities began in 2018 (Fortes et al., 2019) under a contract established with the Port of Sines Authority (APS). Particular emphasis is

placed on the port's main protective maritime structure, the west breakwater.

THE PORT OF SINES

The Port of Sines is the largest artificial harbour in Portugal, operating as a deep-water port with natural bathymetries reaching depths of up to −28 m CD (Chart Datum), as shown in Fig. 1. Owing to its strategic geophysical characteristics, it serves as Portugal's main maritime gateway for energy supply, handling the import and export of containers, liquefied natural gas, coal, crude oil, and petroleum derivatives.

Figure 1. The Port of Sines

The port is equipped with specialised terminals designed for the efficient handling of various cargo types, all of which are protected by extensive rubble-mound breakwaters.
All breakwaters at Sines are monitored under the OSOM+ programme, including the west breakwater, the east breakwater, the marina breakwater, the fishing harbour breakwater, and the service port breakwater (see Fig. 2).
Among these, the west breakwater is the case study presented in this paper (outlined in yellow in the figure, while the remaining structures are shown in red). This breakwater suffered severe storm damage during 1978 and 1979, with progressive failure episodes that fractured and displaced large dolos armour units and undermined the superstructure, ultimately leading to extensive reconstruction works (Reis et al., 2011). Subsequent repair interventions included the use of heavy Antifer-type cubes on widened sections and gentler slopes, followed by a final redesign to meet updated 100-year return-period sea states. These interventions highlighted the importance of armour unit mechanical strength limits, placement density, and the risks associated with storm climate underestimation. Such lessons are consistent with broader assessments of concrete armour integrity, which emphasise size-effect fragility and the need for structural and hydraulic verification beyond notional stability numbers (Scaravaglione et al., 2022; Leone et al., 2024). These considerations strongly motivate the implementation of systematic monitoring approaches, such as the one described in this study.

Figure 2. Rubble-mound breakwaters at the port of Sines

The breakwaters protect a wide range of critical infrastructures, including five specialised terminals (liquid bulk, petrochemical, dry bulk, liquefied natural gas, and container terminals), a logistics activity zone, the fishing harbour, and the leisure marina.
From a structural perspective, each breakwater consists of a core of finer material overlain by an armour layer composed of large units. In the more exposed sections, the armour layer comprises concrete units of various geometries—such as tetrapods, Antifer cubes, or parallelepipeds—to enhance stability and wave energy dissipation. The superstructures of the breakwaters are constructed in reinforced concrete. Access conditions vary across the structures: while some breakwaters are publicly accessible, others are located within restricted operational areas with limited or prohibited public access.

OSOM+ METHODOLOGY

Introduction

The OSOM+ methodology was developed to support infrastructure owners in the systematic monitoring of breakwaters and other maritime structures, enabling the timely recommendation of maintenance and/or repair interventions. It integrates systematic visual inspection campaigns with drone-based photogrammetric surveys, providing comprehensive and up-to-date information on structural behaviour and evolution. All collected data are stored in the ANOSOM database (Maia et al., 2017), which supports the characterization of each structure's *Present Condition*, *Evolution Condition*, and *Risk Condition*. This diagnostic framework enables informed decision-making regarding the timing,

location, and urgency of required maintenance or repair works.

More recently, the development of the ANOSOM-WEB interface has introduced a web-based GIS platform accessible from any internet-connected device (smartphone, tablet, or computer). During field campaigns, inspectors can use this platform to review data from previous inspections, access real-time condition assessments, and determine whether immediate intervention is required (Fig. 3).

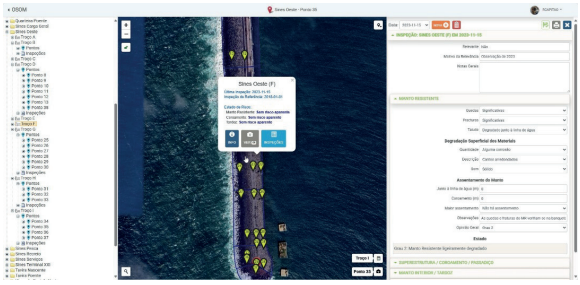

Figure 3. ANOSOM-WEB interface showing the west breakwater of the Port of Sines

Currently, OSOM+ comprises four main components:

- Periodic **visual inspections** conducted by trained personnel, including systematic GPS-tagged photographic and video documentation;
- Periodic **UAV-based aerial surveys** using vertically oriented imagery;
- The **ANOSOM-WEB database**, which stores all inspection data and supports condition assessment and diagnostic analyses;
- A **mobile application** that enables *in situ* data entry and real-time access to inspection results.

OSOM+ visual and UAV inspection campaigns systematically observe the emerged parts of the breakwaters, with surveys deliberately scheduled during low-tide conditions to maximise armour exposure and reduce surf-zone interference in geospatial products. It should be noted, however, that the absence of routine submerged monitoring may bias diagnostic assessments by failing to capture toe scour, filter exposure, or settlement patterns—mechanisms that have historically contributed to significant damage in concrete-armoured structures, including the west breakwater at Sines, as discussed previously. Nevertheless, ANOSOM-WEB already supports the integration of "surveys of emerged and submerged zones," enabling the future incorporation of multibeam bathymetry, side-scan sonar, ROV or diver inspections, and subsea photogrammetry to address this limitation (Reis et al., 2011).

Visual inspection

Visual inspections provide a rapid and intuitive means of monitoring the structural behaviour of rubble-mound breakwaters over time. These inspections, following the methodology outlined by Santos et al. (2003), are typically conducted on an annual basis and additionally after the occurrence of severe storm events that may have affected the structural integrity of the structure as a whole or of individual components.

To enhance the reliability and consistency of observations, each breakwater is subdivided into distinct sections defined according to their specific physical and functional characteristics. In general, each section corresponds to a unique structural cross-section, with the breakwater head always defined as an individual section. For each section, a set of observation points is established and marked directly on the structure. During each inspection campaign, photographs and/or videos are acquired from these predefined locations using consistent photographic parameters—including camera focal length, viewing direction and angle, and framing—to allow direct comparison over time.

To ensure optimal visibility of the armour layers and filters (where present), visual inspections are preferably carried out at low tide. In addition, for safety reasons, inspections are conducted only under favourable weather conditions, ideally when the sea state is calm, thereby reducing the risk of accidents to inspection personnel.

Aerial inspection

The use of Unmanned Aerial Vehicles (UAVs), or drones, as demonstrated by Henriques et al. (2024), has significantly enhanced the accuracy and level of detail of structural condition assessments of rubble-mound breakwaters. UAV-based surveys enable the acquisition of comprehensive data on the evolution of the structural envelope and facilitate the extraction of representative profiles in critical areas. Each UAV campaign produces high-resolution nadir aerial images captured along regular flight patterns. These images are processed to generate point clouds, digital surface models (DSMs), and orthomosaics, which complement ground-based visual inspections by providing additional perspectives, particularly in areas not readily accessible to inspectors walking on the structure.

At LNEC, the initial UAV surveys conducted in 2017 employed a DJI Inspire V1 platform. Subsequent campaigns adopted the DJI Matrice 300 RTK, significantly improving flight stability and operational safety, particularly under moderate to strong wind conditions (up to 54 km h^{-1}). From 2020 onwards, the integration of Real-Time Kinematic (RTK) positioning further enhanced positional accuracy and overall survey reliability.

Prior to 2020, UAV flights typically covered the full length of each breakwater, from head to root, while avoiding sensitive infrastructure (e.g. gas and petrochemical pipelines). Following 2020, compliance with updated European regulations required maintaining a minimum distance of 150 m from buildings, which in some cases reduced survey coverage. To compensate for these restrictions, oblique image acquisition from flight paths over the sea was implemented to ensure adequate coverage of the structures.

Typical flight parameters include altitudes of 30–40 m and approximately 80% longitudinal and transverse image overlap. Flights are autonomous (pre-programmed) and are conducted during low-tide conditions to maximise exposure of the armour layer.

All necessary authorisations were obtained in advance from the relevant national authorities, including the National Aeronautical Authority (ANA), local Port Authorities, aerodrome and heliport authorities, and, where applicable, the Institute for Nature and Forest Conservation (ICNF).

Weather conditions were closely monitored in the five days preceding each flight using official meteorological forecasts, with particular attention given to wind speed and gusts.

The ANOSOM-WEB database

The ANOSOM-WEB database, derived from the earlier ANOSOM system (Reis & Silva, 1995; Santos et al., 2003; Lemos & Santos, 2007), has undergone substantial development through the integration of a GIS-based interface aimed at improving the efficiency of querying and analysing information for each breakwater section. It is now implemented as a web-based Geographic Information System (GIS) platform that enables the centralised management, access, and analysis of all observational data. The platform is accessible from any internet-connected device (smartphone, tablet, or personal computer) and was developed using modern web technologies, including PHP/Laravel for backend development, JavaScript with Bootstrap and jQuery for frontend interactivity, and Leaflet for spatial data visualisation and map integration (Maia et al., 2017). The GIS functionalities are supported by MySQL spatial extensions, which enable efficient storage, querying, and manipulation of georeferenced datasets.

The system supports the import and visualisation of standard geospatial formats, such as shapefiles, and integrates cartographic layers from third-party services, including ESRI/ArcGIS. This allows users to visualise inspection data directly over accurate basemaps and customised site plans. Key functionalities include interactive spatial mapping, attribute querying, and retrieval of historical records, which together facilitate spatio-temporal analysis of structural condition. In addition, the platform provides structured input forms for both visual inspection and UAV survey data, which are georeferenced and linked to individual structural components or sections. This enables a seamless workflow from field data acquisition to analytical diagnosis, ensuring that maintenance decisions are based on comprehensive and up-to-date information.

The ANOSOM-WEB platform provides the following core functionalities:

a) Storage and analysis of visual inspection and UAV survey data, as well as other structural inspection inputs (e.g. surveys of emerged and submerged zones);

b) Diagnostic assessment of each breakwater section, including *Present Condition*, *Evolution Condition*, and *Risk Condition*, based on predefined and calibrated evaluation criteria (Santos et al., 2003);

c) Consultation of historical records, including design documentation, past interventions, hydrographic and aerial surveys, and underwater inspections;

d) Physical characterisation of each section, including geometry, construction materials, and standard cross-sectional configurations.

The platform enables real-time diagnosis of structural condition, allowing on-site users to assess whether immediate maintenance or repair actions are required. Figure 4 illustrates the interface's capability to retrieve photographs and related information linked to specific locations and inspection events. Initially populated with design-phase data, the database has since been continuously updated with results from systematic inspection campaigns and records of structural modifications following major interventions.

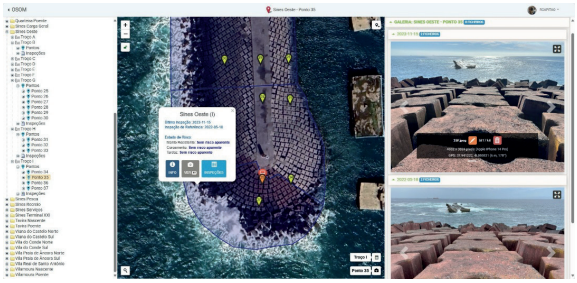

Figure 4. ANOSOM-WEB interface showing photographs and related information for the west breakwater at the Port of Sines (point 35, section I, head)

APPLICATION TO THE SINES WEST BREAKWATER

Integrated visual and UAV monitoring

This section presents the application of the OSOM+ methodology to the monitoring of the west breakwater at the Port of Sines. The analysis integrates inspection data obtained from four monitoring campaigns conducted in 2018, 2020, 2022, and 2023. These campaigns combined traditional systematic visual inspections with drone-based (UAV) surveys.

The comparative assessment is based on a comprehensive set of geospatial products, including georeferenced photographs, orthomosaics, dense point clouds, digital surface models (DSMs), as well as longitudinal and transversal profiles. Together, these products enable a detailed and multi-dimensional interpretation of the structural evolution of the breakwater over time.

This integrated monitoring approach allows the detection of subtle morphological changes, the quantification of structural displacements, and the evaluation of the overall condition of the armour layer with increased accuracy. The combination of UAV-derived data with systematic visual inspections ensures a robust and cross-validated interpretation of physical changes, thereby supporting more reliable decision-making for maintenance planning and risk management at the Port of Sines.

Visual inspection

For the visual inspection campaigns, the west breakwater was subdivided into nine sections (A to I), according to the distinct physical and functional characteristics of the structure. Within each section, several georeferenced observation points were defined, with their number varying according to the extent of the section and the presence or clarity of identified anomalies (Fig. 5).

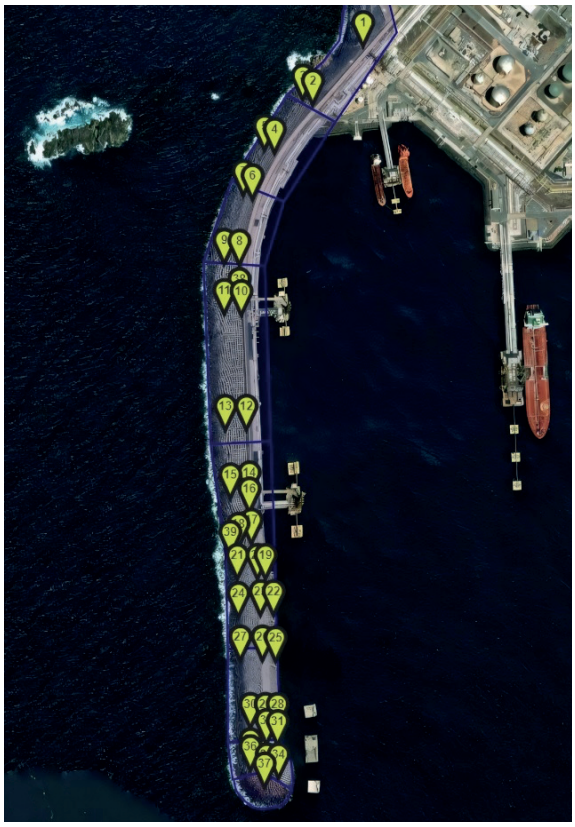

Figure 5. Sines west breakwater showing the division into sections (A to I) and visual reference points (1 to 37)

For each section, a qualitative assessment of the current structural condition was carried out, focusing on the state of the armour layer, the superstructure, and the inner filter layers. Observations included aspects such as armour unit displacement, block fractures, and material degradation, which were recorded using predefined qualitative scales (e.g., for unit displacement: none, few, some, many).

Figures 6, 7, and 8 present photographs taken during the 2018, 2020, and 2022 inspection campaigns, respectively, at predefined observation points on the Sines west breakwater. These include point 27 on the seaward side of section G, point 28 on the harbour-side of section G, and point 37 at the breakwater head (section I). Comparisons between the 2018, 2020, and 2022 campaigns revealed some localized structural changes, which are illustrated in Figures 9 and 10. These figures show photographs from the locations where the most relevant changes were detected, namely section F at point 24 (Fig. 9) and section F at point 27 (Fig. 10). In both cases, block breakage was observed between successive inspection campaigns.

Figure 6. 2018 visual observation at point 27F (F – front direction) of the Sines west breakwater (outer armour layer)

Figure 7. 2020 visual observation at point 28F of the Sines west breakwater (inner armour layer)

Figure 8. 2022 visual observation at point 37T (T – back direction) of the Sines west breakwater (head, section I)

Overall, based on the in situ visual inspections conducted in 2022, no significant changes in the general condition of the breakwater were identified when compared with the 2018 and 2020 surveys. Some localized alterations, such as isolated broken blocks and minor armour unit displacements, were observed; however, these were classified as non-significant and do not compromise the overall structural integrity of the breakwater.

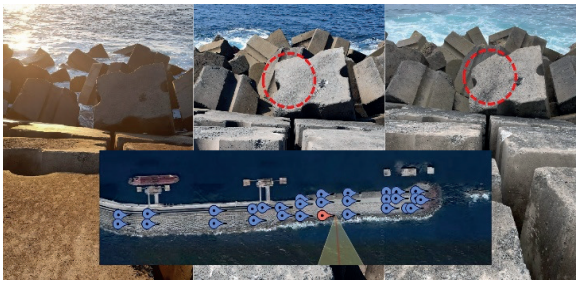

Figure 9. Visual observation at point 24L (L – lateral direction) of the Sines west breakwater (2018–2020–2022). Broken Antifer block observed between 2020 and 2022

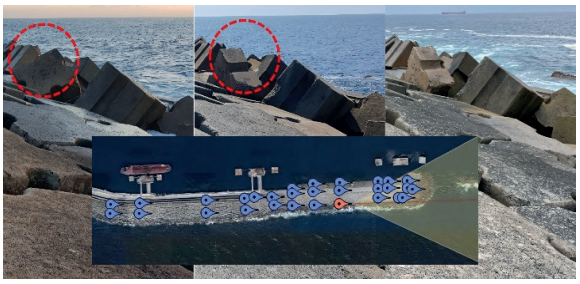

Figure 10. Visual observation at point 27F of the Sines west breakwater (2018–2020–2022). Broken Antifer block observed between 2018 and 2020

Aerial inspection

For the aerial inspection of the structure, the required equipment consisted of an Unmanned Aerial Vehicle (UAV) system operated in conjunction with dedicated flight control and mission-planning software. The initial survey campaign, conducted in 2018, employed a DJI Inspire V1 platform equipped with a Zenmuse X3 camera (12 MP). In the subsequent campaigns of 2020 and 2022, the system was upgraded to a DJI Matrice 300 RTK fitted with a Zenmuse H20 payload (wide-angle and 20 MP zoom cameras with integrated laser rangefinder). This upgrade significantly improved flight stability, positional accuracy, and operational safety, particularly under moderate to strong wind conditions (Fig. 11).

Figure 11. LNEC DJI Matrice 300 RTK UAV

To ensure accurate photogrammetric processing, Ground Control Points (GCPs) were established and surveyed using GNSS technology. These points were clearly marked to ensure visibility in the UAV imagery. In addition, a set of independent Check Points (CPs) was defined to assess the geometric accuracy of the resulting models (Fig. 12).

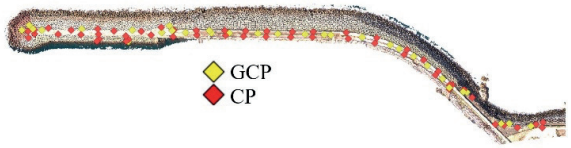

Figure 12. Location of GCPs and CPs on the Sines west breakwater

Flight operations were managed using the DJI Pilot application, which was employed for mission planning, system configuration, and sensor calibration to ensure optimal image acquisition. During flight execution, the software also provided real-time UAV control, obstacle-proximity warnings, and automated collision-avoidance functions (Figs. 13 and 14).

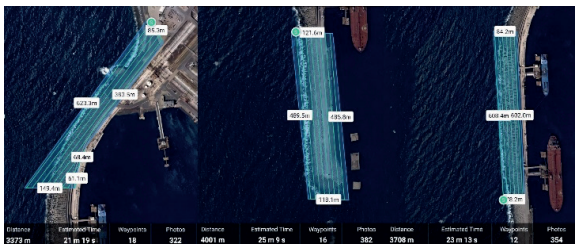

Figure 13. Flight plans over the Sines west breakwater

Figure 14. UAV operator preparing a flight on the Sines west breakwater; the RTK GNSS base antenna is visible at the top of the image

Following each survey, the acquired imagery was processed using Agisoft Metashape (Agisoft LLC), a photogrammetric software package used to generate dense point clouds and Digital Surface Models (DSMs). The resulting DSMs were subsequently analysed in QGIS (GPL licence), which provided the tools required for spatial comparison and change detection.

To identify localised structural changes between the 2018, 2020, and 2022 campaigns, successive DSM comparisons were performed by generating differential DSMs (d-DSMs). These products revealed areas of material loss and deposition. To enhance visual interpretation, the colour scale of the d-DSMs was adjusted to highlight zones exhibiting significant changes.

All dense point clouds, DSMs, and orthomosaics were referenced in the ETRS89 / PT-TM06 coordinate system to ensure spatial consistency across survey epochs. An example of the comparison results is shown in Fig. 15, illustrating DSM differences after outlier filtering. Most excluded points were associated with the waterline, where noise and reflection effects are more pronounced.

Figure 15. Results of DSM differencing between 2018–2020 and 2020–2022 after outlier removal

The processing workflow followed a sequential procedure applied to each breakwater section and survey campaign: (i) generation of the dense point cloud; (ii) computation of the DSM and storage in matrix format (Fig. 16); and (iii) production of the orthomosaic (Fig. 17).

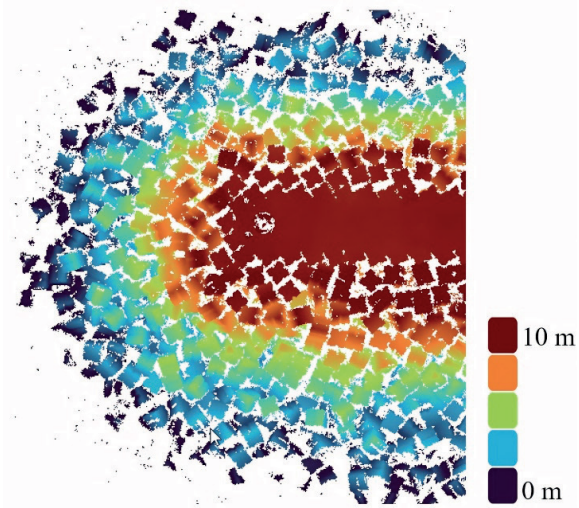

Figure 16. DSM (matrix representation) of the head section of the Sines west breakwater

Figure 17. Detail of the orthomosaic of the Sines west breakwater (head section)

For reporting purposes and to facilitate visual interpretation, the dense point clouds were also converted into three-dimensional meshes (see Fig. 18).

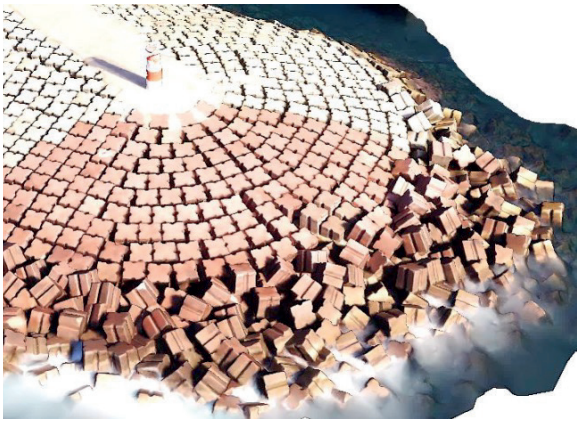

Figure 18. Mesh representation of the head section of the Sines west breakwater

Figures 19 and 20 present, as examples, the maps of detected changes and the corresponding orthomosaics for 2020 and 2022 in sections where relevant modifications were identified. In the adopted colour scale, red indicates material loss, while blue represents material deposition. These analyses were carried out in QGIS, which also served as the primary platform for visualising orthomosaics and DSMs, owing to its robust capabilities for handling and displaying georeferenced raster data and for enhancing topographic features through colour manipulation.

Figure 19. West breakwater. Changes detected between 2020 and 2022 – Occurrence 2 – Section E

Figure 20. West breakwater. Changes detected between 2020 and 2022 – Occurrence 3 – Section G

As previously noted, changes in the armour layer geometry were identified through DSM differencing: subtracting one DSM from another highlights spatial variations, enabling both qualitative interpretation and quantitative assessment of structural evolution. This analysis was performed entirely within the QGIS environment.

Figures 21 to 23 show selected orthomosaic excerpts illustrating specific types of detected changes. The associated DSM differences are represented using colour maps, allowing clear visualisation of localised morphological evolution.

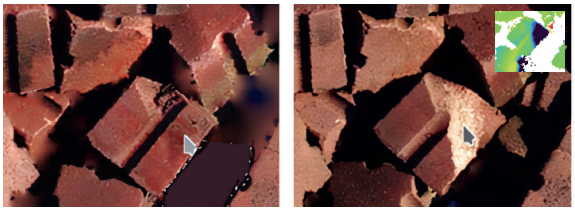

Figure 21. Armour unit exhibiting increased erosion between 2020 and 2022

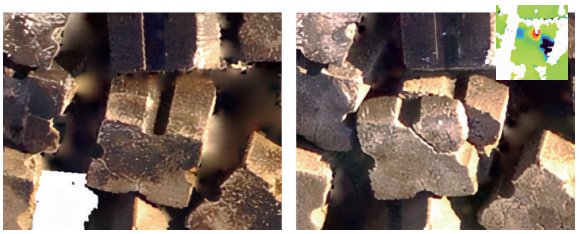

Figure 22. Armour unit failure observed between 2020 and 2022

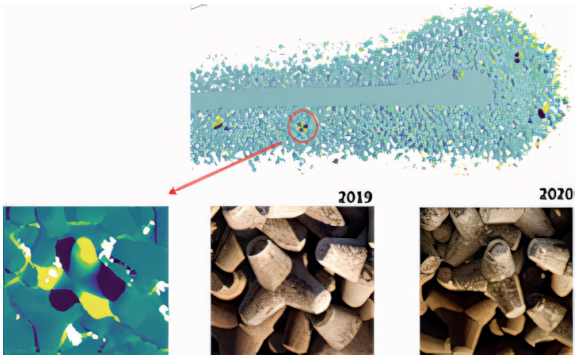

Figure 23. Tetrapod rotation observed between 2019 and 2020

Profiles

Point clouds, supported by orthomosaics, were used to extract accurate cross-sectional profiles of the structure. Transversal profiles were generated along predefined cross-shore sections, oriented perpendicular to the longitudinal axis of the breakwater.

The location and spacing of these sections were selected to cover representative areas of the structure and were kept consistent across survey campaigns to enable reliable temporal comparison. Profile planes were defined by first establishing a baseline polyline along the crest of the breakwater, using the orthomosaic as a spatial reference. Subsequently, a set of normal vectors was defined at regular intervals along this baseline, indicating the direction of each transversal cut (see Fig. 24). An example of the extracted profiles is shown in Fig. 25.

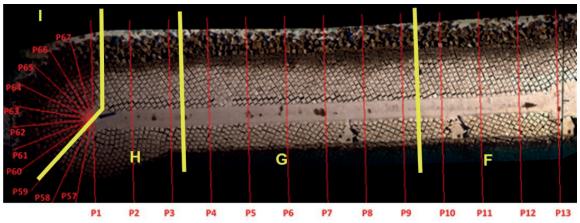

Figure 24. Sines west breakwater: location and details of the extracted profiles, sections F to I (head)

Profile comparison allows the detection of geometric changes in the most vulnerable sections of the structure between consecutive survey campaigns. For the Sines west breakwater, only negligible or no changes were observed between successive profiles.

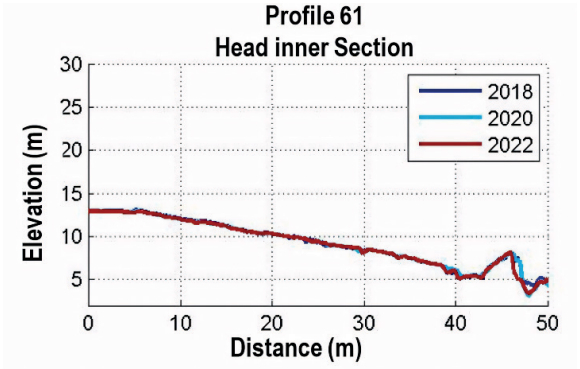

Figure 25. Example of extracted profiles (Profile 61 at the head of the breakwater)

When analysing the profiles, particular attention should be paid to the following factors, as they may contribute to discrepancies between surveys:

- higher quality of image acquisition and point clouds in the 2020 and 2022 surveys compared to 2018;
- slight differences in tidal levels between inspection campaigns;
- potential misalignment of point clouds due to inherent uncertainties in photogrammetric processing;
- increased uncertainty in surf-zone areas that are partially or fully submerged;
- local limitations in image acquisition caused by the presence of vessels, pipelines, mooring equipment, or other obstructions.

In summary, since 2018, only minor and non-significant displacements of armour units have been observed along the Sines west breakwater. As with all maritime structures of this type, it remains essential to monitor such minor

anomalies and, whenever feasible, restore the structure to its original as-built condition.

CONCLUSIONS

Overall, the OSOM+ framework, enhanced by the integration of UAV-based survey capabilities and the development of new digital tools, represents a significant improvement in both the operational efficiency and analytical depth of systematic coastal infrastructure monitoring. Periodic visual inspections, when combined with UAV-derived datasets, enable a more robust assessment of present conditions, structural evolution, and risk indicators. In addition, the deployment of a mobile, field-ready application during inspection campaigns streamlines data acquisition and improves workflow integration.

For the Port of Sines, this study highlights the substantial contribution of visual inspections and aerial photogrammetric surveys to the monitoring of rubble-mound breakwaters. The imagery acquired during visual inspection campaigns and the data products derived from UAV surveys—particularly digital surface models (DSMs), point clouds, and orthomosaics—significantly enhance the capacity to quantify structural evolution within the OSOM+ programme.

Originally grounded in qualitative assessments, the methodology has evolved to incorporate higher-resolution data and increasingly quantitative analyses. With the current level of precision achievable through drone-based surveys, structural changes on the order of a few centimetres can now be detected with confidence. This represents a critical step forward in the early identification of potential risks and supports more reliable long-term management of coastal infrastructure.

Although this study focused on the monitoring of existing maritime structures, the applicability of the methodology extends beyond this scope. The same survey techniques can support verification of as-built geometry during construction or repair phases, which is essential for quality control and contractual validation.

This enhanced monitoring approach benefits both the data provider (LNEC) and the primary end users, namely Port Authority Administrations—specifically, in this case, the Port of Sines Authority (APS). The transition towards a predominantly quantitative monitoring framework yields more precise, objective, and actionable insights into the condition and performance of maritime structures.

ACKNOWLEDGEMENTS

This work was supported by the Port of Sines Authority (APS) under contracts 2018–2022 and 2023–2027, and by LNEC research projects SAFEPORT – Risk and Safety in Ports and Maritime Structures and RISK – Risk Assessment of Maritime Infrastructures.

REFERENCES

Capitão, R., Lemos, R., Henriques, M.J., Fortes, C.J.E.M., Neves, M.G., Silva, L.G. & Reis, M.T. (2018). Systematic observation of maritime works. The new OSOM+. In *Proc. 5as Jornadas de Engenharia Hidrográfica*, Instituto Hidrográfico.

Fortes, C.J.E.M.; Capitão, R., Lemos, R.; Neves, M.G.; Silva, L.G.; Henriques, M.J.; Martins, T. (2019). Sines breakwater harbour: The OSOM+ monitoring program. SCACR2019 – International Short Course/Conference on Applied Coastal Research Engineering, Geology, Ecology & Management 9th – 11th September 2019 – Bari, Italy.

Henriques, M.; Capitão, R.; Fortes, C.; Lemos, R.; Silva, L.; Silva, H. and Gonçalves, R. (2024). The Contribution of Drones to the Monitoring of Rubble-Mound Breakwaters. In Proceedings of the 10th International Conference on Geographical Information Systems Theory, Applications and Management - GISTAM; ISBN 978-989-758-694-1; ISSN 2184-500X, SciTePress, pages 160-167. DOI: 10.5220/0012691200003696

Lemos, R., Santos, J.A. (2007). ANOSOM - Análise da observação sistemática de obras marítimas. In *5as Jornadas Portuguesas de Engenharia Costeira e Portuária*, PIANC. (In Portuguese).

Leone, L; Francone, A.; Paglialunga, A.; Ciardulli, F.; Long, J.; Aloisi, A.; Tomasicchio, G.R.. "Overtopping Assessment of a Rubble Mound Breakwater with Innovative Armor Units: A Physical and Numerical Study," Journal of Coastal Research, 113(sp1), 804-808, (20 December 2024)

Maia, A., Rodrigues, A, Lemos, R., Capitão, R., Fortes, C.J.E.M. (2017). A Web platform for the systematic monitoring of coastal structures. In *GISTAM 2017*, SCITEPRESS.

Reis, M.T., Silva, L.G (1995). Systematic Observation of Maritime Works. ANOSOM Database: User's Manual. *Report NPP*, LNEC.

Reis, M.T.; Neves, G.; Robert, M., Hu, K.; Silva, L.G.; Rehabilitation of Sines west breakwater: wave overtopping study. Maritime Engineering 1 March 2011; 164 (1): 15–32. https://doi.org/10.1680/maen.2011.164.1.15

Santos, J.A.; Neves, M.G.; Silva, L.G. (2003). Rubble-mound breakwater inspection in Portugal. In Proc. Coastal Structures '03, Melby, J.F. (Ed.), Portland, ASCE, pp. 249-261.

Scaravaglione, G. Latham, J.P.; Xiang, J.; Francone, A.; Tomasicchio, G.R. (2022). Historical overview of the structural integrity of Concrete Armour Units. Coastal and Offshore Science and Engineering, Vol. 1-2022

DOI: https://doi.org/10.53256/COSE_240202

Bottom-Up Approach for Flood Risk Assessment in Coastal Areas

E. Leone[a,*], A. Francone[b], A. Paglialunga[a], A. Lauria[b], S. De Bartolo[b], W. Hamza[c], G.R. Tomasicchio[b]
[a]*eCampus University, Novedrate, Como, Italy*
[b]*Department of Engineering for Innovation, University of Salento, Lecce, Italy*
[c]*Biology Department, Faculty of Sciences, United Arab Emirates University, Al-Ain, UAE*

[*]*Corresponding author: elisa.leone@uniecampus.it*

ABSTRACT: Coastal flood risk assessment under climate change increasingly requires the integration of multiple methodological approaches to address both global uncertainty and local specificity. This paper compares two complementary frameworks: a traditional top-down, scenario-driven approach based on downscaled climate projections, and a bottom-up, vulnerability-focused approach grounded in local knowledge and participatory engagement. Particular emphasis is placed on the bottom-up methodology, highlighting its ability to identify site-specific thresholds, capture socio-environmental dynamics, and assess adaptive capacity through stakeholder involvement and climate stress-testing. By analysing the respective strengths and limitations of each framework, the study demonstrates the added value of an integrated assessment strategy that improves the robustness, flexibility, and responsiveness of coastal adaptation planning. Finally, the paper highlights the role of iterative and flexible decision-support tools—such as adaptation pathways—in bridging long-term climate projections with actionable, locally tailored risk reduction and adaptation measures.

KEYWORDS: Risk assessment; coastal engineering; bottom-up approach

1 INTRODUCTION

Coastal regions worldwide are experiencing increasing pressure as a result of the rapid and accelerating rise in mean global sea level. Since the early twentieth century, global mean sea level has risen by approximately 0.2 m, with the rate of increase accelerating from about 1.3 mm yr^{-1} during the twentieth century to more than 3.7 mm yr^{-1} in recent decades. Satellite altimetry observations since 1993 confirm a clear acceleration in the twenty-first century, with rates exceeding 4.5 mm yr^{-1} over the last decade (IPCC, 2021). This ongoing sea-level rise (SLR), primarily driven by ocean thermal expansion and land-ice melt associated with global warming, is unprecedented over at least the past three millennia.

The implications for low-lying coastal areas are profound and include more frequent and severe coastal flooding, accelerated shoreline erosion, saltwater intrusion into freshwater systems, and the compounding of multiple coastal hazards that threaten both ecosystems and human settlements (Griggs and Reguero, 2021). Densely populated river deltas, small island developing states, and gently sloping low-elevation coastlines are among the most vulnerable regions. Many of these areas are characterized by extensive development located only a few metres above present mean sea level and often lack natural protective features, making even relatively modest SLR particularly hazardous.

This context underscores the urgent need for integrated and robust approaches to assess and reduce coastal vulnerability in a warming climate. Risk assessment constitutes a fundamental component of effective coastal adaptation planning. Broadly, two methodological paradigms have emerged for the assessment of climate-related coastal hazards: top-down (scenario-driven) and bottom-up (vulnerability-driven) frameworks (Hinkel et al., 2018). The top-down approach typically begins with global or regional climate scenarios and numerical models to project future hazards (Di Risio et al., 2017; Skinner, 2024). In contrast, the bottom-up approach focuses on local conditions, examining site-specific vulnerabilities, exposure, and adaptive capacity within coastal systems (Padulano et al., 2021; Guan et al., 2023).

Each approach provides valuable yet distinct insights; when applied in combination, they can yield a more comprehensive and robust

characterization of coastal risk. The present paper examines and compares these two methodologies, with particular emphasis on their applicability to low-lying coastal areas under climate change. First, recent trends and future projections of sea-level rise—recognized as a key driver of intensifying coastal hazards—are reviewed. The analysis then explores the structure, strengths, and limitations of both top-down and bottom-up risk assessment frameworks. Finally, attention is given to integrated strategies, such as adaptive pathway planning, which are especially well suited to managing long-term uncertainty. The discussion is framed within the broader context of coastal engineering and environmental science, with the objective of supporting more resilient infrastructure design and evidence-based policy-making in climate-exposed coastal zones.

2 SEA-LEVEL RISE TRENDS

2.1 Observed Trends

Long-term records derived from tide gauges and satellite altimetry reveal a clear acceleration in sea-level rise (SLR). During the twentieth century, global mean sea level increased at an average rate of approximately 1–2 mm yr^{-1}, corresponding to a total rise of about 15–25 cm between 1900 and 2018. This long-term increase has not been linear; rather, the rate of rise has intensified markedly in recent decades.

Satellite observations, available since 1993, indicate a mean global sea-level rise of approximately 3.3 mm yr^{-1} over the past 30 years—nearly three times the rate observed in the early twentieth century. Moreover, the rate of rise continues to accelerate. During the most recent decade (2013–2023), the observed rate exceeded 4.5 mm yr^{-1} (IPCC, 2021). Consistently, the World Meteorological Organization reported an average rise of about 4.8 mm yr^{-1} over the period 2014–2023, compared with approximately 2.1 mm yr^{-1} in the early 1990s. As a result, by 2023, global mean sea level reached its highest value in the modern satellite record, standing roughly 9–10 cm above the 1993 baseline.

Anthropogenic warming has been identified as the dominant driver of accelerated SLR since at least the 1970s, primarily through the combined effects of land-ice melt and ocean thermal expansion. The current rate of sea-level rise exceeds any observed during the past 3,000 years, underscoring the unprecedented nature of contemporary changes.

Although regional and local sea-level trends may deviate from the global mean due to processes such as land subsidence or uplift, tectonic activity, ocean circulation variability, and gravitational redistribution of water mass, the vast majority of coastal regions are experiencing rising sea levels to varying degrees. This widespread increase significantly amplifies the exposure of vulnerable coastlines to high tides, storm surges, and associated coastal hazards worldwide.

2.2 Future Projections

Projections of global mean sea-level rise (SLR) depend primarily on future greenhouse gas emission pathways and the response of polar ice sheets. The Intergovernmental Panel on Climate Change (IPCC) Sixth Assessment Report (AR6) provides scenario-based projections of global mean SLR through 2100 and beyond. Figure 1 (from AR6) illustrates the median projected SLR under several Shared Socioeconomic Pathway (SSP) scenarios, together with likely uncertainty ranges (17th–83rd percentiles) and broader possible bounds. It is important to note that the IPCC is not a research institution; rather, it synthesizes and assesses findings from peer-reviewed scientific literature and technical reports produced by climate change experts worldwide. Consequently, the SLR projections presented in AR6 reflect the current scientific consensus as well as the associated uncertainties identified across the broader research community .

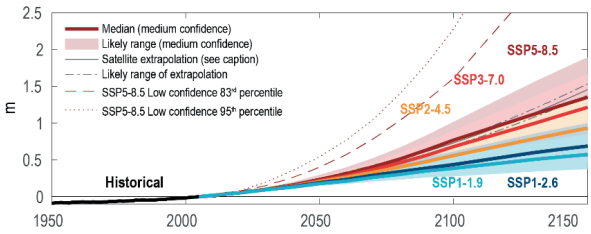

Figure 1. Global mean SLR projections under different emissions scenarios (SSPs), incorporating historical observations and future estimates with associated uncertainty ranges. Source: IPCC (2021), AR6, Chapter 9, Figure 9.27).

Under a low-emissions, high-mitigation scenario consistent with the Paris Agreement (SSP1-1.9, corresponding to approximately +1.5 °C of global warming), the IPCC projects a likely global mean SLR of about 0.28–0.55 m by 2100 relative to 1995–2014 levels. For an intermediate emissions

scenario (SSP2-4.5), global mean sea level is projected to rise by approximately 0.5 m by 2100. In a high-emissions scenario with limited climate policy (SSP5-8.5), global mean sea level is projected to increase by 0.63–1.01 m by 2100, with a median estimate close to 0.77 m.

Beyond 2100, the divergence between scenarios becomes increasingly pronounced. By 2150, median SLR under the high-emissions scenario approaches 1.5 m, while the upper end of the very likely range may approach 2 m if certain ice-sheet instabilities are triggered. Uncertainty in ice-sheet response dominates high-end SLR projections for the late twenty-first century and beyond (Bamber et al., 2019). In particular, the dynamics of the Greenland and West Antarctic ice sheets remain poorly constrained. Processes such as marine ice-sheet instability and marine ice-cliff instability could lead to substantially greater sea-level contributions if critical temperature thresholds are exceeded.

Although the IPCC's likely range under SSP5-8.5 by 2100 extends to approximately 1 m, several studies indicate that SLR on the order of 1.5–2.0 m by 2100 cannot be ruled out if ice-sheet collapse processes accelerate. These outcomes are considered low-probability but high-impact scenarios (Bamber et al., 2019; DeConto et al., 2021). From a coastal risk management perspective, such tail-risk scenarios warrant careful consideration due to their potentially catastrophic implications for low-lying coastal regions and island nations.

Future SLR projections are characterized by deep uncertainty, particularly with respect to the timing and magnitude of ice-sheet mass loss, for which expert consensus remains limited. This uncertainty affects confidence in long-term projections and underscores the importance of considering a wide range of plausible futures. Projected outcomes vary substantially depending on emissions pathways and the sensitivity of polar ice masses to warming.

Moreover, translating global mean SLR projections to regional and local scales requires accounting for multiple modifying factors, including vertical land motion (e.g., subsidence or uplift), regional oceanographic conditions (e.g., circulation patterns and wind forcing), and gravitational and rotational effects. Ongoing research is progressively improving the accuracy of regional and local SLR estimates, which is essential for impact assessment and adaptation planning.

Recent methodological advances aim to strengthen the linkage between large-scale climate projections and site-specific sea-level responses. For example, Tomasicchio et al. (2018) proposed a direct scaling approach that relates projected global mean SLR to observed trends at individual tide-gauge stations. Using long-term observational records, they demonstrated consistent acceleration in local SLR and derived site-specific projections aligned with global estimates. Similarly, Kopp et al. (2023) introduced the FACTS (Framework for Assessing Changes to Sea Level) platform, a flexible and modular system for probabilistic SLR assessment. This framework explicitly accounts for both statistical and structural uncertainties, with particular emphasis on the role of Antarctic and Greenland ice-sheet dynamics in shaping the range of future outcomes.

Overall, the scientific evidence points unequivocally toward rising sea levels with potentially severe impacts, while also highlighting a broad envelope of plausible future trajectories. Coastal engineers and planners must therefore prepare for a range of scenarios. Robust analytical approaches, transparent treatment of uncertainties, and careful interpretation of projection data are essential when assessing SLR impacts at regional and local scales.

3 COASTAL RISK ASSESSMENT APPROACHES

Assessing the impacts of climate change on coastal zones typically involves top-down approaches, bottom-up strategies, or an integration of both. Contemporary methodologies increasingly seek to combine large-scale, scenario-based modelling with localized assessments of vulnerability in order to better inform adaptive planning. This section provides a comparative overview of these approaches, examining their respective workflows, strengths, and limitations. Particular emphasis is placed on the critical role of stakeholder engagement and cross-disciplinary collaboration in developing comprehensive and context-sensitive coastal risk assessments.

3.1 Top-Down Scenario-Driven Assessment

Top-down methods, often referred to as impact-driven or prediction-led approaches, begin with broad climate scenarios and progressively translate these projections down to the coastal scale. They typically rely on future greenhouse gas emission scenarios to drive Global Climate Models (GCMs). The outputs of these models (e.g. temperature change, sea-level rise, and variations in storm frequency and intensity) are

subsequently downscaled to regional and local scales using regional climate models or statistical techniques. These downscaled climate variables are then applied to local coastal impact models.

Through this modelling chain, global climate change signals are translated into site-specific hazard scenarios, such as coastal inundation extents, flood frequencies, or shoreline change projections. A key strength of the top-down framework is its capacity to explore multiple plausible futures by evaluating discrete emission pathways (e.g. low, intermediate, and high emissions scenarios). Moreover, this approach ensures consistency with established climate science, as local hazard assessments are directly linked to the best available global climate projections. As a result, top-down assessments have become the dominant approach for long-term coastal hazard analysis and are widely used in planning studies and climate impact assessments spanning several decades to a century.

Despite these advantages, top-down approaches are subject to a cascade of uncertainties at each stage of the modelling process. Uncertainty arises from assumptions about future socio-economic development and emissions trajectories, differences among GCM outputs, variability in sea-level rise projections, the choice of downscaling techniques, and the parameterization of local impact models. These uncertainties tend to accumulate as analyses progress from global to regional and ultimately to local scales, often leading to a wide spread of projected outcomes.

For example, Toimil et al. (2020) demonstrated that projections of beach erosion by 2100 at a given site can differ substantially depending on the selected climate model ensemble or sea-level rise scenario. Figure 2 provides a schematic overview of the top-down modelling sequence, illustrating how global climate projections are successively downscaled through regional models to inform localized impact assessments. At each stage, uncertainties propagate and compound, reflecting the progressive transfer of imprecision from emission scenarios to site-specific risk evaluations.

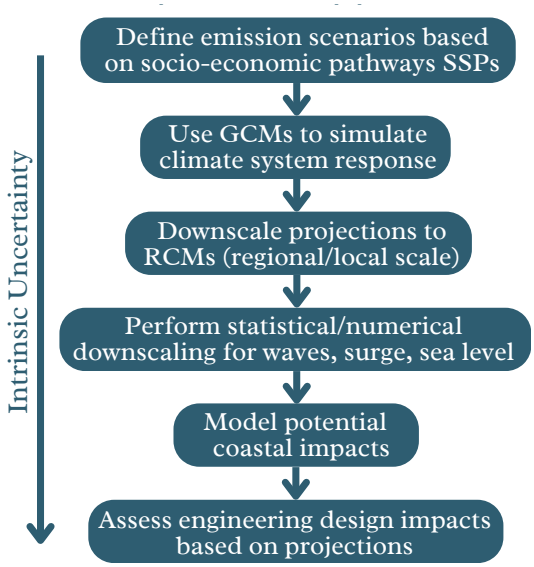

Figure 2. Schematic representation of a top-down coastal risk assessment framework.

Major contributors to this uncertainty include the selected emissions scenario, inter-model variability among global climate models, alternative sea-level rise estimates (e.g. median versus upper-bound projections), downscaling methodologies, and assumptions embedded within coastal impact models, such as erosion formulations and flood threshold definitions. In practical terms, this means that while top-down assessments provide a valuable broad-scale perspective, they may overlook fine-scale features that are critical for local risk management.

In response, researchers have sought to enhance the robustness of top-down coastal risk assessments through improved data sources and modelling techniques. Appelquist (2013), for instance, developed a globally applicable framework for coastal classification and meso-scale hazard assessment to support climate adaptation planning. Lin et al. (2020) combined remote sensing (including UAV surveys), geographic information systems (GIS), and statistical modelling to quantify vulnerability and resilience in coastal communities, demonstrating the added value of high-resolution datasets in top-down analyses. Igigabel et al. (2023) proposed a systemic approach linking sea-level rise projections with meteorological-oceanographic forcing and coastal geomorphology to assess the temporal evolution of hazard profiles. Similarly,

Skinner (2024) introduced a framework that integrates multi-decadal shoreline response models with climate variability and sea-level trends to support strategic coastal infrastructure planning.

While these advances substantially improve top-down methodologies, even the most sophisticated models remain limited in their ability to represent local complexities. Generalized scenarios, even after downscaling, may fail to capture fine-scale variations in topography, land use, exposure, and adaptive capacity that strongly influence real-world risk. For example, coarse models may overlook localized low-lying sections of coastal defenses or densely populated informal settlements—factors that can critically alter flood outcomes. As noted by Di Risio et al. (2017), national-scale vulnerability assessments may mask local hotspots of risk that only detailed, site-specific investigations can reveal.

In summary, top-down approaches provide an essential "big-picture" perspective and ensure scientific coherence across scales. However, to effectively support coastal risk management and adaptation planning, they should be complemented by locally grounded data, knowledge, and participatory processes.

3.2 Bottom-Up Vulnerability Assessment and Climate Stress-Testing

Bottom-up approaches, in contrast to the climate-led nature of top-down methods, take the local system as their starting point, assessing vulnerabilities, stressors, and capacity limits by building the analysis from the coast upward. A bottom-up assessment begins by focusing on current conditions and the specific challenges faced by a given coastal area or community. It involves active engagement with local stakeholders—such as residents, community leaders, engineers, planners, and ecologists—to collect detailed, site-specific information and to understand local concerns, priorities, and values.

This process often includes participatory mapping of low-lying neighbourhoods, critical infrastructure, and sensitive ecosystems to identify assets at risk. Data on local topography and bathymetry are collected, together with historical records of flooding and erosion, as well as indicators of social vulnerability (e.g. population characteristics, mobility constraints, and evacuation capacity). By grounding the assessment in local knowledge and empirical data, bottom-up approaches capture factors that may be overlooked in purely top-down analyses, such as the deteriorating condition of a specific seawall or a community's limited access to evacuation resources. As a result, the outcomes of bottom-up assessments are often more directly relevant and credible to those responsible for implementing adaptation measures, as they reflect lived experience and local realities.

A key analytical tool within bottom-up risk assessment is climate stress testing. This technique evaluates how a coastal system—whether a settlement, infrastructure network, or ecosystem—performs under a wide range of hypothetical stress conditions rather than a limited set of predefined climate projections. Climate stress testing can be understood as a structured sensitivity analysis in which the system is subjected to progressively more severe conditions, such as incrementally higher water levels, stronger storms, or increased rainfall intensity, in order to identify thresholds beyond which system performance becomes unacceptable.

For example, engineers may simulate gradually rising floodwater levels to determine the point at which a town's levee is overtopped, resulting in widespread inundation. Similarly, increasing wave heights may be tested to identify failure thresholds for breakwaters or coastal defenses. By exploring a continuum of possible futures—rather than a small number of discrete scenarios—this approach identifies tipping points and failure conditions that the system cannot tolerate.

Figure 3 outlines the logic of a bottom-up climate stress-testing framework applied to a coastal city. The process begins with defining the local system of concern, including its geographic extent, assets, and stakeholders, followed by the collection of baseline data on coastal flooding, infrastructure, population distribution, and ecosystems.

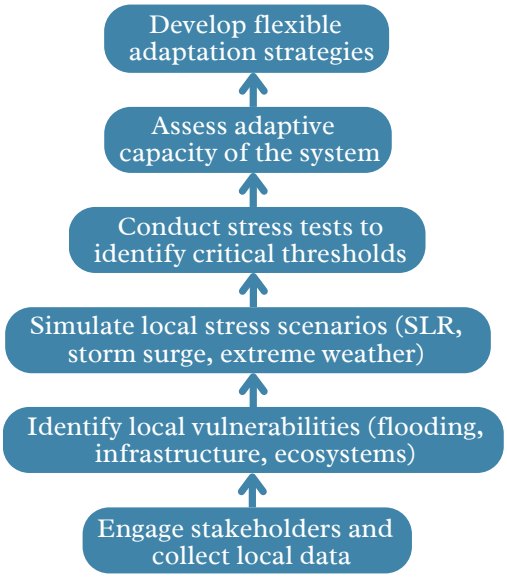

Figure 3. Bottom-up climate stress-testing framework applied to a coastal city.

Stakeholders are engaged early in the process to incorporate local observations of change and community concerns. Subsequently, local hazard models (e.g. flood inundation or shoreline change models) are run under a wide range of conditions combining sea-level rise, storm surge, extreme rainfall, wave action, and other relevant drivers. These conditions are not tied to a single emissions pathway or time horizon but instead span a spectrum of plausible extremes, including compound worst-case combinations (e.g. 0.5 m of sea-level rise combined with a 100-year storm and peak astronomical tide). Through iterative simulations, analysts identify threshold conditions beyond which the system fails or experiences unacceptable impacts.

Threshold metrics may include flood depths at which critical roads become impassable, surge heights that cause coastal defenses to be overtopped or breached, or erosion rates that undermine buildings or infrastructure. Once vulnerability thresholds are identified, the results are used to inform targeted adaptation strategies. In essence, climate stress testing reveals how much change a coastal system can accommodate before existing defenses, practices, or governance arrangements are overwhelmed.

An additional strength of bottom-up approaches is their explicit consideration of non-climatic stressors alongside climate-related drivers. Real-world vulnerability is often exacerbated by factors such as land subsidence, sediment starvation due to river regulation, coastal development that removes natural buffers, or institutional and socioeconomic constraints, including limited emergency response capacity. Bottom-up assessments can integrate these factors directly into stress-testing exercises to reflect the full complexity of local risk.

For example, a coastal city built on reclaimed or former marshland may be subsiding several millimetres per year due to groundwater extraction; a bottom-up analysis would explicitly incorporate this subsidence into future flood scenarios. Similarly, the loss of mangroves or dunes can be accounted for by adjusting wave attenuation or surge exposure in vulnerability assessment.

Bottom-up approaches are inherently interdisciplinary and participatory. By involving local actors throughout the assessment process, they help ensure that adaptation strategies are feasible, socially acceptable, and aligned with community priorities. A particular strength of this approach lies in its capacity to identify practical, context-specific adaptation options. Following stress testing, the analysis often progresses to the evaluation of measures aimed at increasing system resilience by raising identified failure thresholds.

This may involve iterative testing of proposed adaptations. For instance, analysts may examine whether raising a seawall by 0.5 m sufficiently delays overtopping under extreme scenarios, or whether wetland restoration seaward of a dike effectively reduces wave energy during major storms. Through this iterative exploration, bottom-up assessments not only diagnose vulnerabilities but also directly inform the design and prioritization of adaptation measures.

Recent studies illustrate the growing refinement and applicability of bottom-up frameworks. Knighton et al. (2017) developed a vulnerability-based flood risk assessment that integrates physical hydrologic modelling with a peaks-over-threshold statistical approach to account for non-stationarity in extreme events. Padulano et al. (2021) proposed a simplified yet robust method for assessing climate change impacts on urban flooding that avoids reliance on uncertain future

rainfall projections by focusing on critical process thresholds. Guan et al. (2023) introduced a multi-level flood hazard mapping approach for data-scarce cities, demonstrating how bottom-up methods can improve risk estimation even where high-resolution inputs are unavailable. Collectively, these examples show that bottom-up approaches are becoming increasingly accessible and transferable, including in regions with limited data availability.

4 ADAPTATION PLANNING AND STRATEGIES UNDER UNCERTAINTY

Given the complementary strengths of top-down and bottom-up approaches, current best practice increasingly supports their integration within a single, flexible planning framework (Lawrence et al., 2019). In practice, this often takes the form of dynamic adaptive planning, whereby large-scale climate scenarios inform long-term strategic objectives, while local vulnerability assessments guide near-term actions and define trigger points for future adjustments.

One widely adopted method within this paradigm is the adaptation pathways approach, which develops an adaptive roadmap of decisions over time based on how future conditions actually unfold. Rather than committing to a single, fixed solution over a century-long horizon, an adaptation pathways plan outlines a sequence of potential measures and specifies the conditions under which a transition from one measure to the next should occur. For example, a low-lying coastal city may initially enhance drainage systems and construct modest floodwalls. The plan would then define thresholds—such as a mean sea-level rise of X cm or flood events exceeding Y occurrences per year—at which additional interventions, such as higher dikes or storm surge barriers, would be implemented. This approach preserves flexibility and helps avoid both premature overinvestment and delayed action that could lead to unacceptable risk.

The development of adaptation pathways is typically participatory, involving stakeholders in the selection of preferred strategies and acceptable trade-offs.

Communities may prioritise "soft" measures—such as beach nourishment or wetland restoration—in the early stages, postponing more capital-intensive engineering solutions unless they become strictly necessary. By incorporating local values, risk tolerance, and development objectives, pathways can be designed to be both robust and context-sensitive. Interdisciplinary collaboration is essential in this process. Each potential action along a pathway must be evaluated in terms of technical feasibility, economic cost, ecological impact, and social acceptability. Haasnoot et al. (2019) applied this approach across a range of coastal archetypes, illustrating "generic adaptation pathways" for deltas, estuaries, and atoll islands under uncertain sea-level rise conditions. Their results emphasised the need for context-specific strategies, as the effectiveness and timing of adaptation measures are closely linked to local environmental and socioeconomic characteristics. Nevertheless, the pathways framework provides a coherent structure for comparing and coordinating adaptation efforts across diverse settings.

A recent example of integrated planning is the European CoCliCo project (Coastal Climate Core Service), which combines top-down and bottom-up elements to deliver high-resolution coastal risk assessments. CoCliCo develops dynamic coastal flood hazard simulations across Europe under multiple climate scenarios, while integrating detailed exposure data (e.g. population and assets) and downscaled socioeconomic projections. By linking long-term climate projections with local-scale impact models and fostering iterative learning with stakeholders, such hybrid approaches aim to enhance resilience while reducing the risk of maladaptation.

A comprehensive study by Magnan et al. (2023) examined coastal adaptation efforts across 61 case studies worldwide, assessing their level of advancement. Figure 4 presents the resulting global coastal adaptation imprint, evaluated across six key dimensions: risk knowledge, planning, action, capacities, evidence of risk reduction, and long-term strategies. Each dimension is scored on a 0–4 scale, reflecting its contribution to effective local adaptation. Scores are grouped into qualitative categories—No-to-Very Low (0–1), Low-to-Moderate (1–2), Moderate-to-High (2–3), and High-to-Very High (3–4)—providing a clear overview of where adaptation progress is strongest (notably in risk knowledge) and where it remains limited, particularly in long-term strategic planning and the avoidance of maladaptation.

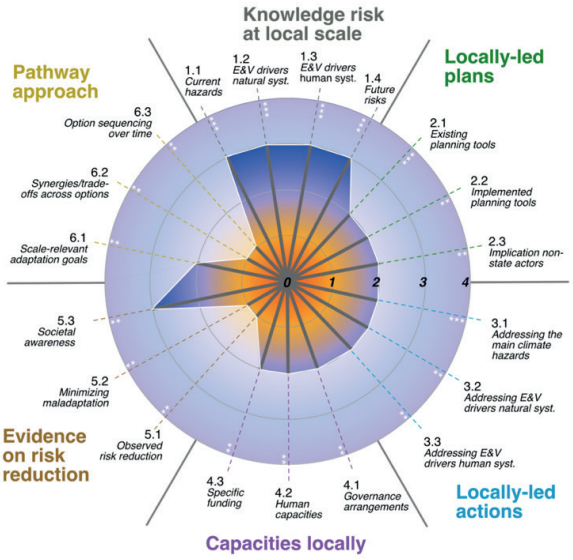

Figure 4. *Global coastal adaptation imprint based on six key dimensions, scored from No-to-Very Low to Very High (source: Magnan et al., 2023).*

In summary, global adaptation responses to coastal climate risks remain modest relative to the scale and pace of projected impacts. Most actions to date have been incremental rather than transformational, despite the likelihood that more profound changes will be required under continued sea-level rise and intensifying climate extremes. Short planning horizons, reactive (rather than anticipatory) decision-making, and sector-based governance structures have constrained the effectiveness of adaptation efforts.

Nevertheless, there remains a critical window of opportunity. By rapidly scaling up investment in coastal resilience, improving coordination between national policy frameworks and local implementation, and embracing innovative solutions—both engineered and nature-based—that extend beyond moderate climate scenarios, coastal societies can shift from ad hoc responses to strategic, long-term adaptation. Ultimately, only proactive and comprehensive planning can enable the most vulnerable coastal regions to avert the most severe consequences of climate change along the world's shores.

CONCLUSIONS

Effective coastal risk management in low-lying areas under climate change requires the integration of both top-down and bottom-up approaches, leveraging their complementary strengths. Top-down methods, grounded in large-scale models and future climate scenarios, provide estimates of the range of potential hazards and support strategic long-term planning. Bottom-up methods, which actively engage local stakeholders, reveal on-the-ground vulnerabilities, site-specific failure thresholds, and community priorities that may be overlooked by purely scenario-driven analyses. This study demonstrates that a blended approach—combining global projections with detailed local assessments—yields a more robust and actionable understanding of coastal risk.

Such integration enables the development of dynamic adaptation pathways that can be phased over time and adjusted as new information becomes available. Rather than relying on one-off interventions, coastal adaptation should be framed as a continuous, iterative process of learning, monitoring, and adjustment.

Although significant uncertainties persist—particularly regarding the magnitude and timing of future sea-level rise—adopting robust and flexible strategies can enhance preparedness across a wide range of plausible futures. These strategies typically involve a diversified portfolio of measures, including engineered defenses (e.g. surge barriers and levees designed with safety margins or upgrade options), nature-based solutions (e.g. mangroves, reefs, and marshes that evolve over time), forward-looking land-use planning to limit development in high-exposure areas, and adaptive policy instruments (such as rolling easements or insurance schemes) that facilitate adjustment as conditions change. No single solution is sufficient; instead, a context-specific combination of measures is required.

In conclusion, the integration of bottom-up and top-down perspectives—supported by iterative, inclusive planning processes—is essential for managing the escalating risks associated with sea-level rise in low-lying coastal regions. Continued refinement and implementation of integrated risk assessment and adaptation strategies will be critical to safeguarding both communities and ecosystems in the face of uncertain, but unequivocally rising, seas.

REFERENCES

Appelquist, L.R. (2013). Generic framework for meso-scale assessment of climate change hazards in coastal environments. Journal of Coastal Conservation, pp.59-74.

Bamber, J.L., Oppenheimer, M., Kopp, R.E., Aspinall, W.P. and Cooke, R.M. (2019). Ice sheet contributions to future sea-level rise from structured expert judgment. Proceedings of the National Academy of Sciences, 116(23), pp.11195-11200.

DeConto, R.M., Pollard, D., Alley, R.B., Velicogna, I., Gasson, E., Gomez, N., Sadai, S., Condron, A., Gilford, D.M., Ashe, E.L. and Kopp, R.E. (2021). The Paris Climate Agreement and future sea-level rise from Antarctica. Nature, 593(7857), pp.83-89.

Di Risio, M., Bruschi, A., Lisi, I., Pesarino, V. and Pasquali, D. (2017). Comparative analysis of coastal flooding vulnerability and hazard assessment at national scale. Journal of Marine Science and Engineering, 5(4), p.51.

Griggs, G., & Reguero, B. G. (2021). Coastal adaptation to climate change and sea-level rise. Water, 13(16), 2151.

Guan, M., Guo, K., Yan, H. and Wright, N. (2023). Bottom-up multilevel flood hazard mapping by integrated inundation modelling in data scarce cities. Journal of Hydrology, 617, p.129114.

Haasnoot, M., Kwakkel, J. H., Walker, W. E., & ter Maat, J. (2013). Dynamic adaptive policy pathways: A method for crafting robust decisions for a deeply uncertain world. Global Environmental Change, 23(2), 485–498.

Hinkel, J., Aerts, J.C., Brown, S., Jiménez, J.A., Lincke, D., Nicholls, R.J., Scussolini, P., Sanchez-Arcilla, A., Vafeidis, A. and Addo, K.A. (2018). The ability of societies to adapt to twenty-first-century sea-level rise. Nature Climate Change, 8(7), 570-578.

IPCC. (2021). Climate Change 2021: The Physical Science Basis. Contribution of Working Group I to the Sixth Assessment Report of the Intergovernmental Panel on Climate Change. Cambridge University Press.

Igigabel, M., Yates, M., Vousdoukas, M. and Diab, Y. (2023). A systemic and comprehensive assessment of coastal hazard changes: method and application to France and its overseas territories. Natural Hazards and Earth System Sciences Discussions, 2023, 1-35.

Knighton, J., Steinschneider, S., & Walter, M. T. (2017). A vulnerability-based, bottom-up assessment of future riverine flood risk using a modified peaks-over-threshold approach and a physically based hydrologic model. Water Resources Research, 53(12), 10043–10064.

Kopp, R.E., Garner, G.G., Hermans, T.H., Jha, S., Kumar, P., Reedy, A., Slangen, A.B., Turilli, M., Edwards, T.L., Gregory, J.M. and Koubbe, G. (2023). The Framework for Assessing Changes to Sea-level (FACTS) v1.0: a platform for characterizing parametric and structural uncertainty in future global, relative, and extreme sea-level change. Geoscientific Model Development, 16(24), 7461-7489.

Lawrence, J., Bell, R., & Stroombergen, A. (2019). A hybrid process to address uncertainty and changing climate risk in coastal areas using dynamic adaptive pathways planning, multi-criteria decision analysis & real options analysis: a New Zealand application. Sustainability, 11(2), 406.

Lin, S.W., Yen, C.F., Chang, C.H., Wang, L.J. and Shih, H.J. (2020). Comprehensive natural environment and landscape signs in coastal settlement hazard assessment: case of east Taiwan between the coastal mountain and the Pacific Ocean. Journal of Marine Science and Engineering, 8(7), 478.

Magnan, A.K., Bell, R., Duvat, V.K., Ford, J.D., Garschagen, M., Haasnoot, M., Lacambra, C., Losada, I.J., Mach, K.J., Noblet, M. and Parthasaranthy, D. (2023). Status of global coastal adaptation. Nature Climate Change, 13(11), 1213-1221.

Padulano, R., Costabile, P., Costanzo, C., Rianna, G., Del Giudice, G. and Mercogliano, P. (2021). Using the present to estimate the future: A simplified approach for the quantification of climate change effects on urban flooding by scenario analysis. Hydrological Processes, 35(12), e14436.

Skinner, W.K. (2024). Coastal Hazard Assessment from Multidecadal Profile Response Incorporating Climate Patterns and Sea-Level Rise. Journal of Coastal Research, 40(3), 511-526.

Toimil, A., Camus, P., Losada, I.J., Le Cozannet, G., Nicholls, R.J., Idier, D. and Maspataud, A. (2020). Climate change-driven coastal erosion modelling in temperate sandy beaches: Methods and uncertainty treatment. Earth-Science Reviews, 202, 103110.

Tomasicchio, G.R., Lusito, L., D'Alessandro, F., Frega, F., Francone, A. and De Bartolo, S. (2018). A direct scaling analysis for the sea level rise. Stochastic Environmental Research and Risk Assessment, 32, 3397-3408.

DOI: https://doi.org/10.53256/COSE_240203

Neural Network-Based Nonlinear Coastal Wave Forecasting Using Hindcast Data and Phase-Resolving Wave Modelling

W. W. Wang[a,*] and H. Bihs[a]
[a]*Civil and Environmental Engineering, Norwegian University of Science and Technology, Trondheim, Norway*

[*]*Corresponding author: Widar Weizhi Wang, widar.w.wang@ntnu.no*

ABSTRACT: As ocean waves approach the shore and propagate over complex coastal topo-bathymetry, the wave field becomes increasingly inhomogeneous and nonlinear. Such nonlinear behaviour poses significant challenges for phase-averaged wave models, particularly in representing wave transformation processes such as diffraction, for which phase-resolving models are often required. With the growing availability of hindcast datasets, data-driven approaches—enabled by recent advances in machine-learning techniques, including neural networks—have increasingly been applied to offshore wave forecasting. In this study, a feed-forward multilayer perceptron (MLP) is employed to establish a nonlinear relationship between offshore and nearshore wave conditions, using phase-resolving wave model outputs as training data. A suite of phase-resolving numerical simulations, conducted under varying offshore wave conditions, is used to generate the training dataset. By combining machine-learning techniques with phase-resolving simulations, the proposed approach yields accurate predictions of wave heights in shoaling and diffraction zones, as well as wave forces acting on the shoal, and demonstrates clear advantages over linear and polynomial regression methods at the test site. Furthermore, the study investigates the coupling of long short-term memory (LSTM)-based offshore wave forecasting with the MLP-based offshore-to-nearshore correlation. The results indicate that this hybrid framework represents a promising pathway towards reliable, site-specific coastal wave forecasting.

KEYWORDS: phase-resolving modelling, numerical simulation, machine learning, coastal wave transformation

1 INTRODUCTION

As ocean waves propagate from deep offshore waters towards coastal regions, they interact with varying seabed topography and irregular coastlines, leading to complex and nonlinear wave transformations such as shoaling, refraction, diffraction, and breaking. These nonlinear processes in coastal waters make the accurate description and prediction of nearshore wave conditions particularly challenging. Well-established offshore wave spectra, such as the JONSWAP spectrum (Hasselmann et al., 1973), often fail to adequately represent coastal wave fields. Attempts to incorporate shallow-water effects into spectral formulations have been made, for example through the TMA spectrum (Hughes, 1984), which modifies the JONSWAP spectrum. However, such formulations are typically limited to constant water-depth scenarios and do not fully account for spatially varying bathymetry.

As coastal blue-economy activities continue to expand—including offshore wind farms, aquaculture, maritime transport, coastal infrastructure, and climate-change adaptation and protection—it has become increasingly important to characterize coastal wave conditions with greater accuracy and detail.

Moving beyond analytical wave descriptions, spectral wave models such as SWAN (Booij et al., 1999) are widely used for offshore and coastal wave prediction. However, within the phase-averaged framework, approximations of nonlinear coastal wave transformations—particularly diffraction—are often inadequate (Holthuijsen et al., 2003). This limitation can lead to the underestimation of wave energy in diffraction-dominated regions and inaccurate representations of coastal wave spectra (Wang et al., 2022). To capture nonlinear wave processes with higher fidelity, phase-resolving wave models are frequently required.

Among the most widely used phase-resolving models are: shallow-water equation (SWE)-based models, such as Boussinesq-type formulations (Madsen et al., 1991; Madsen et al., 1998) and SWE models incorporating quadratic non-hydrostatic pressure corrections (Wang et al., 2020); fully nonlinear potential flow (FNPF) models, including high-order spectral (HOS) models (Ducrozet et al., 2012) and finite-difference-based formulations (Engsig-Karup et al., 2009; Bihs et al., 2020); and three-dimensional non-hydrostatic models (Zijlema et al., 2011; Bihs et al., 2024). Based on a free-surface- and bathymetry-following σ-grid—where the vertical coordinate is normalized between 0 at the seabed and 1 at the free surface—the fully nonlinear potential flow model REEF3D::FNPF (Wang et al., 2022) introduces a novel coastline treatment based on a combined wetting–drying and level-set approach. Together with flexible wave-breaking detection and dissipation algorithms, the model has demonstrated its ability to efficiently and reliably simulate large-scale coastal wave propagation and transformation over strongly varying bathymetry.

Although phase-resolving models can accurately represent coastal wave nonlinearity, they typically require substantial computational resources and simulation time. For certain applications, faster predictions of coastal wave parameters—or even wave-induced loads—are desirable, for example in fairway and harbour operation optimisation or in the development of digital twins for coastal structures. With the growing availability of both measured and numerically simulated datasets, data-driven approaches have emerged as viable alternatives. Recent developments have seen an increasing application of machine-learning (ML) techniques in coastal and ocean engineering. Based on buoy measurements or hindcast datasets, several studies have attempted to predict future wave conditions using ML methods (James et al., 2018; Feng et al., 2022; Minuzzi and Farina, 2023). More recently, Harris (2024) presented a faster-than-real-time, phase-resolving, data-driven framework for wave propagation and wave–structure interaction. However, most existing studies focus on offshore conditions, while wave transformation processes in coastal waters remain less explored.

In this study, a combined numerical modelling and machine-learning approach is proposed to correlate offshore wave conditions with nearshore wave parameters. The phase-resolving model REEF3D::FNPF is used to generate synthetic coastal wave datasets under varying offshore wave inputs. A feed-forward multilayer perceptron (MLP) neural network is then developed to establish a relationship between offshore wave parameters and nearshore wave heights, as well as wave forces acting on a cylindrical structure located in both shoaling and diffraction regions. Although the primary focus is on offshore–coastal correlation, the study also investigates the potential coupling of the MLP framework with a long short-term memory (LSTM) recurrent neural network for offshore wave prediction, offering a promising pathway towards efficient and reliable forecasting of coastal wave conditions and associated wave loads.

2 NUMERICAL MODEL

The phase-resolving numerical wave model employed in this study is the fully nonlinear potential flow model REEF3D::FNPF (Wang et al., 2022). The governing equation is the Laplace equation, given by Eq. (1):

$$\frac{\partial^2 \phi}{\partial x^2} + \frac{\partial^2 \phi}{\partial y^2} + \frac{\partial^2 \phi}{\partial z^2} = 0 \tag{1}$$

The velocity potential ϕ is obtained by solving Eq. (1) subject to fully nonlinear boundary conditions. These include the kinematic and dynamic free-surface boundary conditions, given in Eqs. (2) and (3), respectively, and the bottom boundary condition, given in Eq. (4):

$$\frac{\partial \eta}{\partial t} = -\frac{\partial \eta}{\partial x}\frac{\partial \tilde{\phi}}{\partial x} - \frac{\partial \eta}{\partial y}\frac{\partial \tilde{\phi}}{\partial y} + \tilde{w}\left(1 + \left(\frac{\partial \eta}{\partial x}\right)^2 + \left(\frac{\partial \eta}{\partial y}\right)^2\right) \tag{2}$$

$$\frac{\partial \tilde{\phi}}{\partial t} = -\frac{1}{2}\left(\left(\frac{\partial \tilde{\phi}}{\partial x}\right)^2 + \left(\frac{\partial \tilde{\phi}}{\partial y}\right)^2\right) + \frac{1}{2}\widetilde{w^2}\left(1 + \left(\frac{\partial \eta}{\partial x}\right)^2 + \left(\frac{\partial \eta}{\partial y}\right)^2\right) - g \tag{3}$$

$$\frac{\partial \phi}{\partial z} + \frac{\partial h}{\partial x}\frac{\partial \phi}{\partial x} + \frac{\partial h}{\partial y}\frac{\partial \phi}{\partial y} = 0 \tag{4}$$

In these boundary conditions, η denotes the free-surface elevation, h is the still-water depth, $\tilde{\phi}$and $\tilde{w}$represent the velocity potential and vertical particle velocity evaluated at the free surface, respectively, and g is the gravitational acceleration.

The governing equation and boundary conditions are solved using a finite-difference method on a structured horizontal grid, combined with a σ-coordinate system in the vertical direction, defined as:

$$\sigma = \frac{z+h(x)}{\eta(x,t)+h(x)} \quad (5)$$

The Laplace equation is solved using a conjugate-gradient solver from the **hypre** library (van der Vorst, 1992), combined with a parallelized geometric multigrid preconditioner. Spatial discretization of the governing equations and boundary conditions is performed using a fifth-order Hamilton–Jacobi weighted essentially non-oscillatory (WENO) scheme (Jiang and Shu, 1996), while time integration is carried out using a third-order total variation diminishing (TVD) Runge–Kutta scheme (Shu and Osher, 1988).

Wave generation is achieved through a relaxation-zone method (Larsen and Dancy, 1983). Wetting–drying processes and coastline detection are handled using a level-set-based algorithm, as described by Wang et al. (2022). Depth-induced and steepness-induced wave breaking are detected based on velocity and steepness criteria (Smit et al., 2013), and wave energy dissipation due to breaking is approximated using an artificial viscosity approach (Baquet et al., 2017). The solver is fully parallelized using the Message Passing Interface (MPI) protocol.

An Arbitrary Lagrangian–Eulerian (ALE) method (Pákozdi et al., 2022) is incorporated into the numerical wave model to enable efficient wave-force calculations. In this approach, the motion of fluid particles and the moving computational grid are synchronized, allowing the numerically resolved nonlinear wave kinematics—such as particle velocities and accelerations during wave transformation—to be directly used in the Morison equation for calculating wave loads on cylindrical structures. The formulation for the wave force in the x-direction is given by Eq. (6):

$$F_x = \rho(h+\eta) \left[\int_0^1 C_M a_x A \, d\sigma + \frac{1}{2}\int_0^1 C_D u|u| \, D d\sigma\right] \quad (6)$$

Here, C_M and C_D are the inertia and drag coefficients, respectively; $A$is the cross-sectional area of the structure; $D$is the cylinder diameter; and a_x and u denote the particle acceleration and velocity in the x-direction.

3 MACHINE LEARNING ALGORITHMS

A feedforward multilayer perceptron (MLP) is employed to establish the relationship between offshore wave parameters and nearshore wave characteristics, including wave forces. Simulated significant wave heights and wave-induced forces obtained from the numerical wave model are used as input–output pairs for training the MLP. Prior to training, all simulated data are normalized using a Min–Max scaling procedure to ensure numerical stability and efficient convergence.
The dataset is randomly divided into training and validation subsets using an 80:20 split. The MLP architecture consists of two fully connected hidden layers with 64 and 32 neurons, respectively, followed by an output layer. The rectified linear unit (ReLU) is adopted as the activation function, while the adaptive moment estimation (Adam) algorithm is used for optimization of the network weights and biases. Model performance is evaluated using the mean squared error (MSE) as the loss function.
To enable offshore wave forecasting based on time-series data, a long short-term memory (LSTM) network is also employed. LSTM networks represent an advanced form of recurrent neural networks (RNNs) that are well suited for learning long-term temporal dependencies in sequential datasets. In this study, the time history of significant wave heights from January to November 2024, obtained from the NORA3 hindcast dataset at an offshore location outside the study site, is used to train the LSTM model, which is subsequently applied to predict wave heights for December 2024.
The LSTM architecture consists of two stacked LSTM layers, each with 50 units, followed by a dense output layer. Similar to the MLP configuration, the Adam optimizer, ReLU activation function, and an MSE-based loss function are adopted. The LSTM implementation is based on the open-source framework developed by the Norwegian Meteorological Institute (https://github.com/MET-OM/metocean-ml).

The interconnections and overall workflow between the numerical wave model and the machine learning components are summarized in Fig. 1.

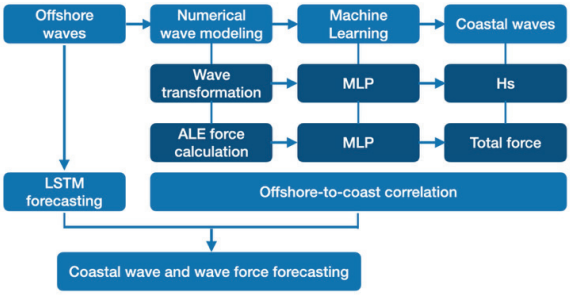

Figure 1. Workflow of the coupled numerical wave model and machine learning framework for coastal wave and wave-force prediction.

4 CASE DESCRIPTION

The study site is located in southern Norway, near the city of Kristiansand. The area of interest comprises the surrounding waters near the island of Store Lyngholmen, which is centred in Fig. 2. The dominant incident waves propagate from the southern boundary of the domain. A navigation tower is planned to be constructed on a shoal south of Store Lyngholmen, indicated as location G1. An anchorage area is situated on the lee side of the island and is denoted as location G2.

The phase-resolving numerical wave tank (NWT) reproduces the bathymetry of the study domain, as shown in Fig. 2. The blue box in Fig. 2 represents the relaxation zone used for wave generation, while the three orange boxes correspond to relaxation zones functioning as numerical beaches to attenuate undesired wave reflections at the domain boundaries.

The imposed irregular waves follow a JONSWAP spectrum with a constant peak period of $T_p = 12$s and a varying significant wave height H_s, ranging from 0.5 m to 10.4 m in increments of 0.1 m. This configuration results in a total of 100 numerical simulations representing different offshore wave conditions. The simulated significant wave heights at locations G1 and G2 are used to train an MLP model for wave height prediction. In addition, the simulated maximum total wave force at location G1 is employed to train a separate MLP model for wave force prediction.

For the idealised cylindrical navigation tower at G1, a diameter of 3 m is assumed. The inertia and drag coefficients used in the force calculations are set to 1.5 and 0.9, respectively.

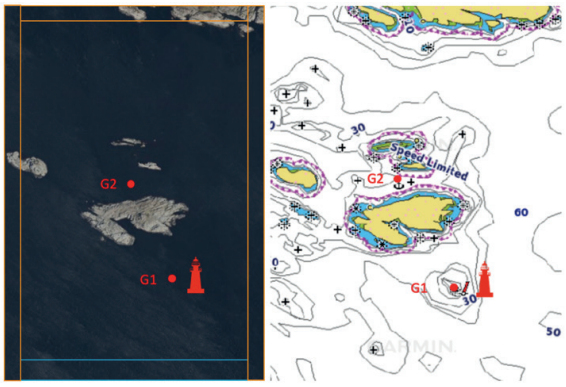

Figure 2. Illustration of the study site, including a satellite image and a bathymetric map. Locations of interest are marked as G1 and G2. G1 is located on a shoal where a navigation tower is planned, while G2 is situated at an anchorage on the lee side of Store Lyngholmen. The blue box indicates the wave generation zone, and the orange boxes represent numerical beach zones.

5 RESULTS AND DISCUSSIONS

Twenty percent of the 100 numerical simulations were used to validate the MLP-based predictions. The MLP-predicted significant wave heights at location G1 (shoaling region), represented by red crosses, are compared with the simulated values (blue dots) for the 20 validation cases in Fig. 3. The x-axis represents the offshore input significant wave height H_s used in the numerical simulations, while the y-axis shows the corresponding simulated and predicted H_s values at G1.

The results indicate that the MLP-predicted significant wave heights closely match those obtained from the phase-resolving simulations across the full range of offshore input wave heights. The machine learning model also reproduces the overall variation trend with high fidelity. In contrast, the linear regression model (cyan dotted line in Fig. 3) fails to accurately predict both the magnitude of H_s and its nonlinear trend. The polynomial regression model (purple dotted curve in Fig. 3), however, provides a comparatively good approximation of the significant wave heights.

Quantitatively, the mean squared error (MSE) of the MLP predictions for the 20 validation cases is 0.141 m, which is higher than that of the polynomial regression (0.054 m). As expected, the linear regression yields the largest error, with an MSE of 0.424 m.

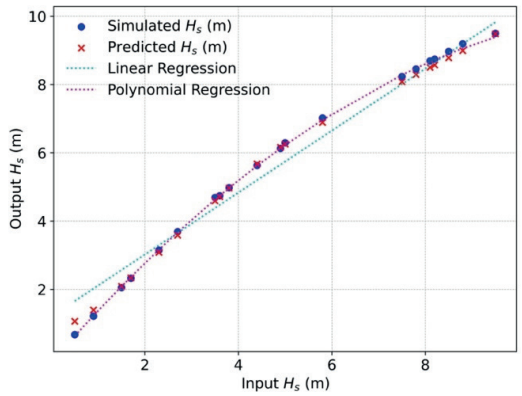

Figure 3. Comparison of simulated significant wave heights at G1 (shoaling region) with predictions obtained using MLP, linear regression, and polynomial regression.

A similar validation exercise was conducted for the diffracted wave field at location G2, as shown in Fig. 4. The observations are consistent with those for the shoaling region. Both the MLP and polynomial regression models accurately predict the magnitude and trend of the diffracted waves, whereas the linear regression again fails to capture the underlying behavior of the wave field. In this case, the MSE values are 0.027 m for the MLP, 0.068 m for linear regression, and 0.013 m for polynomial regression.

More pronounced differences among the prediction methods are observed for the maximum total wave forces acting on the cylindrical structure at G1. As shown in Fig. 5, the total wave force exhibits a stronger nonlinear relationship with offshore wave height than the significant wave height. Initially, the force increases rapidly with increasing offshore H_s; beyond approximately 4 m offshore H_s, the growth rate decreases markedly. This nonlinear behavior can be attributed to premature wave breaking in front of the shoal as offshore wave heights increase.

In this regime, the MLP demonstrates a clear advantage in capturing the complex transition in the physical wave transformation process. The MLP-predicted maximum total wave forces agree well with both the simulated magnitudes and the observed trend. Neither the linear regression nor the polynomial regression adequately reproduces this nonlinear behavior. The MLP approach yields the lowest MSE of 95.89 kN, compared to 342 kN for linear regression and 161 kN for polynomial regression.

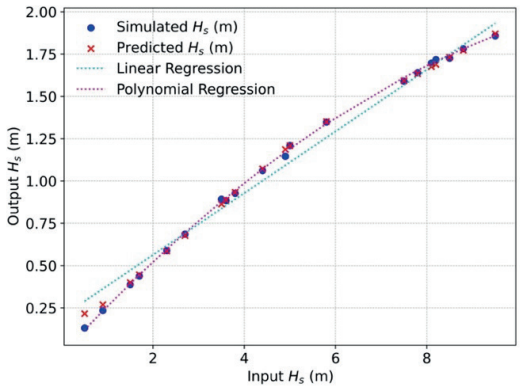

Figure 4. Comparison of simulated significant wave heights at G2 (diffraction region) with predictions obtained using MLP, linear regression, and polynomial regression.

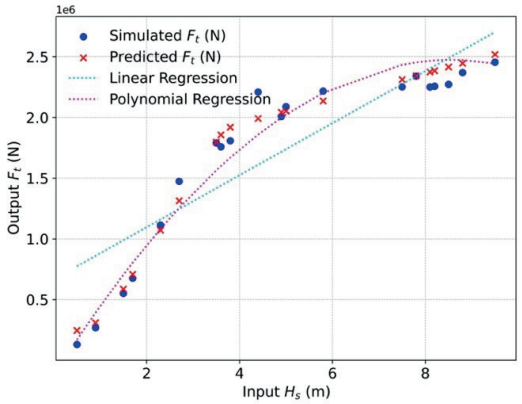

Figure 5. Comparison of simulated maximum total wave forces at G1 (shoaling region) with predictions obtained using MLP, linear regression, and polynomial regression.

Overall, the MLP algorithm provides consistent and reliable predictions for shoaling waves, diffracted waves, and maximum total wave forces. This demonstrates its capability for rapid prediction of coastal wave parameters and wave-induced forces based solely on offshore wave inputs at the study site.

To enable coastal wave forecasting, an LSTM-based model was employed to predict offshore wave conditions using existing hindcast data. Hourly significant wave height time series from an offshore location south of Store Lyngholmen (longitude 7.9293369° E, latitude 58.0167552° N) between January and November 2024 were used to train the LSTM model, which was then applied to predict the wave height time series for December 2024. The predicted H_s values are validated against the corresponding hindcast data for December 2024, as shown in Fig. 6.

The LSTM model successfully captures the general temporal evolution of the significant wave height throughout December. The predicted significant wave height at 23:00 on 31 December 2024 is 3.76 m.

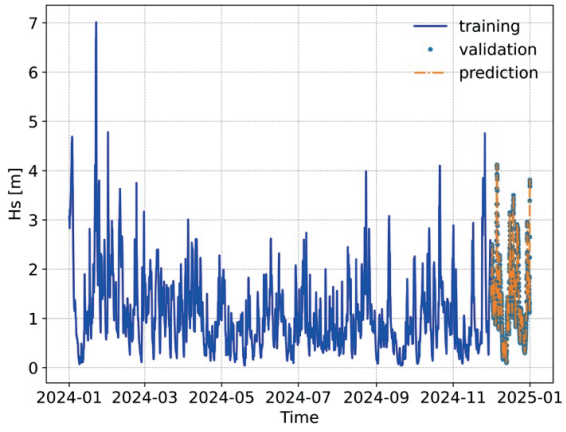

Figure 6. LSTM-based prediction of the significant wave height time series for December 2024 (dash–dotted orange line), validated against hindcast data for December (blue dots), using training data from January to November 2024 (solid blue line).

A new phase-resolving simulation was subsequently performed using the predicted offshore significant wave height of 3.76 m as input. The simulated free surface elevation within the numerical wave tank is shown in Fig. 7. Pronounced wave shoaling is observed, while diffracted waves propagate around both the western and eastern sides of Store Lyngholmen and converge in the lee of the island at the anchorage location.

The MLP-predicted significant wave heights at G1 and G2 are 4.954 m and 0.922 m, respectively. The corresponding simulated values are 4.939 m and 0.9378 m, yielding percentage errors of only 0.3% and 1.7%. Since the offshore input wave height lies within the range of the training data, this strong agreement is expected. However, the predicted maximum total wave force is 19,001 kN, which is approximately 10% lower than the simulated value. As the input wave height is close to the wave-breaking transition regime, the wave kinematics become more irregular and strongly nonlinear, making accurate force prediction more challenging in this range.

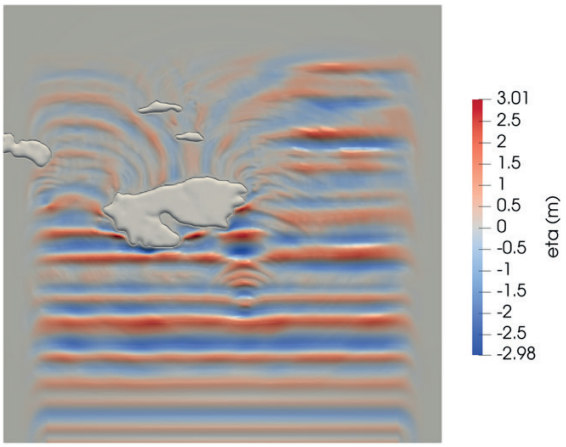

Figure 7. Free surface elevation from the phase-resolving simulation using the predicted offshore significant wave height of 3.76 m on 31 December 2024.

CONCLUSIONS

This study presents a case study demonstrating a hybrid framework that integrates a phase-resolving numerical wave model, hindcast data, and machine-learning techniques. A phase-resolving numerical wave tank (NWT) was used to generate training data for a multi-layer perceptron (MLP), enabling the establishment of a robust correlation between offshore and coastal wave conditions that captures the nonlinear nature of coastal wave transformation. Hindcast data were further employed to train a long short-term memory (LSTM) model for short-term offshore sea-state prediction. When combined, these models provide a computationally efficient approach for rapid forecasting of coastal wave conditions.

The coupled NWT–MLP framework successfully reproduces the key physical processes governing wave shoaling, diffraction, and wave-induced forces acting on a cylindrical structure. Its advantages are particularly evident in the prediction of wave forces, where it clearly outperforms simpler surrogate models such as linear and polynomial regressions. Although further investigation is required—particularly regarding the sensitivity to machine-learning architectures, training data volume, and input parameter selection—the results demonstrate the feasibility and practical potential of the proposed approach for coastal engineering applications, including real-time forecasting and decision support.

ACKNOWLEDGEMENTS

The authors acknowledge funding from the European Union (ERC, PARTRES, grant agreement No. 101045646). The views and opinions expressed in this work are those of the authors only and do not necessarily reflect those of the European Union or the European Research Council Executive Agency. Neither the European Union nor the granting authority can be held responsible for them. The numerical simulations were performed on the Betzy supercomputer, provided by Sigma2 – the National Infrastructure for High-Performance Computing and Data Storage in Norway.

REFERENCES

Baquet, A., Kim, J., Huang, Z.J. (2017) Numerical modeling using CFD and potential wave theory for three-hour nonlinear irregular wave simulations. In: International Conference on Offshore Mechanics and Arctic Engineering. Vol. 1: Offshore Technology: V001T01A002

Bihs, H., Wang, W., Pákozdi, C., Kamath, A. (2020) REEF3D::FNPF—A Flexible Fully Nonlinear Potential Flow Solver, Journal of Offshore Mechanics and Arctic Engineering 142 (4): 041902.

Bihs, H., Ehlers R., Wang W. (2024) A Shock-absorbing non-hydrostatic Navier-Stokes solver on σ-grids for wave modeling over irregular topography, 43rd International Conference on Ocean, Offshore & Arctic Engineering, Singapore, Volume 6: Polar and Arctic Sciences and Technology; CFD, FSI, and AI: V006T08A016

Booij, N., Ris, R. C., Holthuijsen, L. H. (1999) A third-generation wave model for coastal regions: 1. Model description and validation, Journal of Geophysical Research: Oceans 104 (C4): 7649–7666.

Ducrozet, G., Bonnefoy, F. e. l., Le Touzé, D., Ferrant, P. (2012) A modified High-Order Spectral method for wavemaker modeling in a numerical wave tank, European Journal of Mechanics - B/Fluids 34: 19-34

Engsig-Karup, A., Bingham, H., Lindberg, O. (2009) An efficient flexible-order model for 3D nonlinear water waves, Journal of Computational Physics 228: 2100–2118.

Feng, Z., Hu, P., Li, S. and Mo, D. (2022) Prediction of significant wave height in offshore China based on the machine learning method. Journal of Marine Science and Engineering 10 (6): 836

Haakenstad, H., Breivik, Ø., Furevik, B. R., Reistad, M., Bohlinger, P., Aarnes, O. J. (2021) NORA3: A nonhydrostatic high-resolution hindcast of the North Sea, the Norwegian Sea, and the Barents Sea, Journal of Applied Meteorology and Climatology 60 (10): 1443–1464

Harris, J, C. (2024) Faster than real-time, phase-resolving, data-driven model of wave propagation and wave–structure interaction. Applied Ocean Research 154: 104291

Hasselmann, K., Barnett, T., Bouws, E., Carlson, H., Cartwright, D.. Enke, K., Ewing, J., Gienapp, H., Hasselmann, D., Kruseman, P., Meerburg, A., Müller, P., Olbers, D., Richter, K., Sell, W., Walden, H. (1973) Measurements of wind-wave growth and swell decay during the Joint North Sea Wave Project (JONSWAP), Ergänzungsheft zur Deutschen Hydrographischen Zeitschrift, Reihe A 12 (8): 1–95.

Holthuijsen, L., Herman, A., Booij, N. (2003) Phase-decoupled refraction–diffraction for spectral wave models, Coastal Engineering 49 (4): 291–305.

Hughes, S. A. (1984) The TMA shallow-water spectrum description and applications, Coastal Engineering Research Center, Vicksburg, Mississippi, U.S.A. Tech. Rep.: CERC-84-7

James, S. C., Zhang, Y. and O'Donncha, F. (2018) A machine learning framework to forecast wave conditions. Coastal Engineering 137: p. 1–10.

Jeschke, A., Pedersen, G. K., Vater, S., Behrens, J. (2017) Depth-averaged non-hydrostatic extension for shallow water equations with quadratic vertical pressure profile: equivalence to Boussinesq-type equations, International Journal for Numerical Methods in Fluids 84 (10): 569–583

Jiang, G. S., Shu, C. W., (1996) Efficient implementation of weighted ENO schemes. J. Comput. Phys. 126: 202–228.

Larsen, J., Dancy, H., (1983) Open boundaries in short wave simulations — A new approach. Coast. Eng. 7 (3): 285–297.

Madsen, P. A., Murray, R., Sørensen, O. R. (1991) A new form of the Boussinesq equations with improved linear dispersion characteristics, Coastal Engineering 15: 371–388.

Madsen, P. A., Schäffer, H. A. (1998) Higher-order Boussinesq-type equations for surface gravity waves: derivation and analysis, Philosophical Transactions of the Royal Society of London. Series A: Mathematical, Physical and Engineering Sciences 356 (1749): 3123–3181.

Minuzzi, F. C., Farina, L. (2023) A deep learning approach to predict significant wave height using long short-term memory. Ocean Modelling 181: 102151

Pákozdi, C., Kamath, A., Wang, W. and Bihs, H. (2022) Application of Arbitrary Lagrangian–Eulerian strips with fully nonlinear wave kinematics for force estimation. Marine Structures 83: 103190.

Shu, C. W., Osher, S., (1988) Efficient implementation of essentially non-oscillatory shock capturing schemes. J. Comput. Phys. 77: 439–471.

Smit, P., Zijlema, M., Stelling, G. (2013) Depth-induced wave breaking in a nonhydrostatic, near-shore wave model. Coast. Eng. 76: 1–16.

Wang, W., Pákozdi, C., Kamath, A., Fouques, S. and Bihs, H. (2022) A flexible fully nonlinear potential flow model for wave propagation over the complex topography of the Norwegian coast. Applied Ocean Research 122: 103103.

van der Vorst, H. (1992) BiCGStab: a fast and smoothly converging variant of Bi-CG for the solution of nonsymmetric linear systems. SIAM J. Sci. Comput. 13: 631–644.

Wang, W., Martin, T., Kamath, A., Bihs, H. (2020) An Improved Depth-Averaged Non-Hydrostatic Shallow Water Model with Quadratic Pressure Approximation, International Journal for Numerical Methods in Fluids 92: 803–824.

Zijlema, M., Stelling, G., Smit, P. (2011) SWASH: An operational public domain code for simulating wave fields and rapidly varied flows in coastal waters, Coastal Engineering 58 (10): 992–1012.

DOI: https://doi.org/10.53256/COSE_240104

Does Tide–Surge Interaction Occur along the Croatian Coast of the Adriatic Sea?

M. M. Gržić[a,*], N. Ožanić[a] and N. Krvavica[a]
[a]*Faculty of Civil Engineering, University of Rijeka, Radmile Matejčić 3, 51000, Rijeka, Croatia*

[*]*Corresponding author: Marta Marija Gržić, e-mail: mmgrzic@gradri.uniri.hr*

ABSTRACT: Understanding the interaction between storm surges and tidal dynamics is essential for accurately assessing coastal flood risk, particularly in microtidal environments such as the Adriatic Sea. This study evaluates tide–surge interaction (TSI) in three regions of the Adriatic Sea—the northern, middle, and southern Adriatic—using three statistical approaches. The applied methods include: (i) distributing extreme storm surges across tidal ranges, (ii) distributing extreme storm surges relative to high tides, and (iii) assessing the correlation between storm surges and high tides. None of the investigated locations exhibited consistent evidence of tide–surge interaction across all applied methods. Consequently, the results indicate that significant TSI does not occur along the Croatian Adriatic coast, suggesting that storm surges and tidal processes act largely independently in this region.

KEYWORDS: Tide-surge interaction (TSI), Adriatic Sea, Microtidal environment, Extreme sea levels

1 INTRODUCTION

High river discharges, heavy precipitation, extreme storm surges, and severe sea states are key flood drivers that render densely populated coastal areas particularly vulnerable to flooding (Green et al., 2024). While storm surges are primarily driven by atmospheric forcing (Pugh & Woodworth, 2014), their impacts are significantly amplified when they coincide with high tide, resulting in extreme water levels that can threaten coastal infrastructure, communities, and ecosystems. Understanding the interaction between storm surges and tidal dynamics is therefore crucial for accurately assessing coastal flood risk, especially in shallow environments where relatively small changes in water level can have substantial consequences. For this reason, increasing attention has been given to tide–surge interaction (TSI) (Williams et al., 2016). The dominant mechanism underlying TSI involves mutual phase modulation between tides and storm surges (Horsburgh & Wilson, 2007). This interaction is inherently nonlinear and can significantly influence coastal water levels during storm events. Accurately capturing these dynamics is essential for reliable coastal flood forecasting and for the development of effective coastal protection and adaptation strategies.

Numerical modelling of TSI typically involves the combined simulation of tides and storm surges, followed by comparison with scenarios in which tides and surges are modelled separately (Idier et al., 2012). This approach is commonly used to assess the influence of TSI on extreme water levels. In several regions, including the English Channel (Idier et al., 2012), the Bay of Bengal (Antony et al., 2020), the South China Sea (Zhang et al., 2017), the Aveiro Lagoon in Portugal (Pinheiro et al., 2020), and the coast of Taiwan (Liu et al., 2016), the influence of TSI on water levels has been shown to range from a few centimetres to more than one metre. Importantly, the interaction does not always result in higher peak water levels; in some cases, TSI can reduce extreme levels (Antony et al., 2020).

In addition to numerical modelling, several statistical methods have been developed to detect and quantify TSI, including those proposed by Dixon and Tawn (1994), Haigh et al. (2010), Williams et al. (2016), and Arns et al. (2020). The approach of Dixon and Tawn (1994) compares the distribution of all tidal values with the distribution of tides associated with the top 1% of storm surge events using a chi-squared test. The underlying assumption is that, in the absence of statistically significant differences between the two distributions, no significant TSI exists. Conversely, significant distributional differences indicate interaction between tidal and surge

components. Haigh et al. (2010) similarly assessed the distribution of the highest 1% of storm surges relative to tidal phase, where a uniform distribution would be expected in the absence of TSI. Williams et al. (2016) examined the dependence between high tides and skew surges by applying the Kendall rank correlation coefficient and the Anderson–Darling test to compare the distribution of all high tides with those associated with the top 1% of skew surges. Arns et al. (2020) further investigated whether non-tidal residuals depend on astronomical tides during extreme sea-level events, providing a statistical framework for quantifying TSI under conditions most relevant to flood risk assessment.(Arns et al., 2020).

These statistical methods reflect the evolution of TSI research over time. Early studies primarily focused on detecting the presence of TSI (Dixon & Tawn, 1994; Haigh et al., 2010), whereas more recent work has aimed at quantifying its magnitude and relevance for risk assessment (Williams et al., 2016; Arns et al., 2020). While the approach of Dixon and Tawn (1994) is effective for identifying the existence of interaction, it does not allow quantification of its strength. Haigh et al. (2010) highlighted the role of tidal phase, demonstrating that storm surges tend to occur more frequently during specific phases of the tidal cycle. Williams et al. (2016) introduced a more formal dependence framework, combining correlation and goodness-of-fit tests. Arns et al. (2020) advanced this further by quantifying the dependence of non-tidal residuals on tides during extreme events, offering the most risk-relevant assessment, albeit with greater methodological complexity.

TSI has been extensively studied in the North Sea, where strong interactions significantly influence extreme sea levels (Dixon & Tawn, 1994; Horsburgh & Wilson, 2007). In the English Channel, Haigh et al. (2010) found significant TSI at eight out of nine tide gauge stations, with interaction strength increasing eastwards. These findings highlight the importance of accounting for TSI in extreme sea-level and flood risk assessments.

To date, however, no studies have specifically investigated TSI along the Croatian coast of the Adriatic Sea. Given the region's complex coastal morphology, including numerous shallow areas such as bays and estuaries, there is a clear need to assess the potential effects of TSI. Statistical dependence between tides and storm surges may significantly increase—or, in some cases, decrease—coastal flood hazard and risk. Incorporating TSI into flood hazard and risk assessments is therefore essential to improve the accuracy of hazard predictions and to support informed coastal management strategies.

The aim of this study is to investigate the dependence between tides and storm surges in three regions of the Adriatic Sea—the northern, middle, and southern Adriatic—using three different statistical methods to assess the presence and significance of TSI.

The paper is structured as follows. Section 2 describes the study area and its main characteristics, as well as the observational data used. Section 3 outlines the methodology, with Subsection 3.1 addressing data preprocessing and Subsections 3.2–3.4 detailing the applied TSI analyses. Section 4 presents the results (Subsections 4.1–4.3) and discusses the findings (Subsection 4.4). Finally, Section 5 summarises the main conclusions of the study.

2 STUDY AREA AND DATA

The Adriatic Sea is a semi-enclosed basin of the Mediterranean Sea, resembling a narrow channel approximately 800 km long and 200 km wide. It is commonly divided into three main regions: the shallow northern Adriatic, the deeper middle Adriatic, and the deep southern Adriatic (Šepić et al., 2022). Extreme sea levels in the Adriatic are influenced by a combination of processes acting across multiple temporal and spatial scales, with tides, storm surges, and seiches being the dominant contributors (Šepić et al., 2022).

Tides in the Adriatic Sea exhibit both diurnal and semidiurnal characteristics, with tidal ranges increasing from approximately 30 cm in the southern Adriatic to up to 1.2 m in the northern part of the basin (Vilibić et al., 2017; Medvedev et al., 2020). Adriatic tidal dynamics are strongly influenced by the amplification of tidal waves as they propagate from south to north due to the progressive narrowing and shallowing of the basin (Janeković & Kuzmić, 2005).

In a microtidal environment such as the Adriatic Sea, tidal signals are generally weaker than storm surge signals (Međugorac et al., 2016, 2018; Krvavica et al., 2024). Consequently, storm surges represent a key driver of extreme sea-level events in this region. A storm surge is the sea-level response to low-pressure systems, typically accompanied by strong south-easterly Sirocco winds. These winds push seawater towards the northern Adriatic, resulting in the highest surge amplitudes in that region, which can reach up to 1.5 m (Međugorac et al., 2016; Ferrarin et al., 2022). Storm surges, whether occurring independently or in combination with high tides and seiches, significantly contribute to extreme sea levels and coastal flooding in the northern Adriatic, with Venice being among the most

affected locations (Cavaleri et al., 2019; Ferrarin et al., 2022).
The fundamental Adriatic seiche, with a period of approximately 21.2 h (Cerovečki et al., 1997), reach amplitudes exceeding 0.5 m in the northern Adriatic. This oscillation can further amplify sea levels and increase the risk of coastal flooding, particularly in areas with complex coastal morphology, such as along the Croatian coastline (Vilibić et al., 2017; Šepić et al., 2022).
For this study, three locations along the Croatian Adriatic coast were selected to represent the northern Adriatic (Bakar station), middle Adriatic (Prosika station), and southern Adriatic (Ušće station). Figure 1 shows the locations of the selected stations (orange triangles) along the Croatian coast.

Figure 1. Locations of the analysed tide gauge stations along the Croatian Adriatic coast (orange triangles): northern Adriatic (Bakar), middle Adriatic (Prosika), and southern Adriatic (Ušće).

For the northern Adriatic station (Bakar), observational data were obtained from the Bakar tide gauge (Međugorac et al., 2022, 2025). This dataset spans 70 years (1950–2020) with an hourly temporal resolution. For the middle and southern Adriatic stations (Prosika and Ušće), observational data were provided by Croatian Waters and the Croatian Meteorological and Hydrological Service. The hourly tide gauge record for Prosika covers 38 years (1986–2023), while the dataset for Ušće spans 47 years (1977–2023).

3 METHODOLOGY

To investigate whether extreme storm surges coincide with high tides in the eastern Adriatic Sea, the first step was to preprocess the sea-level data in order to extract the tidal and non-tidal residual components, as well as the skew surge.
Three statistical methods were applied to investigate different aspects of the tide–surge interaction (TSI) and to determine whether a statistically significant interaction exists (Dixon & Tawn, 1994; Haigh et al., 2010; Williams et al., 2016).
The null hypothesis underlying all three methods is that storm surges (or skew surges) occur randomly with respect to the tidal phase. Accordingly, these methods assume that any storm surge or skew surge can coincide with any tidal level in the absence of interaction.

3.1 Data preprocessing

The first step in data preprocessing involved separating the hourly total sea-level observations into tidal and non-tidal components. A stationary harmonic analysis was performed using the U-Tide toolbox (Codiga, 2011) on sea-level records from all three stations. The analysis incorporated 62 tidal constituents with frequencies greater than 0.03 cycles per hour (cph). The non-tidal residuals were obtained by subtracting the harmonic tidal predictions from the observed sea-level time series. The skew surge was calculated as the difference between the maximum observed sea level and the predicted high tide within each tidal cycle, regardless of the exact timing of the surge peak relative to the tidal maximum (Haigh et al., 2016).

3.2 Distribution of extreme storm surges across tidal ranges

The first method used to assess tide–surge interaction (TSI), originally proposed by Dixon and Tawn (1994), involves extracting the highest 1% of storm surges and grouping them into tidal bins according to the tidal level at the time each extreme storm surge occurs. The tidal range is divided into five equally spaced bins between low and high astronomical tide (Costa et al., 2023).
If storm surges and tides are independent processes, the distribution of tidal levels associated with extreme storm surges should be identical to the overall distribution of the tidal range. To assess whether the two distributions differ, the chi-squared test (χ^2) is applied. The null hypothesis assumes that both distributions are the same, indicating no interaction between tides and storm surges. At the 95% significance level and with four degrees of freedom (one less than the number of bins), the critical value (χ^2_{crit}) is 9.49. If the calcualted χ^2 value is below χ^2_{crit}, the null hypothesis is not rejected, indicating no statistically significant TSI. Conversely, a χ^2

value greater than 9.49 suggests a statistically significant tide–surge interaction.

3.3 Distribution of storm surges relative to high tide

The second method, adapted from Dixon and Tawn (1994) by Haigh et al. (2010), evaluates the distribution of extreme storm surges relative to the timing of high tide. Storm surges exceeding the 99th percentile are extracted, and the corresponding high tides are identified.
Each extracted storm surge is classified into an hourly bin within a ±6-hour window centred on high tide. Under the null hypothesis of no TSI, the resulting distribution should be uniform, meaning that extreme storm surges are equally likely to occur at any time between −6 h and +6 h relative to high tide.
To test whether the binned storm surge distribution is uniform, the chi-squared test (χ^2) with 12 degrees of freedom is applied at the 95% significance level. χ^2 values below the critical value (χ^2_{crit}) of 21.03 indicate no significant TSI, whereas values exceeding this threshold suggest a statistically significant dependence between storm surges and tidal phase.

3.4 Correlation between skew surges and high tides

While the two previous methods focus on the relationship between extreme storm surges and tides, this method examines the dependence between skew surges and predicted high tides (Williams et al., 2016). An advantage of using skew surge rather than storm surge is that it avoids complications related to tidal timing, as skew surge yields a single value per tidal cycle (Santamaria-Aguilar & Vafeidis, 2018).
Potential storm surge peaks and their times of occurrence, along with high tides, are extracted from the observed sea-level data using an 18-hour moving window. For each high tide, the nearest storm surge peak occurring within ±6 hours is selected to compute the skew surge.
Following Williams et al. (2016), the highest 1% of skew surges are extracted to assess the dependence between extreme skew surges and high tides. The Kendall rank correlation coefficient (τ) is used as the dependence metric. Kendall's τ is a non-parametric measure of monotonic association that is robust to outliers and capable of capturing nonlinear relationships based on data ranks (Li et al., 2012).
If skew surges and high tides are independent, the distribution of high tides associated with the highest 1% of skew surges should be statistically indistinguishable from the distribution of all high tides (Williams et al., 2016). This hypothesis is tested using the Anderson–Darling goodness-of-fit test, with the null hypothesis stating that both samples originate from the same underlying distribution.

4 RESULTS AND DISCUSSION

For all three locations along the Croatian coast of the Adriatic Sea (Fig. 1), tide–surge interaction (TSI) analyses were performed using the three methods described in the previous section. The results are presented separately for each station and subsequently discussed.

4.1 Distribution of extreme storm surges across tidal ranges

4.1.1 Northern Adriatic station (Bakar)

Figure 2 presents histograms of all tidal levels (black) and of tidal levels associated with the extracted extreme storm surge peaks (red dashed) for the Bakar station.
In the central bins (approximately −0.1 to 0.2 m), both distributions exhibit the highest probability densities, indicating that these tidal levels are the most frequent in both datasets. The distribution of all tidal levels shows slightly higher probability densities than the distribution corresponding to storm surge peaks, suggesting that average tidal levels are common in both datasets, but even more prevalent in the overall tidal record.
In contrast, in the outer bins, tidal levels associated with storm surge peaks display higher probability densities, indicating that very low or very high tidal levels more frequently coincide with extreme storm surge events. This comparison illustrates whether tidal levels during storm surge peaks are randomly distributed across the tidal cycle or preferentially occur at specific tidal phases.

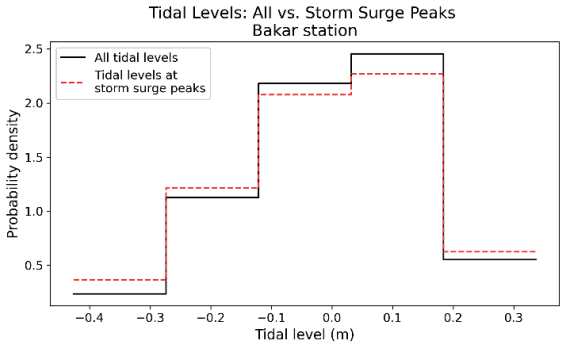

Figure 2. Histograms of tidal levels at the Bakar station for all tidal levels (black) and for tidal levels corresponding to the extracted highest 1% of storm surges (red dashed).

The difference in probability density between the distribution of tidal levels during storm surge

peaks and the expected distribution based on all tidal levels at the Bakar station is shown in Fig. 3. Distinct deviation peaks around −0.3 m and 0.25 m indicate that tidal levels during storm surge peaks occur more frequently than would be expected from the general tidal distribution. The oscillatory nature of the deviation suggests that storm surge peaks are more often associated with both lower-than-average and higher-than-average tidal levels, while being less likely to occur when the tide is near its mean value.

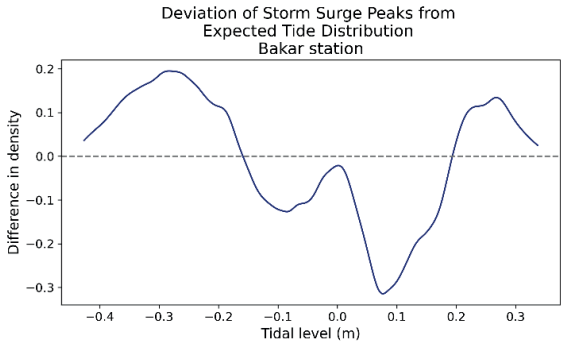

Figure 3. Deviation of the highest 1% of storm surges from the expected tidal distribution at the Bakar station.

For the Bakar station, the chi-squared test yields a χ^2 value of 100.41 at the 95% significance level. As this value greatly exceeds the critical value χ^2_{crit}, the null hypothesis is rejected, indicating a statistically significant difference between the distributions and confirming a strong presence of tide–surge interaction.

4.1.2 Middle Adriatic station (Prosika)

Histograms for the Prosika station indicate that the highest probability densities for both datasets occur within the two central tidal ranges, with a slight shift toward lower tidal levels (Fig. 4). Although the overall shapes of the two distributions are similar, notable differences are observed across most tidal ranges, particularly in the second and third bins. These differences suggest the potential presence of tide–surge interaction (TSI).

The deviations for the Prosika station are shown in Fig. 5. A pronounced positive deviation peak is observed around −0.1 m, indicating that storm surge peaks are considerably more likely to occur at this lower tidal level. This pattern suggests a preference for storm surge peaks to coincide with slightly lower-than-average tidal conditions, rather than with mean or extreme tides.

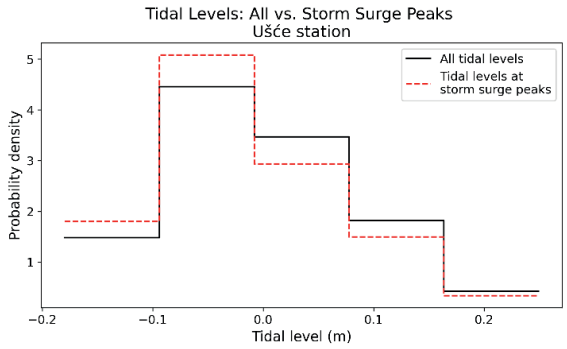

Figure 4. Histograms of tidal levels at the Prosika station for all tidal levels (black) and for tidal levels corresponding to the extracted highest 1% of storm surges (red dashed).

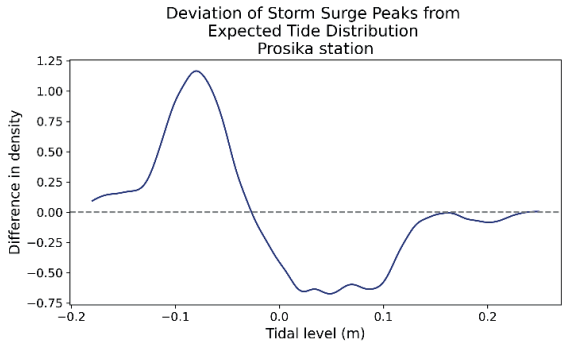

Figure 5. Deviation of the highest 1% of storm surges from the expected tidal distribution at the Prosika station.

For Prosika, the chi-squared test yields a χ^2 value of 79.30 at the 95% significance level. As for the Bakar station, this value greatly exceeds the critical value χ^2_{crit}, leading to a strong rejection of the null hypothesis of no TSI and indicating a substantial tide–surge interaction.

4.1.3 Southern Adriatic (Ušće)

Figure 6 presents histograms for the Ušće station. Both datasets exhibit their highest probability densities around average tidal levels, indicating that these conditions are the most frequent. In contrast, the lowest and highest tidal ranges display very low probability densities, confirming that extreme tidal levels are rare in both datasets. The largest differences between the two distributions occur in the central tidal ranges, whereas the outer ranges are nearly identical.

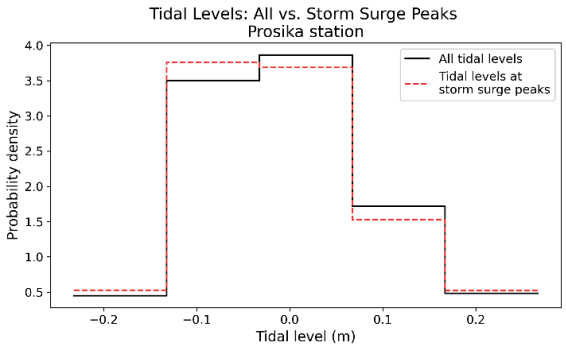

Figure 6. Histograms of tidal levels at the Ušće station for all tidal levels (black) and for tidal levels corresponding to the extracted highest 1% of storm surges (red dashed).

At the Ušće station, a deviation pattern similar to that observed at Prosika is evident in Fig. 7. The highest positive deviations occur around a tidal level of −0.1 m, after which the deviations become negative and decrease in magnitude. This pattern indicates that storm surge peaks tend to coincide with slightly lower-than-average tidal levels rather than with mean or extreme tides.

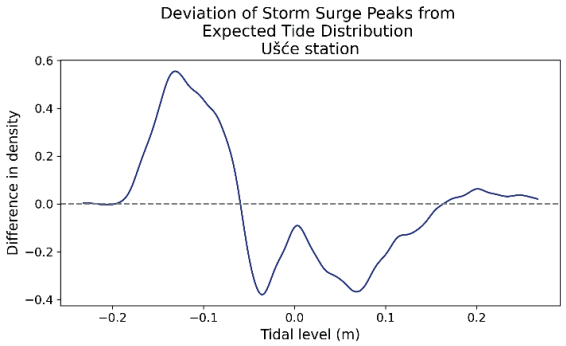

Figure 7. Deviation of the highest 1% of storm surges from the expected tidal distribution at the Ušće station.

For Ušće, the chi-squared test yields a χ^2 value of 18.44 at the 95% significance level. Since $\chi^2 > \chi^2_{crit}$, the null hypothesis is rejected, indicating a statistically significant difference between the distributions and confirming the presence of a notable tide–surge interaction.

4.2 Distribution of storm surges relative to high tide

4.2.1 Northern Adriatic (Bakar)

Figure 8 shows the distribution of storm surges relative to high tide at the Bakar station. The observed distribution appears relatively uniform across the tidal cycle, with only minor deviations from the expected uniform distribution. The absence of pronounced peaks or troughs in the histogram indicates minimal tide–surge interaction (TSI) at this location.

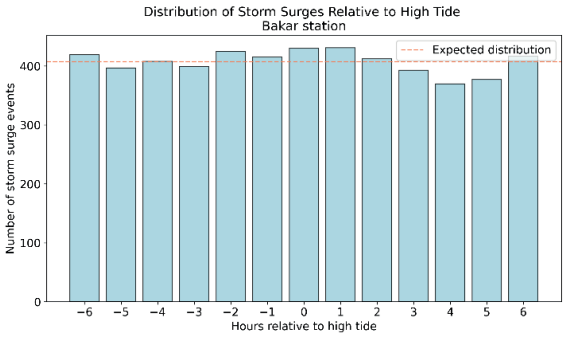

Figure 8. Distribution of the highest 1% of storm surges relative to high tide compared with the expected uniform distribution at the Bakar station.

To support the visual interpretation of Fig. 8, a chi-squared test was performed using a critical value of $\chi^2_{crit} = 21.03$ at the 95% significance level. The resulting χ^2 value of 10.79 is below χ^2_{crit}, confirming that no statistically significant TSI is present at Bakar.

4.2.2 Middle Adriatic (Prosika)

The distribution of storm surges at the Prosika station differs substantially from that observed at Bakar (Fig. 9). A higher frequency of storm surge events occurs five to six hours before high tide, as well as between three and six hours after high tide. Conversely, a noticeable reduction in storm surge occurrences is evident from three hours before to one hour after high tide. This pattern suggests that storm surges at Prosika are less likely to occur shortly before high tide and are more likely to occur toward the beginning and end of the tidal cycle.

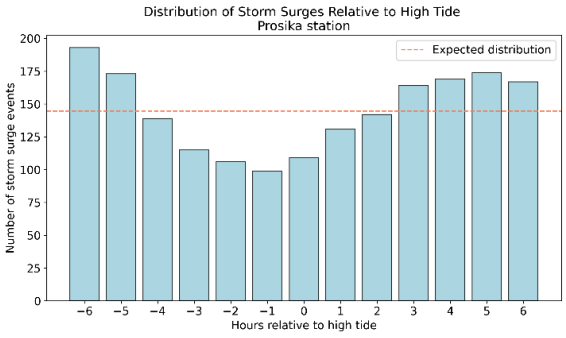

Figure 9. Distribution of the highest 1% of storm surges relative to high tide compared with the expected uniform distribution at the Prosika station.

The chi-squared test confirms the visual interpretation, yielding a χ^2 value of 78.95 at the 95% significance level. As this value is well above χ^2_{crit}, the null hypothesis of no TSI is strongly rejected, indicating a substantial tide–surge interaction at Prosika.

4.2.3 Southern Adriatic (Ušće)

Similar to Prosika, the distribution of storm surges at the Ušće station shows clear deviations from the expected uniform distribution (Fig. 10). As at Prosika, storm surges are less likely to occur shortly before high tide and more likely to occur toward the beginning and end of the tidal cycle.

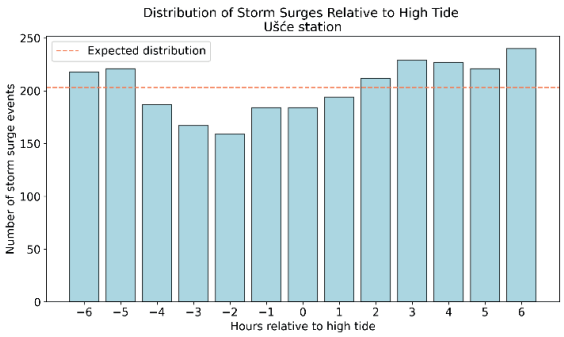

Figure 10. Distribution of the highest 1% of storm surges relative to high tide compared with the expected uniform distribution at the Ušće station.

The chi-squared test yields a χ^2 value of 38.68, which exceeds χ^2_{crit}, indicating that the distribution of storm surges differs significantly from a uniform distribution. Therefore, a statistically significant tide–surge interaction is present at Ušće.

4.3 Correlation between skew surges and high tides

4.3.1 Northern Adriatic (Bakar)

The relationship between the highest 1% of skew surges and the corresponding astronomical high tides at the Bakar station is shown in Fig. 11, together with a visual trend line. Kendall's τ for this station is −0.08 and is not statistically significant ($p > 0.05$), indicating no measurable dependence between skew surges and high tides.

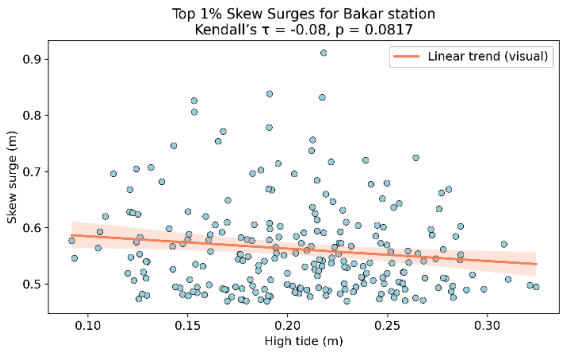

Figure 11. Scatter plot of the highest 1% of skew surges and corresponding high tides, including a visual trend line and Kendall's τ, at the Bakar station.

This lack of correlation suggests that skew surges at Bakar occur independently of astronomical high tides.

Figure 12 presents probability density functions (PDFs) of all high tides and of high tides associated with 99th-percentile skew surges, overlaid with a histogram of high tides during extreme skew surge events at Bakar. Both distributions exhibit a similar bell-shaped form, indicating that the distribution of high tides during extreme skew surges closely resembles the overall high-tide distribution. The peak of the black dashed curve is slightly shifted toward higher values compared with the orange curve, suggesting that extreme skew surges at Bakar tend to occur during slightly higher-than-average high tides.

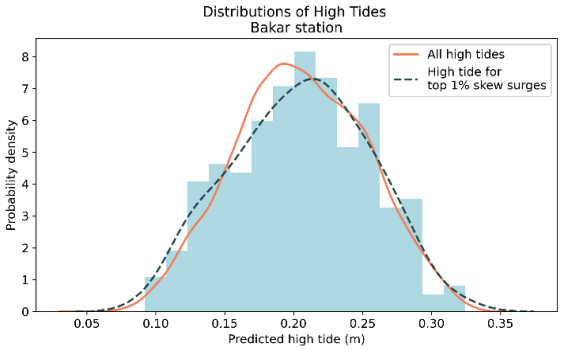

Figure 12. Probability density functions of all high tides and of high tides occurring during extreme skew surges, together with a histogram of high tides associated with skew surges at the Bakar station.

If skew surges and high tides are independent, high tides associated with extreme skew surges should follow the same distribution as all high tides (Williams et al., 2016). The Anderson–Darling test was therefore applied to compare the two distributions. The test failed to reject the null hypothesis ($p > 0.05$), indicating no statistically significant difference between them. Consequently, no significant tide–surge interaction is detected at the Bakar station based on this method.

4.3.2 Middle Adriatic (Prosika)

The correlation between the highest 1% of skew surges and the corresponding high tides at the Prosika station is shown in Fig. 13, together with a visual trend line. Kendall's τ for this location is −0.05 and is not statistically significant ($p > 0.05$). The absence of a statistically significant correlation indicates no dependency between skew surges and high tides and, therefore, no evidence of tide–surge interaction (TSI) at this station.

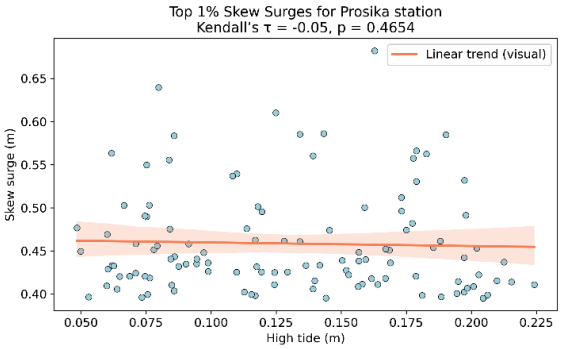

Figure 13. Scatter plot of the highest 1% of skew surges and corresponding high tides, together with a visual trend line and Kendall's τ, at the Prosika station.

Figure 14 presents the probability density functions (PDFs) and histogram for the Prosika station. The dashed black curve (high tides associated with extreme skew surges) peaks at lower tidal levels (≈0.07 m), whereas the orange curve (all high tides) peaks at slightly higher levels (≈0.10 m). This shift suggests that extreme skew surges at Prosika tend to occur more frequently during lower-than-average high tides.

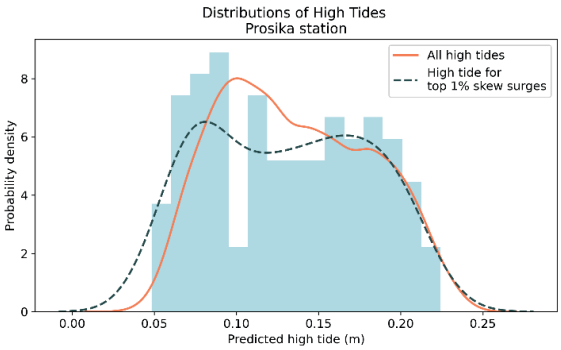

Figure 14. Probability density functions (PDFs) of all high tides and of high tides occurring during extreme skew surges, together with a histogram of high tides associated with skew surges at the Prosika station.

The Anderson–Darling test was applied to compare the distribution of all high tides with that of high tides associated with the highest 1% of skew surges at the Prosika station. The test statistic was 1.9504, slightly below the critical value of 1.9610 at the 95% significance level, with a p-value of 0.0510. Consequently, the null hypothesis of no difference between the distributions is not rejected.
This result indicates that there is no statistically significant difference between the two distributions, supporting the conclusion derived from Kendall's τ that no significant TSI is present at this station.

4.3.3 Southern Adriatic (Ušće)

The Ušće station exhibits the lowest correlation coefficient among the three locations, with a Kendall's τ value of −0.01 (Fig. 15). As for the other stations, this correlation is not statistically significant, indicating no meaningful relationship between skew surges and high tides and, consequently, no evidence of TSI at this location.

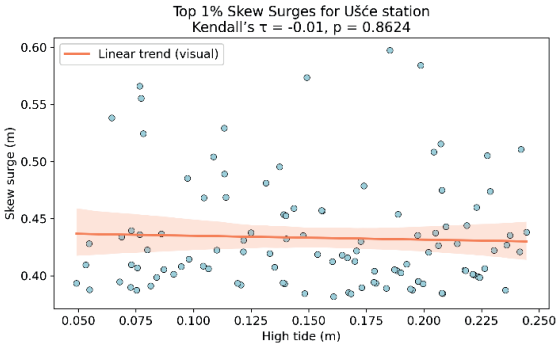

Figure 15. Scatter plot of the highest 1% of skew surges and corresponding high tides, together with a visual trend line and Kendall's τ, at the Ušće station.

The differences between the distributions shown in Fig. 16 were assessed using the Anderson–Darling test. As expected, no statistically significant difference was identified. The test statistic was −0.5716, which is well below the critical value of 1.9610 at the 95% significance level, confirming the absence of significant TSI at the Ušće station.

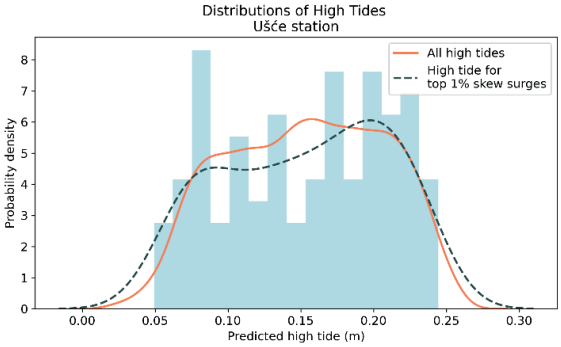

Figure 16. Probability density functions (PDFs) of all high tides and of high tides occurring during extreme skew surges, together with a histogram of high tides associated with skew surges at the Ušće station.

4.4 Discussion

The analysis of tide–surge interaction (TSI) at the three tide gauge stations along the Croatian Adriatic coast produced method-dependent results, with no station showing consistent evidence of TSI across all applied approaches.

At the northern Adriatic station, Bakar, TSI was identified only by the method based on the distribution of extreme storm surges across tidal ranges (Dixon & Tawn, 1994). In contrast, the second method (Haigh et al., 2010) , which evaluates whether extreme storm surges preferentially occur during high tides, and the third method (Williams et al., 2016), which examines the correlation and distributional similarity between skew surges and high tides, both failed to detect statistically significant TSI. This lack of agreement among methods supports the conclusion that TSI at Bakar is weak or not statistically significant.

At the middle Adriatic station, Prosika, both the first and second methods indicated statistically significant TSI, suggesting that extreme storm surges tend to occur under specific tidal conditions. However, the third method revealed no significant correlation between skew surges and high tides, and the Anderson–Darling test statistic (1.9504) did not exceed the 5% critical value (1.9610), yielding a p-value of 0.0510. Although close to the significance threshold, this result does not justify rejection of the null hypothesis. This inconsistency introduces uncertainty: while two methods suggest the presence of TSI, the absence of confirmation from the third method renders the overall result inconclusive.

A similar pattern was observed at the southern Adriatic station, Ušće. Again, the first two methods indicated significant TSI, whereas the third method did not. The correlation between skew surges and high tides was negligible ($\tau = -0.01$), and no statistically significant difference was found between the relevant tidal distributions.

The systematic non-detection of TSI by the third method, despite contrasting results from the other two approaches, may be attributed to its stricter statistical requirements and reduced sensitivity when applied to limited samples of extreme events. In particular, the relatively small number of extreme skew surges may reduce the statistical power of the Anderson–Darling test to identify meaningful deviations. Consequently, the failure of the third method to detect TSI should be interpreted with caution, especially when its results contradict those of multiple independent methods.

CONCLUSIONS

To examine whether extreme storm surges tend to coincide with high tides along the Croatian Adriatic coast, three complementary statistical methods were applied at the Bakar, Prosika, and Ušće tide gauge stations, representing the northern, middle, and southern Adriatic, respectively.

While the first two methods provided evidence of tide–surge interaction (TSI) at the middle and southern Adriatic stations, the third method consistently failed to confirm any statistically significant interaction. The differing outcomes among the three methods can be attributed to the fact that they capture distinct aspects of TSI.

The first method, based on histogram and deviation analyses, offers a direct visual and statistical comparison between tidal levels at storm surge peaks and the overall tidal distribution, making it sensitive to preferential occurrence at specific tidal levels. The second method, which examines the timing of storm surges relative to high tides, focuses on the distribution of surge events across the tidal cycle and is better suited to identify systematic clustering around particular tidal phases. In contrast, the skew surge–high tide correlation approach tests for statistical dependence between two variables, assessing whether extreme surges preferentially coincide with high tides; however, it may overlook interactions occurring at lower or intermediate tidal levels. Consequently, discrepancies among the three methods arise because they quantify different manifestations of TSI—namely, distributional differences, phase preferences, or direct statistical dependence.

Given the lack of consistent agreement across methods and the stringent criteria of the skew surge–based approach, the overall results suggest that storm surges and tides along the Croatian Adriatic coast generally occur independently, with no conclusive evidence of statistically significant tide–surge interaction.

Future research will focus on the application of non-stationary harmonic analysis techniques (e.g., NS_Tide) to explicitly identify potential interactions between storm surges and tides, as well as the modulation of tidal constituents during extreme surge events. Such analyses may provide additional insight into compound sea-level dynamics that can substantially influence coastal flooding.

ACKNOWLEDGEMENTS

This work was supported by the Croatian Science Foundation under the project “Compound Flooding in Coastal Croatia under Present and Future Climate” (4SeaFlood, project number IP-2022-10-7598), and by the University of Rijeka

through projects uniri-iskusni-tehnic-23-83 and uniri-iskusni-tehnic-23-74. The authors gratefully acknowledge Croatian Waters and the Croatian Meteorological and Hydrological Service for providing the observational data.

REFERENCES

Antony, C., Unnikrishnan, A. S., Krien, Y., Murty, P. L. N., Samiksha, S. V., & Islam, A. K. M. S. (2020). Tide–surge interaction at the head of the Bay of Bengal during Cyclone Aila. *Regional Studies in Marine Science*, *35*, 101133. https://doi.org/10.1016/j.rsma.2020.101133

Arns, A., Wahl, T., Wolff, C., Vafeidis, A. T., Haigh, I. D., Woodworth, P., Niehüser, S., & Jensen, J. (2020). Non-linear interaction modulates global extreme sea levels, coastal flood exposure, and impacts. *Nature Communications*, *11*(1), 1918. https://doi.org/10.1038/s41467-020-15752-5

Cavaleri, L., Bajo, M., Barbariol, F., Bastianini, M., Benetazzo, A., Bertotti, L., Chiggiato, J., Davolio, S., Ferrarin, C., Magnusson, L., Papa, A., Pezzutto, P., Pomaro, A., & Umgiesser, G. (2019). The October 29, 2018 storm in Northern Italy – An exceptional event and its modeling. *Progress in Oceanography*, *178*, 102178. https://doi.org/10.1016/j.pocean.2019.102178

Cerovečki, I., Orlić, M., & Hendershott, M. C. (1997). Adriatic seiche decay and energy loss to the Mediterranean. *Deep Sea Research Part I: Oceanographic Research Papers*, *44*(12), 2007–2029. https://doi.org/10.1016/S0967-0637(97)00056-3

Codiga, D. L. (2011). Unified Tidal Analysis and Prediction Using the UTide Matlab Functions. *Technical Report 2011-01. Graduate School of Oceanography, University of Rhode Island, Narragansett, RI*, 59.

Costa, W., Bryan, K. R., Stephens, S. A., & Coco, G. (2023). A regional analysis of tide-surge interactions during extreme water levels in complex coastal systems of Aotearoa New Zealand. *Frontiers in Marine Science*, *10*. https://doi.org/10.3389/fmars.2023.1170756

Dixon, M. J., & Tawn, J. A. (1994). Estimates of extreme sea conditions: Extreme sea levels at the UK A-Class sites: Site-by-site analyses. *Proudman Oceanographic Laboratory Internal Document No. 65*.

Ferrarin, C., Lionello, P., Orlić, M., Raicich, F., & Salvadori, G. (2022). Venice as a paradigm of coastal flooding under multiple compound drivers. *Scientific Reports*, *12*(1), 5754. https://doi.org/10.1038/s41598-022-09652-5

Green, J., Haigh, I. D., Quinn, N., Neal, J., Wahl, T., Wood, M., Eilander, D., de Ruiter, M., Ward, P., & Camus, P. (2024). Review article: A comprehensive review of compound flooding literature with a focus on coastal and estuarine regions. *Natural Hazards and Earth System Sciences*, *25*(2), 747–816. https://doi.org/10.5194/nhess-25-747-2025

Haigh, I., Nicholls, R., & Wells, N. (2010). Assessing changes in extreme sea levels: Application to the English Channel, 1900–2006. *Continental Shelf Research*, *30*(9), 1042–1055. https://doi.org/10.1016/j.csr.2010.02.002

Haigh, I., Wadey, M. P., Wahl, T., Ozsoy, O., Nicholls, R. J., Brown, J. M., Horsburgh, K., & Gouldby, B. (2016). Spatial and temporal analysis of extreme sea level and storm surge events around the coastline of the UK. *Scientific Data*, *3*(1), 160107. https://doi.org/10.1038/sdata.2016.107

Horsburgh, K. J., & Wilson, C. (2007). Tide-surge interaction and its role in the distribution of surge residuals in the North Sea. *Journal of Geophysical Research: Oceans*, *112*(C8). https://doi.org/10.1029/2006JC004033

Idier, D., Dumas, F., & Muller, H. (2012). Tide-surge interaction in the English Channel. *Natural Hazards and Earth System Sciences*, *12*(12), 3709–3718. https://doi.org/10.5194/nhess-12-3709-2012

Janeković, I., & Kuzmić, M. (2005). Numerical simulation of the Adriatic Sea principal tidal constituents. *Annales Geophysicae*, *23*(10), 3207–3218. https://doi.org/10.5194/angeo-23-3207-2005

Krvavica, N., Gržić, M. M., Innocenti, S., & Matte, P. (2024). Impact of storm surge and power peaking on tidal-fluvial processes in microtidal Neretva River estuary. *Estuarine, Coastal and Shelf Science*, *318*, 109227. https://doi.org/10.1016/j.ecss.2025.109227

Li, G., Peng, H., Zhang, J., & Zhu, L. (2012). Robust rank correlation based screening. *The Annals of Statistics*, *40*(3), 1846–1877. https://doi.org/10.1214/12-AOS1024

Liu, W.-C., Huang, W.-C., & Chen, W.-B. (2016). Modeling the interaction between tides and storm surges for the Taiwan coast. *Environmental Fluid Mechanics*, *16*(4), 721–745. https://doi.org/10.1007/s10652-015-9441-0

Međugorac, I., Orlić, M., Janeković, I., Pasarić, Z., & Pasarić, M. (2018). Adriatic storm surges and related cross-basin sea-level slope. *Journal of Marine Systems*, *181*, 79–90. https://doi.org/10.1016/j.jmarsys.2018.02.005

Međugorac, I., Pasarić, M., & Orlić, M. (2022). Long-term measurements at Bakar tide-gauge station (east Adriatic). *Geofizika*, *39*(1), Article 1. https://doi.org/10.15233/gfz.2022.39.8

Međugorac, I., Pasarić, M., & Orlić, M. (n.d.). *Historical sea-level measurements at Bakar (east Adriatic)* [Dataset]. SEANOE. https://doi.org/10.17882/85171

Međugorac, I., Pasarić, M., Pasarić, Z., & Orlić, M. (2016). Two recent storm-surge episodes in the Adriatic. *International Journal of Safety and Security Engineering*, *6*(3), 589–596. Scopus. https://doi.org/10.2495/SAFE-V6-N3-589-596

Medvedev, I. P., Vilibić, I., & Rabinovich, A. B. (2020). Tidal Resonance in the Adriatic Sea: Observational Evidence. *Journal of Geophysical Research: Oceans*, *125*(8), e2020JC016168. https://doi.org/10.1029/2020JC016168

Pinheiro, J. P., Lopes, C. L., Ribeiro, A. S., Sousa, M. C., & Dias, J. M. (2020). Tide-surge interaction in Ria de Aveiro lagoon and its influence in local inundation patterns.

Continental Shelf Research, *200*, 104132. https://doi.org/10.1016/j.csr.2020.104132

Pugh, D., & Woodworth, P. (2014). *Sea-Level Science: Understanding Tides, Surges, Tsunamis and Mean Sea-Level Changes*. Cambridge University Press. https://doi.org/10.1017/CBO9781139235778

Santamaria-Aguilar, S., & Vafeidis, A. T. (2018). Are Extreme Skew Surges Independent of High Water Levels in a Mixed Semidiurnal Tidal Regime? *Journal of Geophysical Research: Oceans*, *123*(12), 8877–8886. https://doi.org/10.1029/2018JC014282

Šepić, J., Pasarić, M., Međugorac, I., Vilibić, I., Karlović, M., & Mlinar, M. (2022). Climatology and process-oriented analysis of the Adriatic sea level extremes. *Progress in Oceanography*, *209*, 102908. https://doi.org/10.1016/j.pocean.2022.102908

Vilibić, I., Šepić, J., Pasarić, M., & Orlić, M. (2017). The Adriatic Sea: A Long-Standing Laboratory for Sea Level Studies. *Pure and Applied Geophysics*, *174*(10), 3765–3811. https://doi.org/10.1007/s00024-017-1625-8

Williams, J., Horsburgh, K. J., Williams, J. A., & Proctor, R. N. F. (2016). Tide and skew surge independence: New insights for flood risk. *Geophysical Research Letters*, *43*(12), 6410–6417. https://doi.org/10.1002/2016GL069522

Zhang, H., Cheng, W., Qiu, X., Feng, X., & Gong, W. (2017). Tide-surge interaction along the east coast of the Leizhou Peninsula, South China Sea. *Continental Shelf Research*, *142*, 32–49. https://doi.org/10.1016/j.csr.2017.05.015

DOI: https://doi.org/10.53256/COSE_240105

Application of Remote Sensing in the Design and Monitoring of Coastal Structures

I. Petković[a], N. Šuput[b], I. Žigo[c], N. Krvavica[a], I. Ružić[a]
[a] *University of Rijeka, Faculty of Civil Engineering, Croatia*
[b] *BSK Commerce d.o.o., Croatia*
[c] *MareCon d.o.o., Croatia*

[*] *Corresponding author: ipetkovic@uniri.hr*

ABSTRACT: Evolving coastal hazards require survey methods that are rapid, accurate, and cost-efficient. This study presents a field-tested, RTK-anchored multisensor workflow that integrates Unmanned Aerial Vehicle (UAV) and handheld Structure-from-Motion (SfM) photogrammetry, smartphone LiDAR (sLiDAR), and terrestrial laser scanning (TLS) to generate engineering-grade point clouds of rubble-mound breakwaters. All datasets are co-registered within a unified control network, quality-controlled, and processed to extract key geometric parameters, including berm width, crown elevation, and cross-sectional profiles. Hybrid uncertainty is quantified by combining M3C2 normal-direction distances with alignment root-mean-square residuals to derive a 95% level of detection (LoD95), enabling robust centimetre-scale change detection. The proposed workflow is demonstrated at two Adriatic sites representative of common breakwater typologies. At the Pećine municipal breakwater, overlapping datasets are analysed using M3C2 comparison and transverse profiles to assess internal consistency and method-specific performance. At the Marina Mitan composite breakwater, transverse and longitudinal profiles derived from handheld SfM and sLiDAR are directly compared with design documentation to evaluate as-built compliance. Across both sites, sLiDAR effectively resolves undercuts and porous interior features that are partially occluded in image-based datasets, while aerial and handheld SfM provide rapid, high-density coverage in accessible and well-lit areas. TLS delivers a highly accurate reference dataset where safe access and instrument placement are feasible, albeit with greater logistical effort.The results highlight the growing importance of remote sensing techniques in contemporary coastal engineering practice and support their broader application across the design, construction, and maintenance phases of coastal infrastructure. By providing a reproducible framework for data acquisition, co-registration, and uncertainty assessment, this study reduces barriers related to processing complexity and initial investment, thereby enabling operational monitoring of critical coastal structures.

KEYWORDS: Rubble-mound breakwaters, Structure-from-Motion, Smartphone LiDAR, Photogrammetry, M3C2

1 INTRODUCTION

The increasing frequency and severity of coastal hazards driven by sea-level rise, storm intensification, and human interventions have underscored the need for rapid, accurate, and cost-effective surveying of coastal infrastructure. Traditional approaches, such as total station surveys, manual levelling, and classical aerial photogrammetry, require extensive field campaigns, specialised equipment, and skilled operators, which can limit spatial coverage and monitoring frequency (Campbell and Wynne, 2011; Wang, 2009). As coastal structures age and the impacts of extreme events intensify, engineering practice increasingly benefits from innovative methods that deliver high-quality three-dimensional (3D) information with reduced logistical effort and cost (James et al., 2013).

Recent advances in remote sensing (RS) have enabled detailed 3D mapping and structural assessment across complex coastal environments. Structure-from-Motion (SfM) photogrammetry reconstructs dense point clouds from overlapping

imagery acquired by unmanned aerial vehicles (UAVs) and handheld cameras. It routinely achieves centimetre-level accuracy and is well suited for monitoring coastal morphodynamics, including beach profiles, cliff erosion, and the geometry of breakwaters (Ružić et al., 2014, 2019; Tadić et al., 2022; Petković, 2023). Light Detection and Ranging (LiDAR) provides direct range measurements capable of capturing fine-scale surface detail and has been widely applied to extract precise geometry and detect small-scale changes in rubble-mound structures (Puente et al., 2014). More recently, the growing availability of smartphone-based LiDAR (sLiDAR) has extended data acquisition to confined and porous zones that are difficult to survey using aerial imagery or terrestrial laser scanning (TLS), thereby complementing both SfM and TLS in coastal applications (Błaszczak-Bąk et al., 2023; Syafie et al., 2024; Šuput, 2023).

This study advances current practice by integrating multiple RS platforms within a single Real-Time Kinematic (RTK)-referenced workflow for surveying rubble-mound breakwaters. The proposed workflow combines UAV-based SfM, handheld SfM, TLS, and sLiDAR, and provides practical guidance for both field acquisition and data processing using readily available hardware and commonly employed software. A unified RTK-anchored control network supports the co-registration of all datasets, after which point clouds are aligned, quality-controlled, and sectioned to extract key engineering parameters such as berm width, crown elevation, and cross-sectional geometry. Uncertainty propagation within the hybrid point clouds is explicitly addressed: normal-direction distances derived from the Multiscale Model-to-Model Cloud Comparison (M3C2) algorithm are combined with the root-mean-square (RMS) alignment residuals to estimate hybrid uncertainty and derive a Level of Detection at the 95% confidence level (LoD95), which frames all reported differences.

The proposed approach is demonstrated at two Adriatic sites representing common breakwater typologies. At the Pećine municipal breakwater, overlapping datasets are compared using M3C2 analysis and transverse profiles to assess internal consistency and method-specific performance. At the Marina Mitan composite breakwater, transverse and longitudinal profiles derived from handheld SfM and sLiDAR are directly compared with design documentation to evaluate as-built compliance. Across both sites, sLiDAR proves effective in capturing undercuts and porous regions that are partially occluded in image-based datasets, while aerial and handheld SfM provide rapid coverage and high point densities in accessible, well-lit areas.

2 STUDY AREAS AND MATERIALS

2.1 Research area

Two study sites were investigated in this work. The first site is the Pećine breakwater, located along the Pećine coastline in the city of Rijeka, Croatia (regional location in Fig. 1a; UAV view in Fig. 1b). The Pećine area is characterised by a rocky coastline with a series of small coves and pocket beaches.

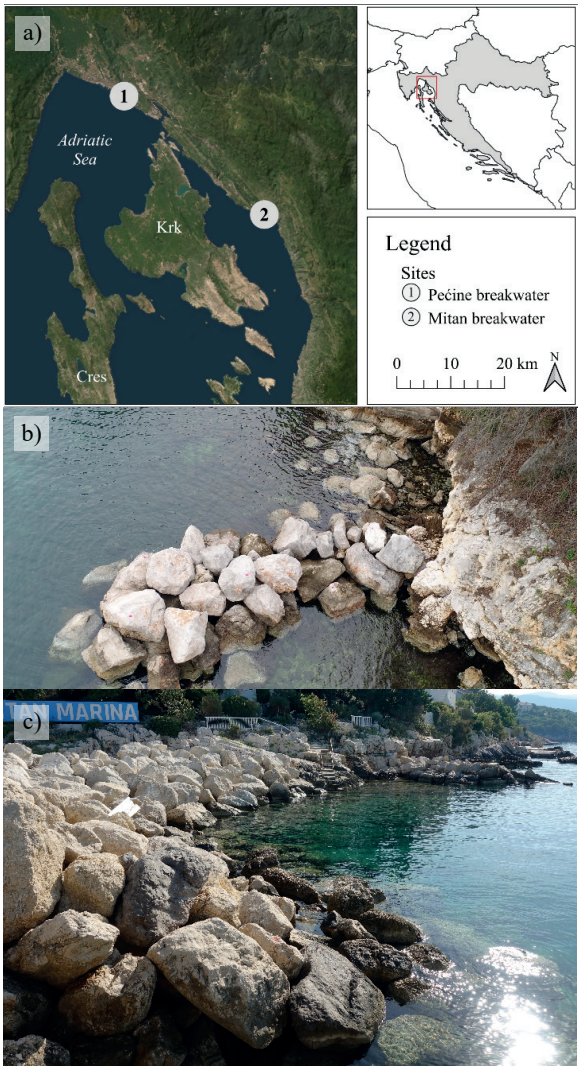

Figure 1. Study area and breakwater sites.
a) Regional location of the two investigated breakwaters on the northern Adriatic coast, showing the Pećine breakwater (site 1) in Rijeka and the Mitan breakwater (site 2) in Novi Vinodolski (basemap: ESRI World Imagery).
b) Secondary rubble-mound Pećine breakwater (site 1).
c) Rubble-mound Mitan breakwater (site 2).

The analysed segment corresponds to Crnej Beach, situated immediately adjacent to the entrance of the Pećine small municipal harbour. This study focuses on a secondary breakwater within the municipal harbour, constructed at a later stage as a simple rubble-mound structure approximately 12 m in length to mitigate wave agitation within the harbour basin. This structure is hereafter referred to as the *Pećine breakwater*.
The second study area is the rubble-mound section of a composite breakwater located at the south-eastern corner of Marina Mitan, in the city of Novi Vinodolski (regional location in Fig. 1a; shoreline photograph in Fig. 1c), hereafter referred to as the *Mitan breakwater*. The Mitan breakwater extends approximately 25 m in each direction and has an above-sea-level width of about 7 m. This structure was selected due to its representative geometry and good accessibility, providing an opportunity to assess the applicability of remote sensing (RS) methods to a commonly encountered breakwater typology.

2.2 Survey equipment

To conduct a comprehensive geometric survey of coastal structures, five complementary components were integrated into a cohesive workflow to leverage their individual strengths. The survey began with a FARO Focus3D X 130 terrestrial laser scanner (TLS), which provides millimetre-level accuracy and high-density point clouds, capturing fine surface details and precise armour-unit placement. These data form a detailed geometric baseline of the exposed armour layer.
Building on this static reference framework, a DJI Phantom 4 Advanced unmanned aerial vehicle (UAV) was employed to extend spatial coverage into broader, hard-to-access areas. The UAV acquires high-overlap aerial imagery, effectively bridging gaps in regions shadowed or occluded from ground-based scanning.
To address undercut features and interstitial voids beyond the reach of both TLS and UAV photogrammetry, smartphone LiDAR (sLiDAR) data were collected using an Apple iPhone 13 Pro. This system provides close-range depth measurements with centimetre-scale precision, enabling the infilling of localized gaps within the point cloud.
Handheld photogrammetry, performed using a Sony RX100 Mark V camera, offered flexible, high-resolution data acquisition and proved particularly effective on textured surfaces and partially occluded rock faces. This method requires minimal operator training and enriches the dataset with colour and material information that range-only sensors cannot capture.
Finally, a GNSS–RTK system ensured sub-decimetre positional accuracy across all measurements, allowing UAV-derived models, TLS point clouds, sLiDAR scans, and handheld Structure-from-Motion (SfM) reconstructions to be co-registered within a single, unified coordinate framework.

3 METHODOLOGY

3.1 Data acquisition

Field campaigns were conducted on three occasions (two at Crnej and one at Mitan) to acquire high-resolution three-dimensional (3D) data of two rubble-mound breakwaters. A unified georeferencing procedure was implemented at all sites. High-contrast ground control targets (painted panels and spray-painted markers) were distributed around the perimeter and across accessible surfaces, and a GNSS–RTK survey was then used to record centimetre-level coordinates for each ground control point (GCP). This established a rigid control network for the subsequent co-registration of all datasets.
Following the establishment of the GCP network, multisensor data acquisition was carried out according to site-specific conditions. Static terrestrial laser scanning (TLS) was employed where unobstructed vantage points allowed the capture of dense 3D point clouds. Unmanned aerial vehicle (UAV) flights provided overlapping oblique imagery for Structure-from-Motion (SfM) photogrammetric reconstruction, while handheld devices—smartphone LiDAR (sLiDAR) and a digital camera—were used to document undercut sections, overhangs, and confined spaces inaccessible to TLS or UAV platforms. All point clouds and image datasets were referenced to the same control network and co-registered to produce unified, high-fidelity site models.

3.1.1 Pećine breakwater survey

Data were collected under overcast, low-wind conditions to minimise shadows and surface ripples (Table 1 summarises the acquisition dates, platforms, and settings). The first campaign (February 2023) combined TLS using a FARO Focus3D X 130 with three tripod stations positioned around the site (three scans acquired in approximately 30 min). As the breakwater lay at the edge of the mapped area, the landward side was not fully captured. A concurrent UAV survey was conducted using a DJI Phantom 4 Advanced, which flew low-altitude oblique paths at

approximately 45° for 15 min, acquiring 220 images for SfM reconstruction.

To document undercuts and a small coastal cave along the breakwater face, smartphone LiDAR (iPhone 13 Pro) was operated at close range. A second campaign (June 2023) employed handheld SfM using a Sony RX100 Mark V camera; 340 overlapping photographs were acquired from multiple land-based viewpoints over approximately 30 min, covering the structure from the base to the crown.

All datasets were georeferenced to the common GNSS–RTK control network and subsequently co-registered into a single, high-resolution 3D model of the Pećine breakwater.

Table 1. Acquisition details for the Pećine breakwater surveys.

Survey No.	Date	Method and equipment
1	21.02.2023	SfM (UAV) DJI Phantom 4 Advanced
1	21.02.2023	TLS Focus3D X 130
1	21.02.2023	sLiDAR iPhone 13 Pro
2	30.06.2023	SfM handheld Sony RX100 Mark V

3.1.2 Marina Mitan breakwater survey

On 11 September 2023, a ground control network was established across the Marina Mitan breakwater and surveyed using GNSS–RTK. Under clear and calm weather conditions, handheld Structure-from-Motion (SfM) photogrammetry was carried out using a Sony RX100 Mark V camera. A total of 540 overlapping photographs were acquired over approximately 1 hour, with an overlap of at least 60%, covering the structure from the base to the crown. In parallel, smartphone LiDAR (sLiDAR; iPhone 13 Pro) was operated at close range to capture the interior geometry through accessible voids within the armour layer.

The approximately 30 m long rubble-mound section was selected as a test site to evaluate the effectiveness of sLiDAR as a complementary technique to handheld SfM photogrammetry. Following data acquisition, all ground control points were re-measured using GNSS–RTK to verify positional integrity. The handheld SfM imagery and sLiDAR point cloud were then referenced to the same control network and co-registered into a unified spatial dataset.

The methods and equipment used for Survey 3 at the Marina Mitan breakwater are summarised in Table 2.

Table 2. Acquisition details for the Marina Mitan breakwater survey.

Survey No.	Date	Method and equipment
3	11.09.2023	sLiDAR iPhone 13 Pro
3	11.09.2023	SfM (handheld) Sony RX100 Mark V

3.2 Data processing

This section outlines the data-processing workflow applied to all datasets. Imagery acquired using UAV- and handheld-based Structure-from-Motion (SfM), terrestrial laser scanning (TLS) data, and smartphone LiDAR (sLiDAR) point clouds were imported into dedicated software environments for preprocessing and georeferencing. All outputs were referenced to the same GNSS–RTK control network to ensure spatial consistency.

All SfM photographs were processed using Agisoft Metashape (v1.8). Image quality was evaluated using the Estimate Image Quality tool, and frames with quality scores below 0.50 were excluded, in accordance with the software documentation and established best practices (Agisoft, 2021; Over et al., 2021). UAV images, which include approximate camera positions stored in EXIF metadata, were aligned using the Reference Preselection option, while handheld images without geotags were aligned using the High Accuracy preset.

Following initial alignment, low-confidence tie points—characterized by a low number of observations and high reprojection errors—were removed through Gradual Selection and manual inspection. Dense point clouds were subsequently generated using the High quality setting, resulting in approximately 3–7 million points per breakwater (UAV-derived point cloud shown in Fig. 2; handheld SfM-derived point cloud shown in Fig. 3).

Ground control coordinates for 11 targets, obtained from the GNSS–RTK survey and referenced to the HTRS96 / Croatia TM coordinate system (EPSG:3765), were imported into the project, manually marked, and used to refine model scale and orientation. The final

alignment to the control network achieved centimetre-level accuracy.

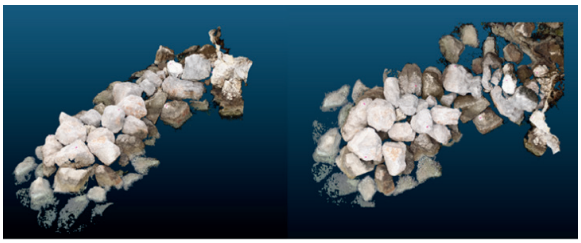

Figure 2. UAV-SfM 3D point cloud of the Pećine breakwater generated in Agisoft Metashape.

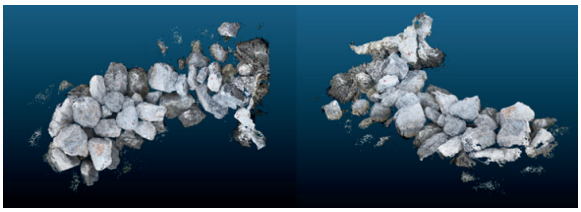

Figure 3. Handheld SfM 3D point cloud of the Pećine breakwater generated in Agisoft Metashape.

To generate a 3D point cloud of the Pećine breakwater using terrestrial laser scanning (TLS), data acquired with the FARO Focus3D X 130 were processed in FARO Scene (v2019). Noise filtering was enabled (Filter Stray Scan Points, grid size: 3 px, distance threshold: 0.02 m), and the resolution was set to Fine (corresponding to a point spacing of 1.56 mm at a range of 10 m) (FARO Technologies Inc., 2015). Three scan stations were registered using the instrument's onboard orientation sensors to preserve relative pose. Because the rubble-mound structure was only partially accessible, the TLS survey captured the seaward face of the breakwater and the adjacent Crnej Beach, while the landward face and crest were incompletely surveyed (Fig. 4). Consequently, full surface meshing of the structure was not attempted.

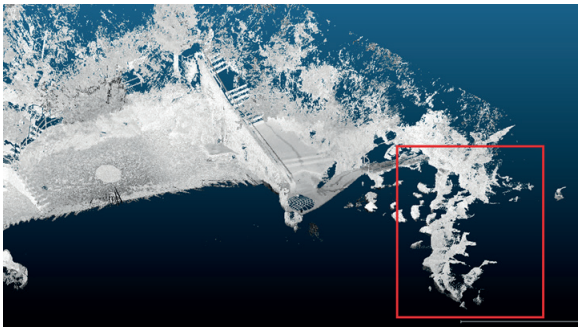

Figure 4. Partial TLS point cloud of the Crnej Beach area processed in CloudCompare, showing points captured from one side of the Pećine breakwater structure (highlighted in red).

The Mitan breakwater was surveyed in three segments using the Scaniverse application on an iPhone 13 Pro. The main segment covered approximately 30 m of the structure, while two auxiliary segments ranged between 5 and 10 m in length. Following device-side processing, the point clouds were exported and imported into CloudCompare for georeferencing and cross-section extraction (CloudCompare Wiki, 2023) (Fig. 5).

Figure 5. Segment of the Mitan breakwater point cloud acquired using sLiDAR scanning.

All point clouds and image-derived models were referenced to the same GNSS–RTK control network and subsequently rigidly aligned and quality-checked prior to analysis. The following sections describe the quantification of overlap uncertainty—combining M3C2 normal-direction distances with alignment root-mean-square (RMS) values—and the extraction of engineering cross-sections.

3.3 Error propagation in hybrid point clouds

Uncertainty in multi-sensor point cloud overlaps was quantified in CloudCompare by combining the alignment RMS of registration residuals with surface-normal distances computed using the Multiscale Model to Model Cloud Comparison (M3C2) algorithm (Lague et al., 2013). Registration was performed using point-pair matching followed by Iterative Closest Point (ICP) alignment. The alignment RMS represents the root mean square of closest-point residuals after rigid registration and is reported in metres.

M3C2 computes normal-direction distances by estimating local surface normals via principal component analysis using a diameter of $D = 0.03$ m. A normal-aligned projection cylinder (projection diameter: 0.05 m; maximum depth: 0.50 m) is then used to identify neighbouring points from both point clouds. These neighbours are projected onto the normal direction, and the mean positions μ_1 and μ_2 are calculated for the reference and compared clouds, respectively.

Their difference defines the signed separation distance d (Eq. 1):

$$d = \mu_2 - \mu_1 \quad (1)$$

Two quality metrics were evaluated for each core point: the number of supporting points in each cloud ($N_{pts1,2}$) and the local surface roughness ($STD_{1,2}$). Statistical summaries were computed for a high-confidence subset defined by $N_{pts1,2} \geq 20$, $STD_{1,2} \leq 0.05$ m, and an analysis window $|d| \leq 0.01$ m (coverage statistics are additionally reported for $|d| \leq 0.03$ m). The relative dispersion σ_{rel} was calculated as the standard deviation of d within this subset.

The hybrid uncertainty σ_{hyb} was then defined according to Eq. (2), where σ_{reg} denotes the alignment RMS:

$$\sigma_{hyb} = \sqrt{\sigma_{rel}^2 + \sigma_{reg}^2} \quad (2)$$

The minimum detectable change at the 95% confidence level, also referred to as the Level of Detection (LoD95), was subsequently derived (Eq. 3), following established practice in M3C2-based change detection (James et al. 2017; Winiwarter et al. 2021; Lague et al. 2013).

$$LoD_{95} = 1.96\sigma_{hyb} \quad (3)$$

3.4 Extraction of Point-Cloud Cross-Sections

Cross-sections were extracted from the merged point clouds of the Pećine breakwater using CloudCompare, following consistent procedures across all sensing methods. A longitudinal reference axis was first defined along the breakwater crest, after which four transverse axes were positioned at 2.5 m intervals, oriented perpendicular to the longitudinal axis. An example of the axis configuration applied to the UAV-SfM point cloud is shown in Fig. 6. Slicing the point cloud along these axes yielded narrow two-dimensional profiles through the armour layer. An example of the extracted UAV-SfM cross-sections is presented in Fig. 7.

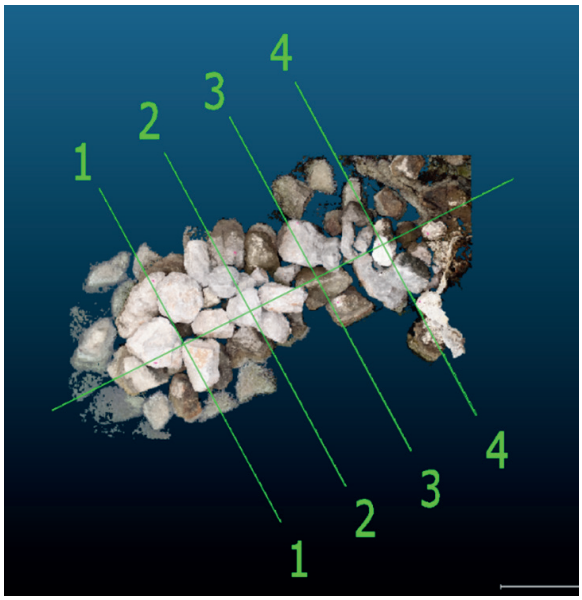

Figure 6. Example of longitudinal and transverse axes defined on the UAV-SfM point cloud of the Pećine breakwater in CloudCompare.

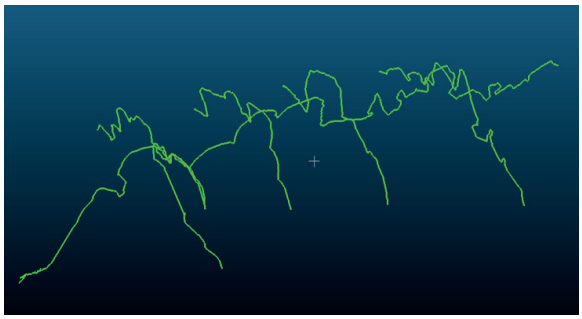

Figure 7. Example of cross-sections extracted from the UAV-SfM point cloud, showing Pećine breakwater profiles generated in CloudCompare.

For each sensing method, the extracted cross-sections—representing only the outer surface of the breakwater—were trimmed to their uppermost contours and exported as DXF polylines. These DXF files were subsequently imported into AutoCAD to remove redundant vertices and standardize line styles. The four transverse profiles derived from each method were then overlaid to enable direct geometric comparison (Fig. 8).

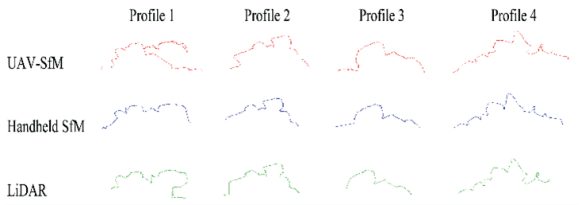

Figure 8. Four transverse cross-sections derived from UAV-SfM, handheld SfM, and sLiDAR data, exported as DXF files and edited in AutoCAD.

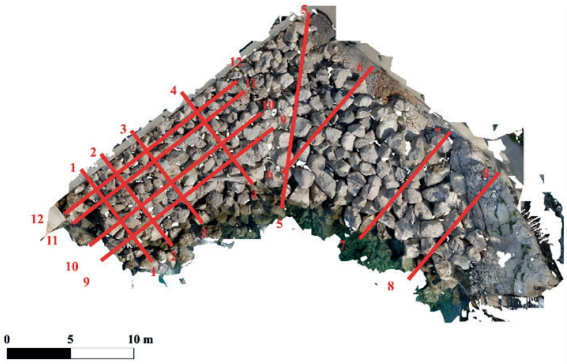

Figure 9. Selected transverse and longitudinal profiles delineated on the Mitan breakwater point cloud in AutoCAD.

Three-dimensional point clouds obtained from SfM photogrammetry and sLiDAR were also used to evaluate the as-built geometry of the Mitan breakwater against its original design documentation. Following image processing in Agisoft Metashape, selected transverse and longitudinal profiles were delineated directly on the point cloud and drafted in AutoCAD (Fig. 9).

These profiles, together with the corresponding point cloud data, were exported in ASCII format and imported into MATLAB, where custom scripts were applied to generate numerical cross-sections for both sensing techniques. The resulting profiles were subsequently reimported into AutoCAD for graphical comparison with the design drawings.

3.5 Analysis of the survey methods employed

A comparative assessment of UAV-SfM, TLS, handheld SfM, and sLiDAR was conducted at the Pećine rubble-mound breakwater. Table 3 summarises the relative direct costs, required expertise, field acquisition time, and processing effort associated with each method, using harmonised categories. The comparison provides a practical decision-support matrix for selecting appropriate survey techniques in comparable coastal engineering applications.

Table 3. Relative time, cost, effort, and expertise associated with the *survey methods applied at the Pećine breakwater* (categories *are indicative and* standardised *across* survey *campaigns*).

Method	Direct cost (relative)	Required expertise	Acquisition time (field)	Processing time (operator)
UAV–SfM[1]	Medium to Low	Moderate	Low	Moderate
Handheld–SfM[2]	Low	Low to Moderate	Medium	Moderate
sLiDAR[3]	Very Low	Low	Low	Low to Moderate
TLS[4]	High	High	Medium	High

Notes:
[1] DJI Phantom 4 Advanced; [2] Sony RX100 V; [3] iPhone 13 Pro; [4] FARO Focus3D X130.
a) Acquisition time (field): Very Low < 15 min; Low 15–30 min; Medium 30–60 min; High > 60 min.
b) Direct cost (indicative incremental per survey): Very Low: €0–€50 per day (smartphone or application already owned); Low: €20–€60 per day to rent, or approximately €500–€1,000 to purchase a consumer-grade camera; Medium to Low: €80–€200 per day to rent, or approximately €1,200–€2,500 to purchase a prosumer UAV; High: €300–€800 per day to rent, or approximately €20,000–€60,000 to purchase a TLS unit.
c) Processing effort (operator time, excluding computation): Very Low < 1 h; Low 1–2 h; Moderate 2–4 h; High > 4 h.
d) Required expertise: Low (app-guided data capture); Low to Moderate (consumer camera with basic SfM processing); Moderate (UAV operation with photogrammetric processing and GCP handling); High (survey-grade TLS deployment, scan planning, and point cloud registration).

4 RESULTS AND DISCUSSION

4.1 Quantitative Overlap Metrics and LoD95

Using the CloudCompare M3C2 algorithm, the UAV-SfM reconstruction of the Pećine breakwater was compared with the handheld SfM reconstruction. The analysis was conducted on a high-confidence subset defined by a minimum point support in both clouds of $N_{pts1,2} \geq 20$, local surface roughness $STD_{1,2} \leq 0.05$m, and a reporting filter of $|d| \leq 0.01$m. The resulting overlap quality is high.

The mean signed distance between the two datasets is effectively zero ($d = -0.00096$ m), with millimetric dispersion ($\sigma_{rel} = 0.004324$ m). The resulting hybrid uncertainty yields a level of detection at 95% confidence of $LoD_{95} = 0.02135$m. Spatial coverage is robust and

representative of the entire structure: 67.64% of all core points fall within ±1 cm ($N_{\pm 1} = 2{,}269{,}113$) and 73.59% within ±3 cm ($N_{\pm 3} = 2{,}468{,}686$) out of a total of $N_{\text{all}} = 3{,}354{,}741$, indicating close agreement over most of the breakwater.

The spatial distribution of M3C2 distances for the high-confidence subset is shown in Figure 10, with the handheld SfM point cloud used as the core dataset. Colours are clipped to ±0.01 m, and distances follow Eq. (1), such that positive values indicate that the UAV-SfM surface lies above the handheld SfM core. Residuals outside this interval are predominantly concentrated at block edges and within occluded recesses, reflecting local geometric complexity rather than systematic bias between the datasets.

From a practical engineering perspective, differences in crest elevation, berm width, or slope exceeding approximately 2–3 cm can be interpreted as real geometric variations. Smaller differences fall below the detection capability of the combined workflow unless further improvements in alignment precision are achieved.

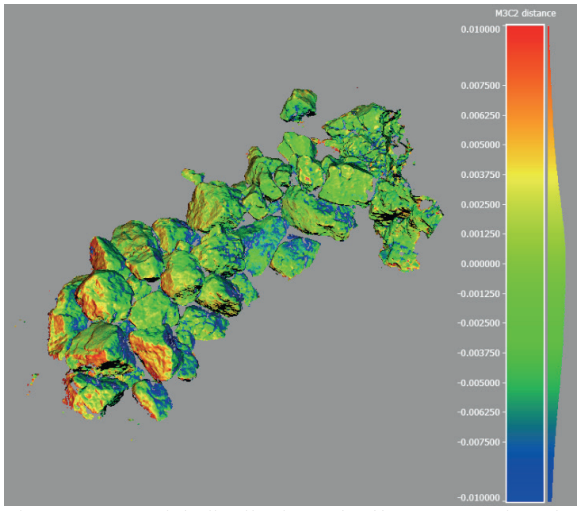

Figure 10. Spatial distribution of offsets comparing the UAV-SfM reconstruction to the handheld SfM core. Colours encode distances according to Eq. (1) and are clipped to ±0.01 m; positive values indicate the UAV-SfM surface above the core.

4.2 Cross-sectional analysis of the Pećine breakwater point clouds

The transverse cross-sections of the Pećine breakwater indicate that UAV-SfM, handheld SfM, and sLiDAR capture the overall armour-block geometry with a high degree of consistency. Figure 11 overlays Profiles 1–4 to illustrate the level of agreement between methods.

In Profile 1, the UAV-SfM trace exhibits a faint secondary line beneath the true contour, caused by oblique viewing angles that partially captured undercut block faces. A single spurious point is also present in the handheld SfM reconstruction at the same location, attributable to limited camera access between blocks. Smartphone LiDAR, although unable to resolve a small central void, provides the most complete representation in this profile due to its ease of close-range manoeuvring.

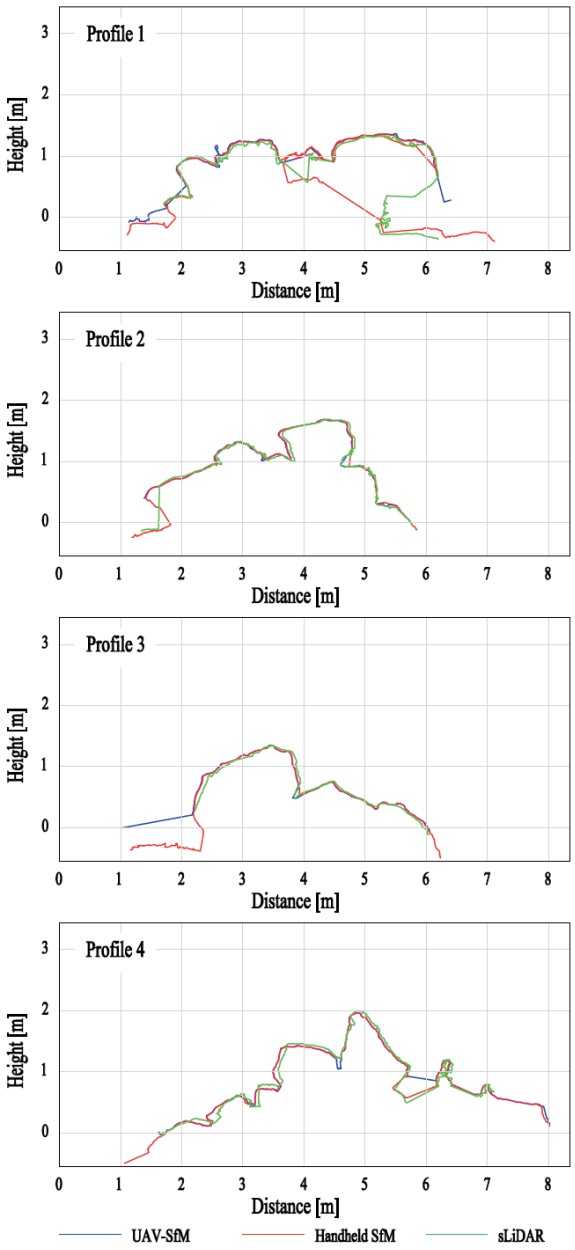

Figure 11. Overlaid transverse cross-section profiles (Profiles 1–4) of the Pećine breakwater obtained using UAV-SfM, handheld SfM, and sLiDAR, displayed in AutoCAD.

Profile 2 shows near-perfect overlap among all three methods in an unobstructed section of the structure. Profile 3 similarly demonstrates strong agreement; however, the sLiDAR profile truncates on the seaward side where water-surface reflections prevented reliable returns, whereas both SfM-based profiles extend slightly further before encountering occlusions. In Profile 4, a local deviation near the 6 m mark is evident in the handheld SfM profile, where a narrow inter-block gap was not captured and the reconstruction consequently smoothed the surface.

Overall, UAV-SfM and handheld SfM perform comparably to sLiDAR in well-lit and accessible areas, whereas sLiDAR is superior in zones characterized by undercuts, occlusions, or restricted access.

Profile-wise discrepancies relative to the sLiDAR reference were quantified using the M3C2 metric with a projection scale of 0.02 m. Across Profiles 1–4, the signed mean deviations are small (approximately 5–6 mm), while the standard deviation typically ranges between 4 and 6.5 cm, resulting in method-level root-mean-square (RMS) values of about 4.8 cm for both UAV-SfM and handheld SfM (Table 4). The largest dispersion occurs in Profile 1 for UAV-SfM (RMS ≈ 6.5 cm), consistent with the presence of local occlusions and reduced surface texture. In regions where all methods overlap, the majority of deviations fall within ±5 cm.

Table 4. M3C2 deviations (m) between SfM-derived point clouds and the sLiDAR reference for four transverse cross-sections (P1–P4) at the Pećine breakwater.

Profile	Method vs. LiDAR	Points	Mean (m)	Std. dev. (m)	RMS (m)
P1	UAV SfM – LiDAR	14,297	0.00109	0.06511	0.06512
	Handheld SfM – LiDAR	30,454	-0.0044	0.05063	0.05082
P2	UAV SfM – LiDAR	11,832	0.00953	0.04103	0.04212
	Handheld SfM – LiDAR	28,840	0.01298	0.04622	0.04801
P3	UAV SfM – LiDAR	10,950	0.00349	0.04055	0.0407
	Handheld SfM – LiDAR	21,428	0.00687	0.04716	0.04766
P4	UAV SfM – LiDAR	18,374	0.00778	0.04379	0.04448
	Handheld SfM – LiDAR	42,363	0.00945	0.04424	0.04524

4.3 Comparison of the as-built Mitan breakwater with design specifications

To evaluate conformity with the design, numerical cross-sections derived from handheld SfM and sLiDAR point clouds were compared with the project documentation (MareCon, 2023). Figure 12 presents all extracted sections in a single panel, comprising transverse Profiles 1–8 and longitudinal Profiles 9–12, with handheld SfM shown in blue and sLiDAR in red.

Within the transverse set, Profiles 2, 3, and 4 demonstrate that the sLiDAR-derived contours resolve interstitial voids between armour blocks that are only partially captured by handheld SfM, owing to the latter's reliance on sufficient image overlap. Profile 4 further illustrates a case where the sLiDAR trace terminates due to an obstructed incidence angle, whereas the handheld SfM contour extends farther owing to a greater stand-off distance. Profiles 5 and 8 exhibit incomplete sLiDAR traces associated with the segmented acquisition of the breakwater, which complicated merging and georeferencing across individual segments. Minor deviations in the handheld SfM profiles are observed in shadowed or steeply inclined areas where photographic coverage was limited.

In the longitudinal set, Profiles 9–12 closely follow the intended design elevations. Profile 12 accurately reproduces the 3 m elevation, while Profiles 11 (3 m), 10 (2 m), and 9 (1 m) similarly conform to their respective design targets. In Profile 10, the sLiDAR contour extends further down the seaward slope than the handheld SfM profile, reflecting the ability of close-range sLiDAR acquisition to capture undercut and overhanging zones. Overall, both methods produce closely overlapping contours, with deviations generally within a few centimetres across the analysed sections, indicating no systematic departures from the design geometry.

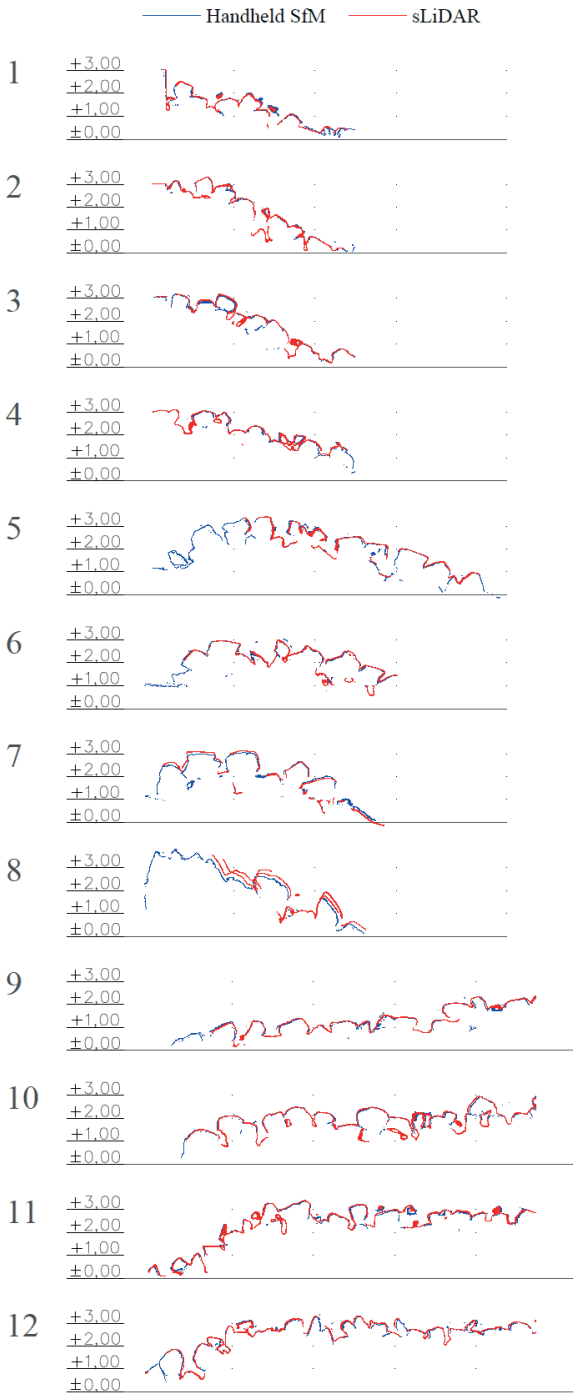

Figure 12. Cross-sections of the Marina Mitan breakwater derived from handheld SfM (blue) and sLiDAR (red) point clouds in AutoCAD. Transverse Profiles 1–8 and longitudinal Profiles 9–12 are shown, with axes in metres.

Figure 13 shows the design cross-section with the locations of longitudinal Profiles 9–12 indicated for reference. In addition, transverse Profile 2 is directly overlaid along the seaward vertical wall using the design documentation (MareCon, 2023). This profile clearly illustrates the geometry and elevation of the stone-filled armour layer, where the sLiDAR-derived contour (red) closely tracks the design line. Cross-sectional measurements yield a berm width of 2.60 m and a revetment slope of 1:1.5, confirming that the as-built structure complies with the original specifications.

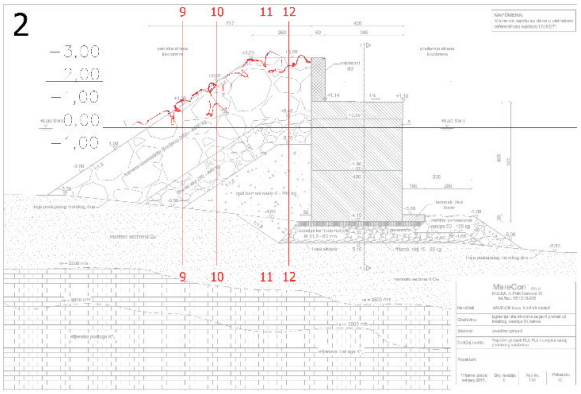

Figure 13. Point cloud cross-sections for longitudinal Profiles 9–12 and transverse Profile 2 on the Mitan breakwater, overlaid on the design section. sLiDAR (red) contours closely match the design geometry (MareCon, 2023); Profile 2 indicates a 2.60 m berm width and a 1:1.5 revetment slope.

CONCLUSIONS

This study demonstrates that a multisensor, RTK-referenced point-cloud workflow can capture and analyse the geometry of rubble-mound breakwaters with decision-grade accuracy at modest cost and operational effort. UAV-based SfM, handheld SfM, sLiDAR, and—where feasible—TLS were integrated within a single control network, then aligned, quality-checked, and analysed using consistent parameters. Uncertainty in hybrid overlaps was treated explicitly by combining M3C2 normal-direction distances with the alignment root-mean-square (RMS), yielding a hybrid uncertainty and a 95% confidence level of detection that frames all comparisons.

At the Pećine breakwater, the overlap between UAV SfM and handheld SfM is strong: the mean signed normal distance is effectively zero, with millimetric dispersion. Coverage within ±1 cm and ±3 cm of the normal direction reaches 67.64% and 73.59% of all core points

(approximately 3.35 million), respectively. The derived detection limit at 95% confidence is 0.021 m, indicating that differences on the order of two to three centimetres can be interpreted as real changes across most of the structure. Transverse cross-sections extracted at 2.5 m spacing confirm close agreement among methods; profile-wise RMS values typically range from four to five centimetres, with larger residuals confined to block edges and occluded recesses where true overlap is limited.

At the Mitan breakwater, handheld SfM and sLiDAR successfully reproduce the design elevations and dimensions. The measured berm width is 2.60 m, and the revetment slope conforms to the specified 1:1.5. The datasets are both substantial and complementary: the sLiDAR point cloud comprises approximately 10.0 million points, while the handheld SfM point cloud contains about 2.25 million points. Together, they resolve both exterior surfaces and interior voids accessible from the armour layer. Overall, the two methods produce closely overlapping contours, with no systematic departures from the design geometry.

The comparative assessment clarifies key operational trade-offs. UAV SfM provides the fastest coverage and highest point density for a given field time; handheld SfM adds colour and geometric detail in accessible areas; sLiDAR effectively resolves undercuts and interior voids at close range; and TLS offers a highly precise baseline where safe access and station placement are possible, albeit with greater deployment demands. The accompanying table summarising time, cost, effort, and expertise requirements serves as a practical decision aid for selecting a fit-for-purpose combination of methods in coastal surveys. In practice, UAV SfM is recommended for rapid, large-area surveys when time and personnel are constrained, with handheld SfM and sLiDAR added where complex geometry, shadowing, or occlusions are present.

Periodic re-survey following a consistent schedule, using the same control network and processing parameters, supports early detection of settlement, armour displacement, and toe migration. The workflow scales effectively to harbour-scale assets through a stable RTK control framework and a tiled acquisition and processing strategy, preserving uniform accuracy as spatial extent increases and enabling targeted re-survey of affected sections after storms or construction activities. Limitations arise where surfaces are not jointly observed, notably at block edges, occluded recesses, and near the waterline. These effects are mitigated by reporting results for a high-confidence subset, documenting M3C2 and cross-section extraction parameters, and prioritising robust registration. Future work should focus on improving alignment in areas with complex access, adopting adaptive neighbourhood selection for M3C2, and routinely using empirical cumulative distributions of normal distances to summarise spatial coverage and acceptance thresholds. Collectively, these steps further consolidate multisensor point-cloud workflows as a reliable basis for construction verification, condition monitoring, and targeted maintenance of coastal infrastructure.

ACKNOWLEDGEMENTS

This work was supported by the University of Rijeka through the GraDiS project “Unaprjeđenje modela stjecanja stručnih kompetencija učenjem uz rad kroz izradu diplomskog rada” (Project code A3-21-6; UNIRI CLASS A3) and by the Croatian Science Foundation (Project IP-2022-10-7598). The GraDiS project was led by Associate Professor Dr. Sc. Silvija Mrakovčić and funded under the University of Rijeka’s UNIRI CLASS A3 programme. The funding bodies provided financial support for data acquisition, analysis, and manuscript preparation but were not involved in the study design, data interpretation, writing of the manuscript, or the decision to submit it for publication.

REFERENCES

Agisoft (2021) Agisoft PhotoScan User Manual: Professional Edition, Version 1.7. Agisoft LLC.

Błaszczak-Bąk, W.; Janicka, J.; Dumalski, A.; Masiero, A. (2023). Integration of Terrestrial Laser Scanning and Smartphone LiDAR: The Case Study of Lidzbark Castle. *International Archives of the Photogrammetry, Remote Sensing and Spatial Information Sciences*, XLVIII-1/W1, 51–56.

Campbell, J. B.; Wynne, R. H. (2011). Introduction to Remote Sensing. Guilford Press.

CloudCompare Wiki (2023). *CloudCompare Wiki* [Online]. Retrieved June 19, 2023, from https://www.cloudcompare.org/doc/wiki/index.php/Main_Page

FARO Technologies Inc. (2015). FARO Laser Scanner Focus3D X 130 Manual, February 2015.

James, M.; Ilić, S.; Ružić, I. (2013). Measuring 3D Coastal Change with a Digital Camera. In Proceedings of Coastal Dynamics 2013, Arcachon, France; pp. 893–904.

James, M. R.; Robson, S.; Smith, M. W. (2017). 3-D uncertainty-based topographic change detection with structure from motion photogrammetry: Precision maps for ground control and directly georeferenced

surveys. Earth Surface Processes and Landforms, 42(12), 1769–1788.
Lague, D.; Brodu, N.; Leroux, J. (2013). Accurate 3D comparison of complex topography with terrestrial laser scanner: Application to the Rangitikei canyon (N-Z). *ISPRS Journal of Photogrammetry and Remote Sensing*, 82, 10–26. (doi:10.1016/j.isprsjprs.2013.04.009)
MareCon d.o.o. (2023). *Tehnička dokumentacija lukobrana marine Mitan*. MareCon d.o.o., Rijeka, Croatia
Over, J. R.; Ritchie, A. C.; Kranenburg, C. J.; Brown, J. A.; Buscombe, D. D.; Noble, T.; Sherwood, C. R.; Warrick, J. A.; Wernette, P. A. (2021). Processing Coastal Imagery with Agisoft Metashape Professional Edition, Version 1.6 - Structure from Motion Workflow Documentation. U.S. Geological Survey Open-File Report 2021-1039, 46 p. https://doi.org/10.3133/ofr20211039.
Petković, I. (2023). Primjena 3D oblaka točaka za projektiranje u priobalnom području [Master's thesis, University of Rijeka, Faculty of Civil Engineering]. University of Rijeka Repository.
Puente, I.; Lindenbergh, R.; González-Jorge, H.; Arias, P. (2014). Terrestrial laser scanning for geometry extraction and change monitoring of rubble mound breakwaters. *ISPRS Annals of the Photogrammetry, Remote Sensing and Spatial Information Sciences* II-5: 289–296.
Ružić, I.; Dugonjić, S.; Benac, Č.; Krvavica, N. (2019). Assessment of the Coastal Vulnerability Index in an Area of Complex Geological Conditions on the Krk Island, Northeast Adriatic Sea. Geosciences, 219(9).
Ružić, I.; Marović, I.; Benac, Č.; Ilić, S. (2014). Coastal cliff geometry derived from structure-from-motion photogrammetry at Stara Baška, Krk Island, Croatia. Geo-Marine Letters, 34(6), 555–565.
Syafie, F. S.; Khalid, N.; Tahar, K. N.; Naharudin, N.; Kamaruddin, A. H. (2024). Assessment the Accuracy of Crack Detection Derived from Smartphone LiDAR and TLS Dataset. *Proceedings of the 2024 IEEE International Conference on Automatic Control and Intelligent Systems*, 1–5.
Šuput, N. (2023). Primjena daljinskih istraživanja kod projektiranja i praćenja obalnih građevina (Master's thesis, University of Rijeka, Faculty of Civil Engineering). University of Rijeka Repository.
Tadić, A.: Ružić, I.; Krvavica, N.; Ilić, S. (2022). Post-Nourishment Changes of an Artificial Gravel Pocket Beach Using UAV Imagery. Journal of Marine Science and Engineering, 10(3).
Wang, Y. (Ed.) (2009). Remote Sensing of Coastal Environments. CRC Press.
Winiwarter, L.; Anders, K.; Höfle, B. (2021). M3C2-EP: Pushing the limits of 3D topographic point cloud change detection by error propagation. ISPRS Journal of Photogrammetry and Remote Sensing, 178, 240–258.

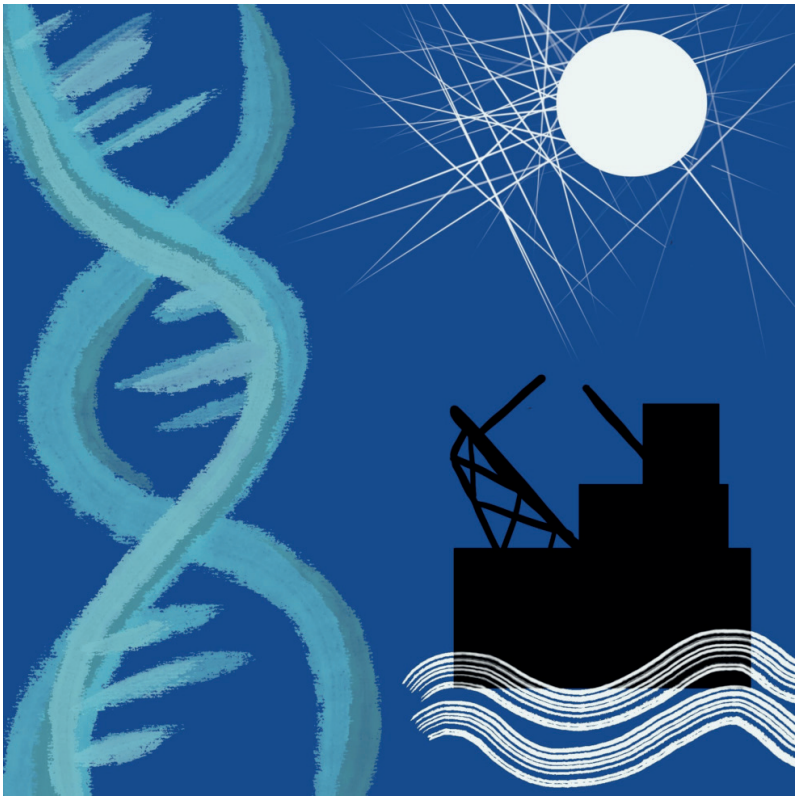

Concept:
Stefano Pagliai

Cover credits:
Cover image by ©**Marialuisa Sabato**

Web-site
https://www.ecampusuniversitypress.it/riviste/coastal-and-offshore-science-and-engineering/

Contact
editore@uniecampus.it

Publisher
Studium Srl
via Matera, 18 – 00182 – Roma
via Isimbardi, 10 – 22060 – Novedrate (CO)
www.studiumeditore.it

Registration with the Court of Como n. 2, March 7, 2022.

Coastal and Offshore Science and Engineering

an International open-access Journal

6/2024
ISSN 2785-7972

STUDIUM EDITORE

eCAMPUS UNIVERSITÀ

eCAMPUS UNIVERSITY PRESS